Twenty-first century wind and solar energy potential in northern Canada

by

Laura Van Vliet
BSc Env Sci, University of Guelph, 2014

A thesis submitted in partial fulfillment of the requirements for the degree of

MASTER OF SCIENCE

in the School of Earth and Ocean Sciences

We acknowledge with respect the Lekwungen peoples on whose traditional territory the university stands and the Songhees, Esquimalt and W̱SÁNEĆ peoples whose historical relationships with the land continue to this day.

Twenty-first century wind and solar energy potential in northern Canada

by

Laura Van Vliet
BSc Env Sci, University of Guelph, 2014

Supervisory Committee

Dr. Adam Monahan, Co-Supervisor
(School of Earth and Ocean Sciences)

Dr. Charles Curry, Co-Supervisor
(School of Earth and Ocean Sciences)

Dr. David Atkinson, Outside Member
(Department of Geography)

Abstract

Northern regions of Canada are of special interest for renewable energy investment due to the high cost of traditional energy generation in remote communities (Das & Canizares 2016b). However, climate variability and change have a substantial impact on renewable energy yield and system vulnerability (e.g., Ravestein *et al.* 2018; van der Wiel *et al.* 2019), and the North will experience more dramatic impacts due to climate change compared with other parts of Canada (Serreze 2015). Using the Canadian Regional Climate Model Version 4 (CanRCM4) large ensemble driven by Representative Concentration Pathway 8.5, current and future wind and solar energy potential, variability and covariability in northern Canada were assessed. Eight focal communities were additionally selected for in-depth analysis based on the work of Das & Canizares (2016b). Robust increases in annual average wind power potential (*WPP*) are projected across the northernmost part of the study area by 2070-2099 (up to 30%), with changes most pronounced in cold seasons. Decreases in *WPP* are projected for southern areas. Solar power potential (*SPP*) is projected to decrease across the study area, with robust changes emerging by as early as 2010-2039. For the focal communities, *WPP* stability (as measured through inter- and intra-annual variability) is projected to increase, while *SPP* stability is projected to decrease. The changes in *WPP* variability are associated with a dampening of the seasonal cycle of *WPP* in the north. Monthly mean *WPP* and *SPP* are negatively correlated, with approximately oppositely-phased seasonal cycles. Combined wind/solar installations therefore show reduced sub-annual variability, stabilizing power supplies relative to installations of solely wind or solar power.

Drivers of change in *WPP* and *SPP* are complex, but changes in sea ice across the 21st century will play an important role for both *WPP* and SPP. Over the northern ocean

regions, the influence of sea ice loss on roughness length is found to be more important than impacts on surface layer stability. Changes in storm winds also play a role, but impacts due to synoptic storm activity are difficult to distinguish from shifts in the wind speed distribution. Decreases in *SPP* can be attributed to projected reductions in downwelling shortwave radiation, which in turn are closely associated with changes in cloud characteristics (e.g., optical depth), as measured through CanRCM4 column liquid/ice water content. Clear-sky changes in shortwave radiation were not directly assessed, but are potentially impacted by robust increases in column water vapour.

Overall, northern regions of Canada and the focal communities show high potential for renewable energy generation across the 21st century. Projected increases in wind power resources and wind power stability in the focal communities could enhance the cost-savings and emissions reductions predicted based on current climate assessments (e.g., Das & Canizares 2016b). With ever improving technologies and declining costs, the viability of renewable power in the north is likely to become even more certain in years to come.

Table of Contents

List of Tables

List of Figures

Acknowledgements

I would like to thank:

- My wonderful family for their unfailing love and support.
- My supervisors, Adam Monahan and Charles Curry, for their continuous guidance, support, and understanding. This would not have been possible without your help.
- My committee member, David Atkinson (University of Victoria), for his knowledge of Arctic weather and climate systems.
- Carsten Abraham (University of Victoria) for helping me learn the ropes when I first arrived.
- Yanjun Jiao (Environment and Climate Change Canada) for responding so quickly to my endless data requests, and John Scinocca (Environment and Climate Change Canada) for providing technical details on CanRCM4.
- Curran Crawford (University of Victoria) and Marvin Quitoras (University of Victoria) for their insight into the technical aspects of wind power production.

Chapter 1

Introduction

Across the globe, interest in renewable energy is growing in response to environmental and economic pressures, with wind and solar energy receiving particular emphasis. Northern regions of Canada are of special interest for renewable energy investment; remote northern communities are disconnected from larger energy grids, and traditional methods for local power generation (such as diesel generators) are costly (Das & Canizares 2016b). To date, however, renewable power in these regions has remained largely unexploited (Natural Resources Canada 2021). Harsh conditions can make it difficult and costly to install, operate, and maintain equipment. In addition, the natural variability in wind speed and solar irradiance make integrating renewable power reliably both challenging and expensive (Natural Resources Canada 2021).

With recent advancements in solar and wind energy technology, investment in renewables in the Canadian north has seen growing interest. A 2016 study commissioned by the World Wildlife Fund (WWF) found high potential for implementation of renewable wind energy in Nunavut communities (Das & Canizares 2016a,b). The study assessed potential cost-savings, renewable energy penetration, and CO_2 emissions reductions. As typically done when performing renewable energy site assessments, Das & Canizares (2016a) used historical climate means to assess feasibility of implementation. However, as wind and solar energy generation are directly tied to weather conditions, climate variability and change will have a substantial impact on energy yield and system vulnerability (e.g., Ravestein *et al.* 2018; van der Wiel *et al.* 2019). Future climate uncertainty results from both anthropogenic climate change and the natural internal variability of the climate. Canada's far north will experience more dramatic impacts due to climate change compared to other parts of Canada (Serreze 2015). However, relatively little emphasis has been placed on the effects of climate change on wind and solar energy potential in Canada. Understanding the natural climate-driven internal variability of wind and solar power will help assess the stability of renewable resources and the feasibility of current or future installations.

Global and regional climate models can be used to assess variability and change in wind speed and solar irradiance, and their associated impacts on renewable energy resources (e.g., Gernaat *et al.* 2021; Jerez *et al.* 2015b; Wild *et al.* 2015a). Regional climate models (RCMs) have advantages over global models in their ability to resolve finer-scale spatial features and related influences on atmospheric processes (see Flato *et al.* 2014 and references therein). The Canadian Regional Climate Model Version 4 (CanRCM4), developed by the Canadian Centre for Climate Modelling and Analysis, has been used to produce a large ensemble (LE) driven by Representative Concentration Pathway 8.5 forcings (Scinocca *et al.* 2016), an extreme climate change scenario. Unlike many RCMs, CanRCM4 includes transient aerosol forcings (Scinocca *et al.* 2016), a critical component for assessing changes in solar irradiance and related features over time.

The present work assesses current and future wind and solar energy potential in Canada's north using the CanRCM4-LE. Emphasis will be placed on the select communities identified in the WWF report. Mean energy potential and intra- and inter-annual variability from 1970 to 2100 will be evaluated, followed by an analysis of the covariability of wind and solar power. Finally, potential contributors to change in energy potential and variability will be assessed.

Chapter 2 presents a literature review describing historical and projected wind and solar power resources, sources of uncertainty in climate modelling, and CanRCM4. Chapter 3 describes the study area and methods for modelling and analyzing wind and solar energy potential. In Chapter 4, current and future wind and solar energy potential, variability, and covariability are presented and discussed. This is followed by an analysis of potential contributors to change. Conclusions are summarized in Chapter 5.

Chapter 2

Background

2.1 Historical and projected near-surface wind speeds and wind energy potential

See Table A.1 in Appendix A for a summary of previous research on 21st century near-surface wind speeds and wind power potential.

During the period from about 1980 to 2010, decreases or "stilling" of near-surface (10 m) wind speeds (SWS) were reported globally and in Canada from both station-based observations (e.g., McVicar *et al.* 2012; Tuller 2004; Wan *et al.* 2010) and reanalysis datasets (e.g., Deng *et al.* 2021; Hundecha *et al.* 2008). However, more recent assessments of global station observations have found a reversal of this trend since about 2010 (e.g., Deng *et al.* 2021; Zeng *et al.* 2019). A notable exception to the period of terrestrial stilling may be high-latitude regions (e.g., Leung *et al.* 2020; Lynch *et al.* 2004; McVicar *et al.* 2012; Pinard 2007), although trends are variable based on the data source and study.

Observation-based studies in northern Canada largely reported increases in SWS in recent decades, while other parts of the country largely followed global stilling trends. An analysis of the wind climate of three sites in the Whitehorse area revealed increases of 1 m/s from 1956 to 2005 (Pinard 2007), while a case study in Barrow, Alaska from 1920 to the early 2000s showed significant[1] increases in winter and spring mean wind speeds (Lynch *et al.* 2004). Leung *et al.* (2020) compared wind speeds for the periods 1971-1990 and 1991-2010 for six communities around Hudson Bay, and found decreasing trends in annual wind speeds for the three inland communities (including Baker Lake), while significant increases in daily average SWS were observed for the three coastal communities. Using station data, Vautard *et al.* (2010) concluded that SWS over continental areas in the northern mid-latitudes de-

[1]Use of the term 'significant' when referring to the work of others denotes significance by their definition, which may be formal hypothesis testing or use of a signal-to-noise ratio.

creased by 5-15% from 1979-2009. However, over the Canadian prairies and some northern regions SWS was shown to be increasing (Vautard *et al.* 2010). Assessment of homogenized Canadian station data from 1953 to 2006 identified significant increases in wind speeds in the central Canadian Arctic in all seasons, with significant decreases throughout most of southern Canada (except the Maritimes) and western Canada (Wan *et al.* 2010). These results agree with Tuller (2004), who found decreases in annual mean SWS at three of four West Coast weather stations in the latter half of the 20th century, with the exception hypothesized to be due to changes in surface roughness. In a global review of continental SWS changes from studies using observational datasets, McVicar *et al.* (2012) concluded decreasing trends were globally predominant until about 2010, including most of Canada, but excluding high-latitudes in both hemispheres and notably Nunavut in Canada (McVicar *et al.* 2012).

While there remains much uncertainty in the ability of reanalyses to reproduce SWS (e.g., Pryor *et al.* 2009; Torralba *et al.* 2017; Vautard *et al.* 2010), Deng *et al.* (2021) concluded they generally reproduce global terrestrial stilling and the reversal around 2010, although of a much smaller magnitude than observations. Trends in SWS from 1980-2010 in Canada's far north varied in sign among reanalyses, but were generally decreasing, except in the Arctic Archipelago at >70°N (Deng *et al.* 2021). Using the North American Regional Reanalysis (NARR) in the greater Gulf of St Lawrence/ eastern Canada region, Hundecha *et al.* (2008) detected significant increases in annual maximum wind speeds in the southern Maritimes in the period of 1979-2004, with significant decreases in Northern Quebec/Labrador interior. However, overall little widespread significant change was detected (only 7% of grid cells).

Reported trends in SWS are of concern for renewable resources, as wind power density (WPD) is largely controlled by surface wind speeds. Globally averaged, Zeng *et al.* (2019) estimated the change in wind speed from 2010 to 2017 would correspond to a 17% increase in wind power potential, while if the stilling trend of 1980 to 2010 continued at pace until the end of the century, it would result in an about 50% decrease in wind power potential. Projection of wind energy resources from Earth System Models (ESMs) under climate change remains unclear, as ESM skill in reproducing SWS trends remains poor and inter-model uncertainties high (Chen 2020; Cheng *et al.* 2014; Tian *et al.* 2019). However, projections of SWS for northern Canada are largely increasing, while southern regions of Canada are generally projected to experience decreases or little change.

While most studies agree on projected increases in SWS and WPD for northern Canada and Arctic regions, the spatial pattern and magnitude of this projected change is inconsistent among models. Using a Regional Climate Model (RCM) driven by CanESM2 and MPI-ESM, Jeong & Sushama (2019) project increases in wind speeds in northern Canada by 2071-2100 for both driving ESMs under RCP4.5 and 8.5, particularly for regions between

the Beaufort Sea and northern Quebec, including Hudson Bay. Decreases in summer (JJA) mean wind speeds are projected for most of North America, excluding northern Canada (Jeong & Sushama 2019). This pattern was also largely found by Jung & Schindler (2019) in their assessment of 12 CMIP5 ESMs under RCP8.5, projecting increases in mean wind speed for Hudson Bay and the northern part of the Canadian Arctic Archipelago, with some decreases in Eastern Canada, Baffin Island and southern Alberta and British Columbia by the end of the century. Using the CESM-LE, Mioduszewski *et al.* (2018) also projected significant decreases over most land areas of Canada, with increases projected for northern marine and coastal areas, especially those adjacent to Hudson Bay and parts of Nunavut. These spatial patterns of change are somewhat different than those found by McInnes *et al.* (2011) using CMIP3 models, who projected increases in mean and extreme (99th percentile) annual and DJF wind speeds in a northwest-to-southeast band across central and northern Canada, excluding the high Arctic region projected to see increases (Jeong & Sushama 2019; Mioduszewski *et al.* 2018). Non-significant changes were projected elsewhere in the study area. In a western Canada assessment using the Canadian Regional Climate Model (CRCM) driven by two ESMs, Daines *et al.* (2016) also largely projected modest decreases or no change in SWS and WPD by 2031-2060 compared to 1971-2000 for the ECHAM5-driven model, but projected modest increases with the CGCM-driven model. Redilla *et al.* (2019) used bias-adjusted RCM output driven by two climate models to assess changes in Alaskan wind climatology over the 21st century in a station-based analysis. They also found more widespread, significant wind speed changes for one driving ESM than the other, but both showed similar trends and seasonality in projected changes: increases in cold season wind speeds, and decreases in warm season wind speeds, with increases more common in northwestern and coastal locations, and decreases more common in southern and inland locations (Redilla *et al.* 2019). Yao *et al.* (2012) assessed climate change impacts on wind and related power potential in Ontario using the PRECIS regional climate model. Under the A2 scenario, they projected mean wind speed decreases in southern Ontario of up to 5% by 2071-2100 compared to 1961-1990, and increases of $> 5\%$ for coastal areas off James and Hudson Bay.

Inter-model uncertainty in wind power projections are also high, with projections of change varying considerably. Using a 12-model ensemble from NA-CORDEX, Chen (2020) assessed projected change in SWS and wind energy for North America, but excluded much of northern Canada. Historical SWS and projected changes varied widely between RCMs, in magnitude, sign and spatial pattern, but the multi-model ensemble (MME) mean was reasonably similar to the MERRA-2 reanalysis (see Figures 2.1 and 2.2 for a comparison of historical SWS and projected change by RCM). Under RCP8.5, the MME mean predicts SWS change between -10% and 10% from 1971-2000 to 2071-2100, and wind power density changes of between

-20% and 20%, with decreases over the East Coast, western Canada and the USA, and increases over northern Ontario, Quebec, and Labrador (Chen 2020). The MME indicates that these northern increases are driven by DJF, MAM, and SON increases and offset by JJA decreases, although only DJF and JJA see high agreement between models in this region (Chen 2020). Karnauskas *et al.* (2018) investigated global wind power resources using a 10-model ensemble from CMIP5. Under RCP8.5, annual mean wind power by the end of the century is projected to decrease for the central USA and Eastern Canada. Most of mainland Canada, however, is projected to experience non-robust changes to annual mean power; increases are projected only for parts of the Canadian Arctic Archipelago, with the exception of Baffin Island (Karnauskas *et al.* 2018). Similarly, Gernaat *et al.* (2021) assessed changes in renewable energy technical potential from 1970-2000 to 2070-2100 under RCP6.0 using 4 ESMs from ISIMIP2b[2], finding non-significant decreases in SWS, from 0-5% for much of Canada, with increases only in the northern parts of the Canadian Arctic Archipelago (again excluding Baffin Island) and the Arctic Ocean. This change corresponds to non-significant projected decreases of about 0-10% in wind power potential, with greatest decreases projected for Nunavut, Northern Quebec, and Labrador (Gernaat *et al.* 2021). Averaged across the country, Gernaat *et al.* (2021) found Canadian wind energy potential is projected to decrease significantly. Using 7 models from CMIP6, Qian & Zhang (2021) assessed wind power and climate change in Canada's Northwest Passage, which encompasses part of the Canadian Arctic Archipelago. They project wind energy density will increase in the region North of 72°N, but largely decrease in the region south of the Northwest Passage, with impacts as great as 30% under RCP8.5 by the end of the century relative to 1980-2014. These northern increases are largely due to autumn and winter increases, while spring and summer declines drive projected decreases south of the Northwest Passage (Qian & Zhang 2021).

The drivers of the observed and projected global wind speed trends, including the recent stilling and reversal, remain uncertain. Potential explanations include changes in surface roughness (Vautard *et al.* 2010), changes in boundary layer stability due to increased atmospheric aerosols (Bichet *et al.* 2012), changes in large scale circulation patterns (Torralba *et al.* 2017; Vautard *et al.* 2010), shifting storm tracks (Yan *et al.* 2006), and decadal ocean–atmosphere oscillations (Zeng *et al.* 2019). Whatever the cause, the impact of climate variability and change on wind power is an area of ongoing interest, which has been assessed extensively for Europe (e.g., Hueging *et al.* 2013; Pryor *et al.* 2005; Ravestein *et al.* 2018; Tobin *et al.* 2015), the USA (e.g., Johnson & Erhardt 2016; Pryor & Barthelmie 2011, 2013), and elsewhere (see Solaun & Cerdá (2019) and references therein).

[2]Technical potential accounts for land-use and system performance constraints. ISIMIP2b includes land-use change related to agricultural management (Frieler *et al.* 2017).

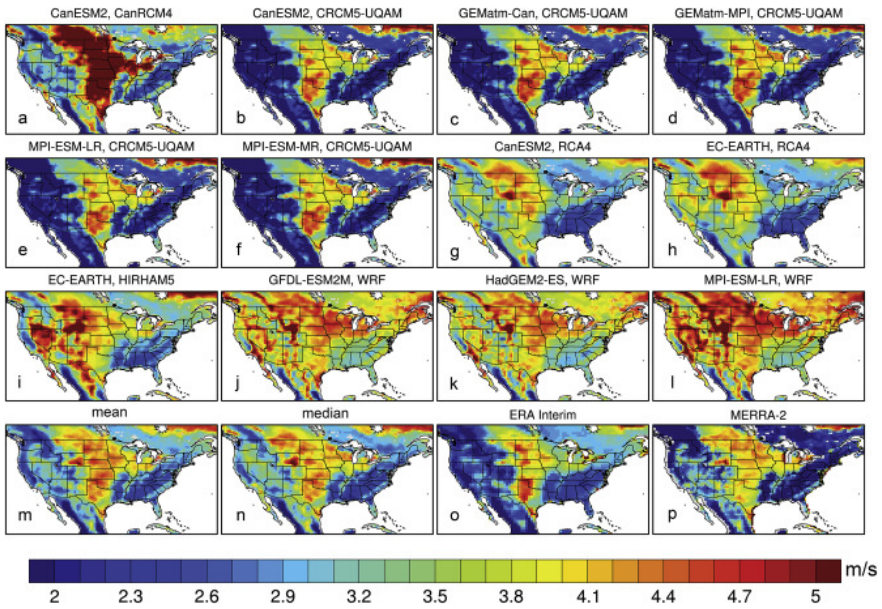

Figure 2.1: Annual mean 1980–2005 SWS (m/s) from 12 NA-CORDEX models (a-l), their MME mean (m) and median (n), and two reanalysis datasets (o-p). Note the maps exclude all but the southernmost portions of the study area for the present work; the figure is intended only to illustrate the influence of model on wind climatology. Figure taken from Chen (2020).

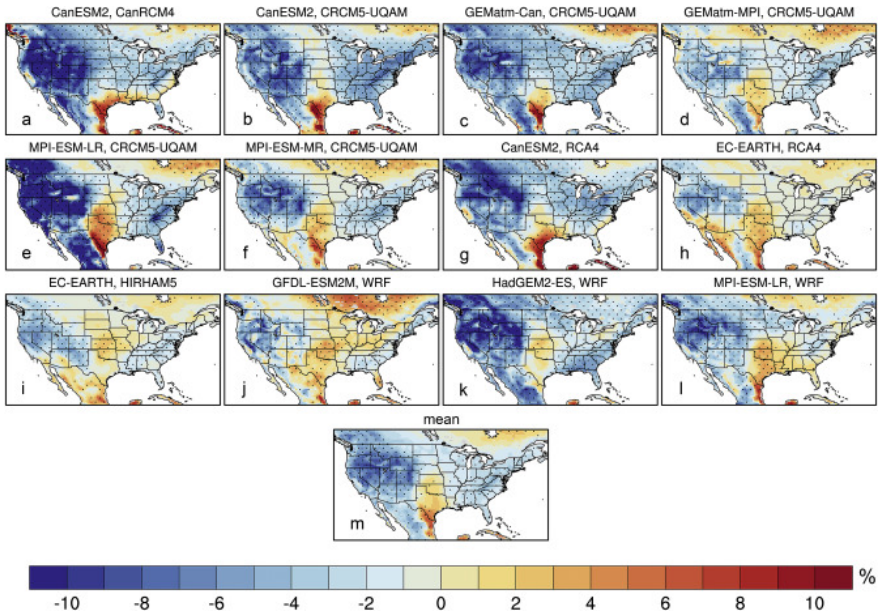

Figure 2.2: Percent change in annual SWS from 1971–2000 to 2071–2100 (RCP8.5 - historical) for 12 NA-CORDEX models (a-l) and their MME mean (m). For individual models, stippling indicates statistically significant changes ($p<0.05$); for the MME mean, stippling indicates that at least 75% of models agree on the sign of a change greater than 0.1 m/s. Note the maps exclude all but the southernmost portions of the study area for the present work; the figure is intended only to illustrate the influence of model on change in wind climatology by the end of the 21st century. Figure taken from Chen (2020).

2.2 Historical and projected solar irradiance and solar energy potential

See Table A.2 in Appendix A for a summary of previous research on 21st century surface solar irradiance and solar power potential.

Similar to SWS and wind power, solar irradiance and related solar photovoltaic (PV) power experience decadal variations. Across much of the globe, historical records indicate a "dimming" period of decreasing downwelling shortwave radiation (DSR) from the 1950s until the late 1980s, followed by a "brightening" period lasting until about 2000 (e.g., Dutton *et al.* 2006; Stanhill 1995; Stanhill & Cohen 2001; Wild 2009; Wild *et al.* 2005). Observed changes affect both all-sky and clear-sky (cloudless) radiation (Wild 2009). In the following discussion, DSR refers to all-sky downwelling shortwave radiation unless otherwise specified. In their comprehensive review, Stanhill & Cohen (2001) concluded that worldwide DSR decreased by 2.7% per decade between the 1950s and 1990s. A study using seven sites in the Canadian prairies revealed a significant average decrease of 1.7% per decade from 1958 to 2005, with dimming trends found in all seasons (Cutforth & Judiesch 2007). This trend was also found in Arctic locations, where significant decreases averaging 3.6 W/m^2 per decade were found from 1950 to 1993 (Stanhill 1995). In the late 1980s, dimming trends ceased. Wild *et al.* (2008) estimated a worldwide brightening trend over land of 2.0 W/m^2 per decade from 1986 to 2000. Since 2000, however, trends are less clear, with some regions experiencing continued brightening while others see reversed trends (e.g., Augustine & Hodges 2021; Wild 2016). Augustine & Hodges (2021), for example, assessed SURFRAD Network data from 1996 to 2019 for the USA, and found a brightening trend from 1996 to 2012, and a dimming trend thereafter until 2019.

Historical changes in DSR have largely been attributed to atmospheric aerosols and cloud cover (see Wild (2009) and references therein). Observed decreases under both all-sky and clear-sky conditions indicate that aerosols, including from anthropogenic emissions, have impacted worldwide solar radiation (e.g., Wild *et al.* 2005). Indeed, the global dimming and partial recovery since the 1980s tracks clean-air policy and regulation in many industrialized nations (Wild *et al.* 2015a). Using 9 ESMs from IPCC AR4, Romanou *et al.* (2007) found a global dimming of about 1-4 W/m^2 for all models over the 20th century, which generally agreed with observed changes, and attribute much of the dimming trend to direct and indirect aerosol effects. On decadal timescales, however, much of the DSR variability was attributed to cloud cover changes linked to atmosphere-ocean oscillations (Romanou *et al.* 2007). The impact of radiatively active gases (H_2O, N_2O, CH_4, etc.) on historical trends in DSR is less important, estimated to be about an order of magnitude less than the observed change (Kvalevåg & Myhre 2007; Wild 2009). The potential contribution of external solar forcing

– the change in incoming extra-terrestrial radiation due to solar cycles or Earth's orbital parameters – is also at least 10 times less than the observed trend (Wild 2009).

Studies of worldwide DSR or PV power potential under climate change generally project decreases across the 21st century, including for Canada. Using 18 models under the SRES A2 emissions scenario, Remund & Müller (2010) projected small decreases in DSR over most of the globe by 2080-99 relative to 1961-90, with some regions of brightening (e.g., Mediterranean). Huber *et al.* (2016) used model output from the E39C-A and ECHAM5-HAM models to assess changes in DSR under SRES A1B, calculating surface irradiance from radiative transfer relationships rather than using direct model output. Comparing means for only 5-year periods, 1995-99 to 2035-39, they project decreases in northern Canada averaging almost 5 W/m^2 (about 2%), coinciding with increasing cloud cover over most of the region, as well as increases (decreases) in aerosol optical depth over northern (southern) Canada. Haywood *et al.* (2011) used the HadGEM2-ES model to investigate contributors to global dimming and brightening over the 21st century under RCP8.5. They project large decreases in cloud-free DSR, with a global average decrease of approximately 5.7 W/m^2 from 2000 to 2090. They attribute this largely to increases in atmospheric water vapour, which is partially offset by decreases in aerosols. Projected trends in all-sky DSR over most areas are minimal, as decreases in cloud cover offset the cloud-free DSR dimming (Haywood *et al.* 2011). Wild *et al.* (2015a) also project dimming in most parts of the globe using 39 CMIP5 models under RCP8.5 until 2050. The multi-model median projects significant increases in cloud cover over polar areas and some parts of northern Canada, associated with significant decreasing trends in all-sky radiation. Projected clear-sky radiation changes are much smaller, close to zero or slightly negative across the globe (Wild *et al.* 2015a).

Consistent with future projections of DSR, studies focusing on PV potential also project decreases across the 21st century. Wild *et al.* (2015a) found significant negative trends in estimated PV power output in northern Canada, with little or no change in southern Canada. Similarly, Zou *et al.* (2019) projected potential PV power on a worldwide scale would decrease by 0.67 kWh/m^2 per year during 2006 to 2100 using 36 CMIP5 models. Stronger decreasing trends were found in high latitudes, including most of northern Canada, coinciding with increases in cloud cover in these regions (Zou *et al.* 2019). Using HadGEM1 and HadCM3 from CMIP3 under SRES A1B, Crook *et al.* (2011) projected decreases of about 10% in PV output in high latitude regions, including northern Canada, from 2010 to 2080. Feron *et al.* (2021) also assessed global PV power potential under climate change using 7 CMIP5 models. The MME projects mean decreases of about 5% in PV potential in northern Canada by 2036-2065 under RCP4.5 (compared to 1961–1990), which largely coincides with an increase in cloud fraction and a decrease in aerosol optical depth in this region (Feron *et al.* 2021). Gernaat *et al.* (2021) assessed climate change impacts on the

technical potential of three different types of solar power: utility-scale and rooftop PV, and concentrated solar power (CSP) under RCP6.0 using four ISIMIP2b models. Significant decreases in solar irradiance are projected for Arctic Canada (mainly the Canadian Arctic Archipelago) by 2071-2100 relative to 1971-2000, with moderate increases in southern regions of Canada (Gernaat *et al.* 2021). This corresponds to significant decreases in PV and CSP technical potential in these northern regions, and non-significant changes elsewhere.

The above studies reveal worldwide dimming is generally projected across the 21st century, associated with decreasing PV power potential. However, a recent study by Chen (2021) revealed differences in the projections of solar irradiance made by many RCMs versus ESMs. Using 14 CMIP5 ESMs, significant **increases** in DSR were projected over the southeast USA/southeastern Canada (Chen 2021). In contrast, for NA-CORDEX RCMs significant **decreases** in DSR were projected over most of the USA. These differences were concluded to be due to differences in cloud behaviour as well as the inclusion of transient aerosol forcings in CMIP5 ESMs, but not the selected RCMs (Chen 2021). In a similar comparative study over Europe, Bartók *et al.* (2017) also found opposing signals in DSR trends in RCMs versus ESMs, and cited differences in cloud behaviour as the cause (with cloud cover decreases [no change] projected for ESMs [RCMs]). As time-invariant aerosols were used by RCMs in Bartók *et al.* (2017), decreases in projected DSR were attributed to increasing atmospheric water vapour. While regional climate models may have an advantage over ESMs in their ability to resolve finer-scale features, different parameterization schemes or treatment of aerosols may lead to new biases (see Bartók *et al.* 2017 and references therein). The following work is novel in its use of a regional climate model (CanRCM4) to investigate projected DSR and PV potential over Canada. Unlike many RCMs, CanRCM4 includes transient aerosol forcings, and is driven on its lateral boundaries by prognostic variables from its parent ESM (CanESM2; Scinocca *et al.* 2016).

2.3 Sources of uncertainty

There are three main sources of uncertainty in climate modelling: model, scenario, and internal climate variability (Collins *et al.* 2013). Model uncertainty refers to the inherent limitations of climate models and their inability to fully reproduce the climate system because of limited computational resources and imperfect process representation (Collins *et al.* 2013; Mankin *et al.* 2020). Scenario uncertainty refers to the unknowns as to future emissions trajectories and other climate forcings. The third source, internal climate variability, refers to variations inherent to the naturally chaotic atmospheric system; the variability that would exist even if all external influences are held constant (Hu *et al.* 2012). Internal variability plays a larger role at smaller time and spatial resolutions (Hawkins & Sutton 2009).

Hawkins & Sutton (2009) found that internal variability and model spread were the greatest contributors to uncertainty in short-term projections, while model and scenario uncertainty dominated for long-term projections. Scenario uncertainty is typically dealt with by considering multiple emissions scenarios (Collins *et al.* 2013). As discussed in Section 2.4, the present study uses only one scenario, RCP8.5, to quantify projected impacts on wind and solar resources in a 'worst-case' scenario. In other words, it can be seen as an upper bound of climate change impacts on renewable energy potential. Chen (2020) assessed wind speed and wind energy change over the contiguous USA using NA-CORDEX and found that near- and long-term changes projected by RCP4.5 were similar to those projected in the near-term for RCP8.5. Overall, greatest change was projected in the RCP8.5 long-term scenario (Chen 2020).

Multimodel ensembles (MME) are often used address model uncertainty (Collins *et al.* 2013; Eyring *et al.* 2016). However, MME can confuse uncertainty due to internal variability with that resulting from model structure. Within a MME, single realizations from different models may show opposite signals in their climate projections due to natural variability alone, and not because of structural differences in the models (Deser *et al.* 2012a). Large ensembles of single climate models have advantages in their ability to (1) identify the full range of potential outcomes consistent with a selected emissions scenario; (2) better quantify the irreducible uncertainty due to internal variability (Mankin *et al.* 2020); and (3) identify robust signals in climate projections (Deser *et al.* 2012b). This study uses the single-model CanRCM4 large ensemble to assess change to wind and solar energy potential. While the use of the CanRCM4 large ensemble will not address potential biases associated with model uncertainty, it will preclude conflating model uncertainty with uncertainty due to internal variability (Mankin *et al.* 2020), and allow us to address our central research questions: robust identification of climate change signals and quantification of internal variability. Large single-model ensembles have been used previously to assess forced and internal variability in wind and/or solar power potential in Europe (e.g., Hueging *et al.* 2013; Ravestein *et al.* 2018).

2.4 Canadian Regional Climate Model Version 4

This study uses model output from the Canadian Centre for Climate Modeling and Analysis' (CCCma, part of Environment and Climate Change Canada [ECCC]) Regional Climate Model Version 4 (CanRCM4) large ensemble. Simulations in this 50-member initial condition large ensemble have the same forcings, varying only in initial conditions of the atmosphere or ocean. CanRCM4 has been used in other studies to assess projected change in climate variables, extremes, and compound events (e.g., precipitation (Diaconescu *et al.* 2016), driving

rain wind pressure (Jeong *et al.* 2020), temperature (Whan *et al.* 2016), freezing precipitation (Jeong *et al.* 2019), and rain-on-snow events (Jeong & Sushama 2018)).

The CanRCM4 simulations use a 0.44° grid (approximately 50 km by 50 km) that encompasses North America and adjacent ocean areas, corresponding to the North American domain defined by the Coordinated Regional Climate Downscaling Experiment (CORDEX) project. CanRCM4 has the same dynamical core as ECCC's Global Environmental Multiscale model (Côté *et al.* 1998), but employs the physical parameterizations of CCCma's fourth-generation Canadian atmospheric global climate model (CanAM4, von Salzen *et al.* 2013), also used by CanESM2. CanRCM4 boundary layer physics are described in Abdella & McFarlane (1997). The Canadian Land Surface Scheme version 2.7 (Verseghy 2000) integrates land surface processes, including energy and moisture fluxes. CanRCM4 is driven by CanESM2 at its boundaries by all prognostic variables (including aerosols) using historical (1950–2005) and Representative Concentration Pathway 8.5 (RCP8.5, 2006–2100) forcing scenarios (Scinocca *et al.* 2016).[3] Indirect and direct aerosol effects are considered, and the aerosol scheme includes a full sulfur cycle, organic and black carbon, mineral dust, and sea salt (Scinocca *et al.* 2016). As surface boundary conditions, CanRCM4 uses sea surface temperature and sea ice information from CanESM2 (Scinocca *et al.* 2016). Additional details on CanRCM4 can be found in Scinocca *et al.* (2016). Details of the CanRCM4 variables used in this study and their sampling methods are presented in Table 2.1. Most variables are available on a 1-hr or 3-hr basis, with the exception of wind stress, column water content, and sea ice concentration.

RCP8.5 is a high emissions scenario in which total radiative forcings by 2100 increase by 8.5 W/m^2 relative to 1850 (Collins *et al.* 2013). This is a worst-case "business-as-usual" scenario without policy intervention. Sanford *et al.* (2014) and Schwalm *et al.* (2020) conclude that RCP8.5 is generally consistent with historical emissions and current policy. While others debate this (e.g., Hausfather & Peters 2020), this scenario can be considered an upper limit on the external forcing produced by future GHG and aerosol emissions.

2.5 Biases in CanRCM4

CanRCM4 and CanESM2, its parent ESM, both use the same atmospheric model and share physical parameterizations (Scinocca *et al.* 2016). Where possible, direct assessments of CanRCM4 biases are used in the following discussion. If studies for CanRCM4 are not available, relevant assessments of CanESM2 have been cited.

[3]CanRCM4 forcings: greenhouse gases, ozone (tropospheric and stratospheric), anthropogenic sulfate aerosol (direct and indirect), black carbon, organic carbon, land-use change, and volcanic aerosol. It does not include solar forcings, unlike CanESM2.

Jeong *et al.* (2020) performed an analysis of CanRCM4 biases in mean and maximum wind speeds over Canada against station measurements. CanRCM4 was found to underestimate extreme (annual maximum) wind speeds but overestimate annual mean wind speed (Jeong *et al.* 2020). However, the spatial pattern was well reproduced for both measures. For annual mean wind speed, CanRCM4 performed comparably to the ERA-Interim reanalysis, explaining 52% and 53% and of the spatial variance (R-squared of 0.72 and 0.73), respectively, using similar validation periods (Jeong *et al.* 2020). CanRCM4 was also found to reproduce the seasonal cycle of mean wind speeds (intra-annual variability; Jeong *et al.* 2020). Overall, however, near-surface wind speed representation in climate models is biased (Tian *et al.* 2019); both climate models and reanalyses exhibit considerable wind speed biases (e.g., Krishnan & Bhaskaran 2020; Miao *et al.* 2020; Tian *et al.* 2019). While calibration with observational datasets is often recommended, Daines *et al.* (2016) found that projected changes do not vary considerably based on calibration techniques. Therefore, the extent of potential biases should not hinder assessments of seasonality and projected change.

Climate sensitivity assessments for CMIP5 models largely attribute model spread to cloud parameterizations (e.g., Vial *et al.* 2013). CanRCM4 has a relatively high transient climate response compared to other NA-CORDEX RCMs (the mean global temperature change due

Table 2.1: CanRCM4 variables used, time scale of available output, and method of acquisition (mean or point measurement). All means are taken using a 20 minute time step/interval.

Variable	**Time Scale**	**Method**
Near-surface (10 m) wind speed	1-hr or 3-hr	Mean
Surface sensible heat flux	1-hr or 3-hr	Mean
Surface latent heat flux	1-hr or 3-hr	Mean
Eastward downward wind stress	6-hr	Mean
Northward downward wind stress	6-hr	Mean
Near-surface (2-m) air temperature	1-hr or 3-hr	Mean
Surface air pressure	1-hr or 3-hr	Time point
Near-surface (2-m) specific humidity	1-hr or 3-hr	Mean
Sea ice area fraction	Daily	Mean
Surface downwelling shortwave radiation	1-hr or 3-hr	Mean
Column water vapour	6-hr	Mean
Column condensed (liquid & ice) water content	6-hr	Mean
Cloud area fraction	1-hr or 3-hr	Mean

to CO_2 doubling, having increased at 1% per year; Bukovsky & Mearns 2020). Challenges in cloud parameterizations also impact representation of surface solar irradiance, leading to biases (Nam *et al.* 2012; Stanfield *et al.* 2014) that are compounded by difficulties in representation of clear-sky radiative transfer (Wild 2008). In an assessment of model fluxes in 43 CMIP5 models, Wild *et al.* (2015b) found a climatological annual mean bias of 11.2 W/m^2 for shortwave radiation in CanESM2 using 760 observation sites. This compared to a multi-model mean bias of 7.4 W/m^2 (Wild *et al.* 2015b). There is high potential for bias in CanRCM4 output DSR, and therefore modelled PV potential. However, Wild *et al.* (2015a) tested the sensitivity of PV power projections to irradiance biases, and found no meaningful influences on projected absolute PV change.

Sea ice and sea ice change under global warming will have a critical impact on the climate in far northern Canada. Sea ice and sea surface temperature in CanRCM4 is taken from CanESM2 (Scinocca *et al.* 2016). Assessments of CanESM2 sea ice have revealed a large underestimation (bias) in sea ice extent, particularly in the summertime, where it is the lowest of all CMIP5 models (Stroeve *et al.* 2012). This is also true over the Canadian Arctic, with sea ice projections further limited by the relatively coarse spatial resolution of CanESM2 (Kushner *et al.* 2018). CanESM2 representation of sea ice in the Canadian Arctic Archipelago is less than half of that observed, with practically ice-free summers reached by as early as present day (Kushner *et al.* 2018).

All climate models contain biases relative to real-world conditions, and many bias correction techniques have been developed, from simple to complex. Due to grid cell averaging, CanRCM4 model output will be inherently different from point values for any given location, including our focal communities. In this study, we do not adjust CanRCM4 output to correct for potential model biases. While CanRCM4 will contain biases, we assume that these will remain constant in time, so that change in climate will be reliably reproduced. Similar assumptions are made by Ravestein *et al.* (2018) in their assessment of vulnerability of European wind and solar power to climate change. The considerable sea ice underestimation in CanRCM4/CanESM2 can be expected to impact time of emergence, biasing when robust changes in wind speed and solar irradiance become apparent. This early-emergence bias, however, will not affect the absolute relationship of these variables with sea ice; that is, it will affect the *when* but not the *if*.

Chapter 3

Methods

3.1 Communities and domain of focus

Das & Canizares (2016b) assessed 13 communities in Nunavut and recommended five with the strongest case for renewable energy investment: Arviat, Baker Lake, Iqaluit, Rankin Inlet, and Sanikiluaq. These five communities all showed potential for at least 20% operation and maintenance cost savings, 34% reductions in CO_2 emissions, and 34% renewable energy mix (Das & Canizares 2016b). As typically done when performing renewable energy site assessments, Das & Canizares (2016a) used historical climate means to assess feasibility of implementation. We have used their results to guide selection of communities for in-depth analysis, with the aim of furthering knowledge of current and future renewable energy potential and reliability.

To represent these communities of focus, model output was extracted from the closest grid cell centre to the community. Due to the relatively coarse resolution of CanRCM4, coastlines and small islands are not always well resolved. Figure 3.1 overlays actual coastlines with the CanRCM4 land versus water grid cells to highlight differences between the model and the real world. The CanRCM4 grid cell corresponding to Sanikiluaq (an island in Hudson Bay) is classified as ocean, and therefore Umiujaq was also selected as an analogue for Sanikiluaq. Umiujaq is located approximately 200 km east and 100 km north of Sanikiluaq (latitudes of 56.54°N and 55.55°N, respectively), along the eastern coast of Hudson Bay. While the coastal location of Umiujaq will certainly experience differences relative to an offshore island, it will be a useful comparison to an ocean grid cell which is subject to different physical parameterizations in CanRCM4. An analogue for Iqaluit was also chosen and referred to hereafter as 'Iqaluit Coastal Point'. Due the coarse resolution, Frobisher Bay is not well resolved and the corresponding grid cell for Iqaluit is not represented as a coastal location. A coastal grid cell in close proximity was selected for Iqaluit Coastal Point. Finally, an additional community, Sachs Harbour, Northwest Territories was selected

as there are ongoing pilot projects and on-the-ground research related to renewable energy implementation in the community.

In total, eight focal communities/locations will be assessed in detail in this paper: Arviat, Baker Lake, Iqaluit, Iqaluit Coastal Point, Rankin Inlet, Umiujaq, Sachs Harbour, and Sanikiluaq. In addition, a larger study area was selected to include the Yukon, Northwest Territories, and Nunavut, including the entirety of Hudson Bay. The study area also includes the northern portion of many provinces. The northernmost extent of the study area was determined by the northern extent of CanRCM4, with 2 grid cells along the boundary clipped. Figure 3.1 shows the locations of the eight locations of focus and larger study area domain.

3.2 Seasonal definitions

Rather than the boreal seasons that are commonly used (e.g., for study of Arctic cyclone activity (Sepp & Jaagus 2011)), seasons in the following study are defined as January-February-March (JFM, winter), April-May-June (AMJ, spring), July-August-September (JAS, summer), and October-November-December (OND, autumn). This selection was made to align with sea ice activity, which has considerable impacts on weather and climate in the far north.

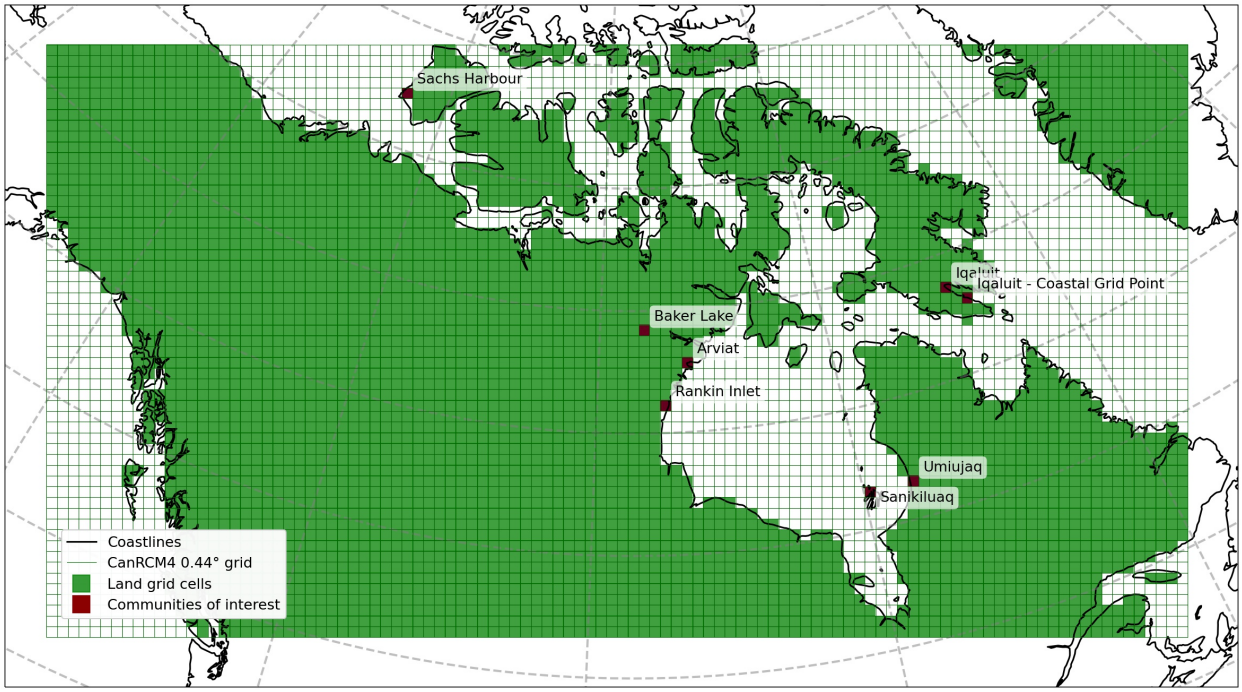

Figure 3.1: Study area overview map indicating the locations of the eight communities of focus and community analogues. Projection: rotated pole (pole latitude 42.5°, pole longitude 83°).

These seasons correspond with timing of maximum and minimum sea ice extent, as well as onset of freeze and melt (Francis & Vavrus 2015), and are frequently used for analyses of Arctic climate and weather (e.g. Candlish *et al.* 2015; Francis & Vavrus 2015; Overland & Wang 2010).

3.3 Wind power potential

3.3.1 Extrapolating wind speed to turbine hub height

To determine potential wind energy, 10 m wind speed from model output must first be extrapolated to turbine hub height (typically 20 to 100 m). This can be done using one of two methods:

1. Empirically derived power law profile:

$$v(z) = v_r \left(\frac{z}{z_r}\right)^{\alpha} \tag{3.1}$$

   where $v(z)$ is the velocity at height z, z_r is the reference height, and α is an empirically derived coefficient commonly taken to be 1/7 (Manwell *et al.* 2002).

2. Theoretically derived logarithmic wind speed profile, which can be used with or without stability correction from the Monin-Obukhov Similarity Theory (MOST):

$$v(z) = \frac{u_*}{k} \left[ln\left(\frac{z}{z_0}\right) - \Psi\left(\frac{z}{L}\right)\right] \tag{3.2}$$

   where z_0 is the roughness length, $k = 0.4$ is the Von Karman constant, u_* is the friction velocity, L is the Monin-Obukhov (MO) length, and Ψ is the empirically determined MO similarity function related to the dimensionless wind shear.

Due to its simplicity, the power law is commonly used in engineering applications for extrapolation of wind speeds. The exponent alpha can be empirically determined for locations based on observed wind speed data. However, wind profiles in the neutral boundary layer typically follow the logarithmic profile, and so this form is preferable. The shape of the log profile varies considerably from strictly logarithmic depending on boundary layer stability; the term Ψ corrects for atmospheric stability. The logarithmic profile with MOST is most suitable for low-altitudes, such as the turbine hub-heights used in this study (Optis *et al.* 2014).

The similarity functions used in CanRCM4 were used for this extrapolation. Under stable conditions the Beljaars and Holtslag similarity function is used (Beljaars & Holtslag 1991):

$$-\Psi = a\frac{z}{L} + b\left(\frac{z}{L} - \frac{c}{d}\right) exp\left(-d\frac{z}{L}\right) + \frac{bc}{d} \tag{3.3}$$

where $a = 1$, $b = 2/3$, $c = 5$, and $d = 0.35$. Under unstable conditions the Dyer function is used (Abdella & McFarlane 1996):

$$\Psi = 2\ ln\left(\frac{1+x}{2}\right) + ln\left(\frac{1+x^2}{2}\right) - 2\tan^{-1}(x) + \frac{\pi}{2} \tag{3.4}$$

where $x = (1 - 16z/L)^{1/4}$. These flux-profile relationships have been empirically determined from various micrometeorological experiments (Arya 2001; Beljaars & Holtslag 1991). The Monin-Obukhov length (L) is given by:

$$L = \frac{\theta_{v0}\ c_p\ \rho\ u_*^3}{k\ g\ H_{v0}} \tag{3.5}$$

where θ_{v0} is the virtual potential temperature, c_p is the specific heat capacity of the air, g is acceleration due to gravity, and H_{v0} is the virtual heat flux. The specific heat capacity of air at standard atmospheric conditions was used in all calculations (1004.64 J kg^{-1} K^{-1}). L measures relative importance of mechanical shear-generated turbulence versus buoyancy-driven turbulence (Arya 2001; Foken 2006). The absolute value of L represents the height at which buoyancy-driven turbulence dominates mechanical shear-generated turbulence (Overland 1985). Therefore, when $|L|$ is large, mechanical mixing is dominant. Close to the surface, wind shear typically dominates ($z << |L|$) (Arya 2001; Overland 1985). Using the variables available in CanRCM4 output, the required parameters can be determined through the Ideal Gas Law (Arya 2001):

$$\rho = \frac{m\ p}{R\ T} \tag{3.6}$$

$$m = \frac{0.028966}{1 + 0.61q} \tag{3.7}$$

where q is the specific humidity.

$$\theta_{v0} = T_0\ (1 + 0.61q) \tag{3.8}$$

$$T_0 = T + \frac{z\ g}{c_p} \tag{3.9}$$

$$H_v = H_s + \alpha_\theta H_l \tag{3.10}$$

where

$$\alpha = \frac{0.61\ c_p\ \Theta}{L_e} \tag{3.11}$$

and L_e is the latent heat of evaporation, 2.501×10^6 J/kg.

Determining friction velocity and roughness length

CanRCM4 uses the Canadian Land Surface Scheme 2.7 (CLASS). Within CLASS, a static roughness length is assigned to soil, ice, snow and four different vegetation classes, interpreted to be the maximum roughness length for that vegetation class (at peak vegetation height). Each land grid cell can therefore contain up to four subareas: bare soil, snow over bare soil, vegetation over soil and vegetation over snow (Sun & Verseghy 2019). At each time step, the characteristics of the vegetation and snow/bare ground are determined and aggregated to determine instantaneous roughness length (Verseghy 2009). Adjustments are made to account for orographic roughness length where necessary (Verseghy 2009). Roughness lengths and displacement heights therefore vary in the model due to vegetation height (for crop areas only) and snow or ice cover.

Instantaneous roughness length is not available as part of CanRCM4 output. Similarly, while all other parameters required in Equation (3.2) are available on a 1- or 3-hourly basis, friction velocity must be calculated using eastward and northward downward wind stress (τ_0), which is only available on a 6-hrly basis in CanRCM4 output. Wind stress is related to u_* by:

$$u_* = (\tau_0/\rho)^{1/2} \tag{3.12}$$

One of these two unknown parameters (friction velocity or roughness length) can be calculated at a 3-hourly basis from Equations 3.2 and 3.11, if the other parameter is known. Three methods of determining these parameters were explored:

1. Assuming a temporally static roughness length, calculate friction velocity from 6-hourly wind stress using Equation (3.12), then up-sample friction velocity to 3-hourly.

2. Assuming a temporally static roughness length, solve for friction velocity from Equation (3.2) at each time step.

3. Adjust Method 1 by first calculating friction velocity from 6-hourly wind stress, then solving for roughness length (z_0) at each time step using Equation (3.2).

Method 3 was selected based on minimizing error. The details of this analysis are laid out in Appendix B.

3.3.2 Air density in wind power estimates

CanRCM4 output has the significant advantage of already being specific to the local elevation. Therefore, extrapolation would only be required for the modest changes in altitude

to reach turbine hub height (e.g., 50 metres), meaning overall impacts will be very small (< 0.01 kg/m^2, which translates to $< 0.0001\%$ difference in power production). In addition, further simplifications would be required to make air density extrapolations, namely assuming a constant standard lapse rate of 6.5 K/km and zero humidity. Therefore, we use surface air density in power production calculations, computed via Equation (3.6), which accounts for changes in density due to pressure, humidity and temperature variation.

Standard air density (1.225 kg/m^3) is often assumed in wind resource estimates. However, model output variable air density has advantages, particularly in high-latitudes. First, cold temperatures result in an average air density that is much higher than standard conditions, and second, the considerable changes in temperature and humidity expected due to climate change will have equally large impacts on air density, and therefore wind power potential.

3.3.3 Semi-idealized wind power production model

The kinetic power of wind per unit area, commonly called wind power density, is a standard measure in wind resource estimates:

$$P = \frac{1}{2}\ \rho\ v^3 \tag{3.13}$$

However, actual wind power production is governed by turbine specifications (rotor swept area, turbine rotor/generator efficiency, cut-in and cut-out wind speeds) and fluid mechanics (Manwell *et al.* 2002). The Betz Limit states that maximum power output for a wind turbine is given by 16/27 times the wind power density:

$$P_{max} = \frac{16}{27}\ \frac{1}{2}\ \rho\ A\ v_z^3 \tag{3.14}$$

where A is the rotor swept area, ρ is air density and v_z is wind speed at hub height z. In practice, turbine efficiency rarely exceeds 50% of the wind power density (Carrillo *et al.* 2013). Individual wind turbines are characterized by a rated power (maximum theoretical power produced). If wind is less than the required "cut-in" wind speed, no power is produced; between the cut-in and "rated" wind speed, power will be produced following Equation (3.14) multiplied by a turbine and wind speed-dependent power production coefficient (c_p) instead of the Betz Limit; at the rated wind speed, the rated power is reached; and between the rated wind speed and "cut-out" wind speed power is produced at the rated power.[1] Power is not produced beyond cut-out wind speed, as turbine blades are stopped for safety reasons (Jerez *et al.* 2015a). In standard conditions ($\rho_0 = 1.225$ kg/m^3), the wind turbine power

[1] Assuming standard air density, $\rho_0 = 1.225$ kg/m^3.

production model can therefore be represented by:

$$P_0(v) = \begin{cases} 0 & \text{if } v < v_{cut-in} \\ c_p \ \frac{1}{2} \ \rho_0 \ A \ v^3 & \text{if } v_{cut-in} \leq v \leq v_{rated} \\ c_p \ \frac{1}{2} \ \rho_0 \ A \ v_{rated}^3 & \text{if } v_{rated} < v \leq v_{cut-out} \\ 0 & \text{if } v > v_{cut-out} \end{cases} \tag{3.15}$$

Most modern turbines use active power control with pitch regulation, for which the International Electrotechnical Commission (IEC) standard 61400–12–1 for power performance measurements recommends normalization of input wind speed to account for non-standard air density according to (International Electrotechnical Commission 2005):

$$v_n = v_{actual} \ \left(\frac{\rho}{\rho_0}\right)^{1/3} \tag{3.16}$$

Table 3.1 provides specifications of example wind turbines suitable for use in Arctic conditions and of a size appropriate for the power needs of the communities of focus, as identified by Das & Canizares (2016a). The turbines have a rated power of ∼900 kW and turbine hub heights at approximately 50 m. Figure 3.2 shows the actual power production curves for these turbines.

According to Jerez *et al.* (2015a), the most common values for cut-in, rated and cut-out speeds are 3.5, 13 and 25 m/s respectively. For simplicity of calculation, and because all wind power production is turbine specific, we employ a semi-idealized theoretical turbine power curve (i.e., power production model) that combines a practical power coefficient with a selected rated power of 900 kW and rotor swept area corresponding to turbine blades of length 26 m. While typically c_p varies with wind speed, we use a static value selected so that power production was reasonably consistent with real-world turbines. Carrillo *et al.* (2013) tested this approach using best-fit functions, and found it to be a good approximation for real-world turbines. Therefore, our power production model will use Equation (3.15) with v_n from Equation (3.16) given the model parameters in the last column of Table 3.1. Using this semi-idealized 900 kW turbine power model with a 50 m hub height ($M_{50m,900kW}$) we calculate power production potential per turbine, neglecting potential wake effects due to multi-turbine wind farm installations. Note that in real world situations, turbines would be selected to maximize power output given the wind speed characteristics of site locations.

3.3.4 Wind power potential

Wind power potential (WPP) for a specified time period is typically estimated for engineering applications using the Weibell wind speed distribution and average wind speed for the site

Table 3.1: Specifications of two example wind turbines (Emergya Wind Technologies n.d.[a],[b]), and the semi-idealized 900 kW turbine model ($M_{50m,900kW}$) created for wind power production estimates.

Model	DW54 900kW	DW61 900kW	$M_{50m,900kW}$
Manufacturer	Emergya Wind Tech.	Emergya Wind Tech.	N/A
Rated power (kW)	900	900	900
Diameter (m)	54	61	52
Rotor swept area (m^2)	2290	2922	2124
Hub height (m)	40, 50 or 75	46 or 69	50
Cut-in speed (m/s)	2.5	2.5	2.5
Rated speed (m/s)	13.5	11.5	11.34
Cut-out speed (m/s)	25.0	25.0	25.0
c_p	variable max: ~ 0.45	variable max: ~ 0.45	0.475

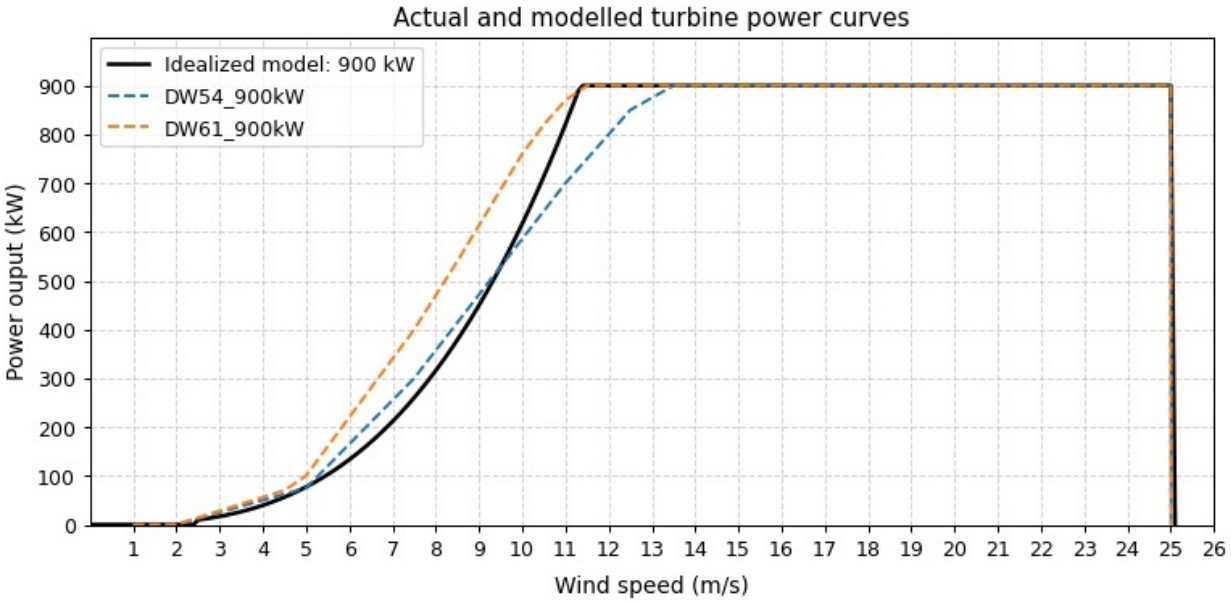

Figure 3.2: The semi-idealized power production model to be used (black line) along with two sample power curves from actual turbines realistic for the communities of focus (dotted lines; see Table 3.1). All power curves at standard air density (1.225 kg/m^3).

(Manwell *et al.* 2002). CanRCM4 output consistency, both spatially and temporarily, allows us to directly calculate *WPP*:

$$WPP = \sum_{i=1}^{N} P_{n,i} \Delta t \tag{3.17}$$

where N is the number of time intervals of size Δt for the period of interest, and $P_{n,i}$ is the normalized power output for time interval i. Normalized power output is calculated according to $M_{50m,900kW}$, as described above. *WPP* will be calculated using two temporal scales: daily wind power production (WPP_{day}) for comparison between seasons; and annual wind power production (WPP_{annual}, commonly called Annual Energy Production) a common measure in engineering applications which estimates the total amount of electrical energy a turbine produces over a year, often expressed in megawatt hours (MWh).

3.4 Solar photovoltaic power potential

Solar photovoltaic power potential (*SPP*) can be given by (Mavromatakis *et al.* 2010):

$$SPP = P_m \cdot \eta_t \cdot \frac{DSR}{DSR_0} \cdot f_{PV} \tag{3.18}$$

where P_m is the rated capacity of the PV array at standard test conditions, DSR is the incident solar irradiance (the surface downwelling shortwave radiation from the climate model), DSR_0 is the incident solar irradiance at standard conditions (1000 W/m^2), η_t accounts for panel efficiency due to non-standard atmospheric conditions, and f_{PV} is a derating factor that accounts for all other impacts to real-world power performance (e.g., losses from panel age, soiling, wiring losses, etc.; Gernaat *et al.* 2021; Mavromatakis *et al.* 2010; Quitoras *et al.* 2020). We assume these factors will remain constant and assign a static value of 0.85 for f_{PV}, similar to previous studies (e.g., Gernaat *et al.* 2021). P_m is taken to be 900 kW, for comparability with the 900 kW wind power production model.

Module performance is dependent on PV array cell temperature (T_c) via η_t (Mavromatakis *et al.* 2010; Skoplaki & Palyvos 2009):

$$\eta_t = 1 + \gamma(T_c - T_0) \tag{3.19}$$

where $T_0 = 25$ °C (cell temperature at standard conditions) and γ is the temperature coefficient of power, taken to be -0.0045 °C^{-1}, which is the average for monocrystalline silicon solar panels at $T_0 = 25$ °C (Skoplaki & Palyvos 2009). Many different models for estimating the cell temperature from meteorological conditions have been developed (e.g., see Mavro-

matakis *et al.* 2014).[2] Mavromatakis *et al.* (2014) compared seven models for determining cell temperature, and reported best performance for the relationship developed by King *et al.* (2004):

$$T_m = T_a + DSR \cdot e^{(a+b \cdot v_{10})} \tag{3.20}$$

$$T_c = T_m + \frac{DSR}{DSR_0} \cdot \Delta T_0 \tag{3.21}$$

where T_m is the module temperature and v_{10} is the wind speed (m/s) measured at 10 m. Values of a and b are empirically derived by King *et al.* (2004) for wind speeds up to 18 m/s, and differ based on module type and mounting configuration. ΔT_0 is the difference between the module and cell temperatures at reference conditions (1000 W/m^2), which is usually between 2 and 3°C, or zero for thermally-insulated back surfaces (King *et al.* 2004). We use a standard configuration of open-rack mounting and glass/polymer module (as tested by Mavromatakis *et al.* (2014)), giving a = -3.56 °C m^2/W, b = -0.075 s m^1, and ΔT_0 = 3°C (King *et al.* 2004). As per the relationships above, higher temperatures result in reduced PV array efficiency, while lower temperature result in higher efficiency. Equations (3.20) and (3.21) were calculated using the library pvlib-python v0.8.1 (Holmgren *et al.* 2018).

Optimal power output is achieved when incident solar radiation is at right angles to PV panels, achieved through use of tilted panels, which also benefit from ground-reflected solar radiation. We assume panels are horizontally-oriented, as in previous studies (e.g., Köberle *et al.* 2015; Wild *et al.* 2015a), and therefore reflected radiation (proportional to global horizontal radiation[3]) and performance gains from use of tilted modules are not considered. Our results represent a lower-limit on solar PV potential in this sense. These factors are assumed to remain unchanged over time, although it should be noted that changes in surface albedo due to snow and ice loss in Arctic regions may be considerable over the 21st century.

3.5 Assessing robust and substantial changes

The magnitude of the forced change due to climate change (the signal) was compared to the internal climate variability (the noise) to identify potentially robust and substantial responses

[2]Many recent studies (e.g. Gernaat *et al.* 2021; Jerez *et al.* 2015b; Pérez *et al.* 2019) have used a simple linear approximation developed by TamizhMani *et al.* (2003) to estimate cell temperature: $T_c = a \cdot T_a + b \cdot DSR - c \cdot v + d$, where T_a is the ambient temperature, v is wind speed, and coefficients are empirically determined and usually taken to be $a = 0.943$, $b = 0.028$ °C m^2/W, c = 1.528 °C s m^1, and d = 4.3 °C. However, this relationship is unreliable at wind speeds exceeding 10 m/s – a situation not uncommon in our study area – as it leads to erroneously low cell temperatures (Mavromatakis *et al.* 2014).

[3]Reflected radiation on a tilted surface is proportional to global horizontal irradiance (Demain *et al.* 2013): $R_\beta = \alpha G R_r$, where α is the ground albedo, β is the panel tilt angle with respect to the horizontal plane, and R_r is the transposition factor of ground reflection. Assuming constant radiance from the ground surface (it is ideally isotropic, Demain *et al.* 2013), R_r is given by: $R_r = \frac{1-cos(\beta)}{2}$.

using a signal-to-noise ratio (SNR, e.g., Christensen *et al.* 2007; Daines *et al.* 2016).

(1) Robustness

For projected time periods 30-year means were taken, and the differences between each realization and the ensemble mean of the reference period (1970-1999) were calculated (ΔP). The ensemble mean (μ_e) of these anomalies is interpreted as the forced change (signal, S), while the ensemble standard deviation (σ_e) of the reference period means (P_{ref}) is interpreted as internal climatic variability (noise, N). Robustness in therefore given by:

$$Robustness = SNR = \frac{\mu_e(\Delta P)}{\sigma_e(P_{ref})} \tag{3.22}$$

The greater the signal-to-noise ratio, the more robust the climate change response. A robust change is defined as SNR>1, when the change in ensemble mean exceeds the intra-ensemble standard deviation of the reference period. The goal is to identify robust climate shifts from its current (reference period) state. Similarly, time of emergence (ToE) of a climate signal is defined as the period when the SNR first exceeds one. These criteria are used by Abatzoglou *et al.* (2019), and similar methods with variations in the definition of the internal variability or significance thresholds are common (e.g., Christensen *et al.* 2007; Giorgi & Bi 2009; Hawkins & Sutton 2009, 2012; Kjellström *et al.* 2018; Mioduszewski *et al.* 2018). This measure will smooth out inter-annual variability by relying on standard deviation of 30-year means as a measure of noise. Therefore, we also employ a second measure of impact, substantiality.

(2) Substantiality

The climate signal is defined the same as for robustness: the ensemble mean of anomalies between a given period and the reference period (ΔP). To measure noise, the temporal variance of annual means in the reference period was calculated for each ensemble member, averaged over the 50 ensemble members, and then the square root was taken. Substantiality is therefore given by:

$$Substantiality = SNR = \frac{\mu_e(\Delta P)}{[\mu_e(Var_{ref}(P_a))]^{1/2}} \tag{3.23}$$

This measure will allow identification of changes in the mean which exceed the inter-annual variability within the reference period.

Note that the signal is defined the same for both substantiality and robustness (mean change), but that for robustness 'noise' measures the inter-ensemble variability, while for substantiality 'noise' measures temporal (inter-annual) variability of individual realizations, which are then averaged. As inter-annual standard deviation is greater than the inter-ensemble standard deviation, we expect substantiality will be a more conservative measure than robustness. A projected change may be *robust* in that it is detectable in 30-year

means, but perhaps not *substantial* in that the mean change is not distinguishable from current inter-annual variability.

3.6 Assessing influences on wind power: Partial correlation analysis

Changes in sea ice, storm activity, roughness length, and atmospheric stability have been suggested as potential causes of SWS increases (e.g., Mioduszewski *et al.* 2018), and therefore of wind power potential. Correlation and partial correlation analysis was used to assess the relationship between potential mechanisms of change and wind power while controlling for the effect of the remaining covariates. Partial correlation ($\rho_{XY \cdot Z}$) between factor X and Y while controlling for Z (a set of n controlling variables) is calculated as the correlation between the residuals resulting from the linear regressions of X with Z and of Y with Z (Lawrance 1976). The relationship can be represented using pairwise correlations (Lawrance 1976) as:

$$\rho_{XY \cdot Z} = \frac{\rho_{XY} - \rho_{XZ}\rho_{YZ}}{[(1 - \rho_{XZ}^2)(1 - \rho_{YZ}^2)]^{1/2}} \tag{3.24}$$

Monthly statistics as described in Table 3.2 were used for analysis. To remove potential confounding seasonal variations, the seasonal cycle was removed from monthly means and then data was detrended using a first degree polynomial fit. The seasonal and temporal trend was calculated from the ensemble mean for the 30-year period on which correlations were taken (1970-1999).

Storminess measures

Storms are associated with high wind speeds, strong pressure gradients, and, oftentimes, precipitation events. Storminess can be measured directly using near-surface wind speeds or

Table 3.2: Variables considered in correlations with wind power potential.

Variable	Measure	Statistic
Atmospheric stability	$\zeta = z/L$	Median
Storminess	Near-surface winds	Storm count
Roughness length	z_0	Median
Air density	Near-surface density	Mean
Sea ice	Sea ice concentration	Mean

indirectly using geostrophic winds as proxy, or, commonly, via sea level pressure or lower-tropospheric vorticity (e.g., Screen *et al.* 2011). Near-surface wind speed methods often suffer from limited availability of long-term station data or inconsistencies resulting from changes to measuring techniques, instruments, or station surroundings over time (WASA Group 1998). Another potential limitation of direct wind speed-based measures is that wind speeds over the ocean can be affected by atmospheric stability (Kent *et al.* 2013) and sea ice changes (which also impact atmospheric stability, e.g., Knippertz *et al.* 2000; Mioduszewski *et al.* 2018). However, as climate model output does not suffer from data quality or consistency concerns, and use of partial correlation analysis should account for interdependent factors over ocean areas, we decided on a wind speed-based index of the storm climate, which we denote storminess.

Storm intensity is typically defined by near-surface wind speed (Feser *et al.* 2015). Weisse *et al.* (2005), for example, used hourly 10 m wind speed output from a regional climate model (RCM) simulation for the northeast Atlantic and the North Sea and compared it with available station data to assess storminess. They identified storms using the Beaufort scale and near-surface instantaneous wind speed maxima, concluding that the RCM was able to simulate storm indices based on near-surface wind for the marine areas in their study area (Weisse *et al.* 2005). Earl *et al.* (2013) used near-surface wind speed exceedances of predefined thresholds to assess changes in UK storminess from 1980-2010 using station data. Smits *et al.* (2005) identified 97-hr near-surface wind speed maxima, and then ranked all events in the 41-year record, labelling them as weak (*average* occurrence 30 times per year), moderate (10 times per year), or strong events (2 times per year), in order to assess trends over time. Atkinson (2005) identified storm events in the circum-Arctic coastal region with potential coastal geomorphological impacts as those that exceeded 10 m/s for at least 6 hours, and further included 'lulls' and 'shoulder' events that exceeded the arbitrarily defined 7 m/s 'continuity threshold'. Redilla *et al.* (2019) used a similar method to assess change in high wind events, but selected event thresholds (both wind speed and duration) to produce a desired sample size of events in the control period. Other studies measure changes in storminess by changes in wind speed extremes, such as 99th percentile wind speed (e.g., Donat *et al.* 2011). An increase in the 95 or 99th percentile wind speed, for example, indicates an increase in storminess, possibly due to more powerful or more frequent storms (Weisse *et al.* 2005). Beniston *et al.* (2007) identified wind storms using RCM output near-surface wind speeds in their assessment of future extreme events in Europe through 3 indices: change in extreme wind speed percentiles; exceedances of 90th, 95th and 99th percentile reference period wind speeds; and exceedances of Beaufort scale thresholds.

Our methods are based on those of Beniston *et al.* (2007) and Atkinson (2005), using 3-hr mean near-surface wind speeds from CanRCM4. Threshold wind speeds are defined

for each individual grid cell as the 95th percentile near-surface wind speeds of the 1970-1999 reference period across all realizations. This threshold will take into account physical differences in locations (e.g., roughness lengths), while still allowing identification of change over time. Windstorms are then identified as minimum 6-hr duration wind speeds greater than the threshold speed. Lulls during which the wind speed falls below the threshold for <6 hrs and then recover are also flagged as storm events. For ease of computation, individual time points are flagged as storm (1) or not-storm (0) based on these criteria, and then are averaged across the month to produce metric indicating the frequency of exceedance of the control period 95th percentile.

Other measures

The influence of stable or unstable stratification on wind speed profiles in the surface layer, the lowest part of the boundary layer, is measured using the Obukhov stability parameter $\zeta = \frac{z}{L}$ (Arya 2001; Overland 1985), where L is defined in Equation (3.5).

Air density is calculated from model output using Equation (3.6). Sea ice concentration is used to represent sea ice, and is directly available from model output as daily means.

Roughness length is calculated from model output as detailed in Appendix B. Roughness length is calculated instantaneously at each time-step using logarithmic wind law with stability correction. The z_0 parameter therefore partially acts as a correction factor for temporal and spatial averaging of model output. However, median roughness lengths follow expected relationships with land cover: high roughness lengths are found over forested regions, lower values over tundra or grasslands, and lowest roughness lengths over open ocean.

3.7 Assessing influences on photovoltaic power

To assess individual influences of changes in solar irradiance, temperature, and wind speed on projected changes in PV potential, mean *SPP* was also calculated using a combination of future and reference period (1970-1999) inputs:

$$SPP_{proj,G} = SPP(G_{2070-99}, T_{a,1970-99}, v_{10,1970-99})$$

$$SPP_{proj,T_a} = SPP(G_{1970-99}, T_{a,2070-99}, v_{10,1970-99})$$

$$SPP_{proj,v_{10}} = SPP(G_{1970-99}, T_{a,1970-99}, v_{10,2070-99})$$

These values were compared to the mean of the reference period *SPP*:

$$SPP_{ref} = SPP(G_{1970-99}, T_{a,1970-99}, v_{10,1970-99})$$

giving, for each variable (var) of interest, the absolute impact of changes in this variable:

$$\Delta SPP_{var} = SPP_{proj,var} - SPP_{ref}$$

As solar irradiance, temperature and wind speed are not statistically independent, this calculation is approximate.

In addition to the calculations above, partial correlation analysis was performed between DSR and potential influencing factors. Partial correlation methods are described in Section 3.6. Potential factors include model output fields of total cloud fraction (CLT), column condensed liquid/ice water (CLW, a proxy for cloud characteristics, as CLT includes all clouds); column water vapour (CWV), and sea ice (SIC). Aerosol optical depth is not available CanRCM4 output. As with the wind power correlation analysis, the seasonal cycle was removed from monthly means and then data was detrended using a first degree polynomial fit before correlations were taken. For DSR only, the seasonal cycle was removed using division rather than subtraction to assess variations relative to seasonal means. This method accounts for the seasonally varying maximum possible DSR, which is controlled by top of atmosphere solar irradiance and impacts the absolute magnitude of DSR response to potential influencing factors.

3.8 Assessing stability of the power system

The dependence of wind power and solar power on weather conditions implies that both short-term (sub-annual) and longer-term (inter-annual) temporal climate variability can make grid integration challenging (Natural Resources Canada 2021), with potential impacts on power stability. Inter-annual variability (IAV) and inter-daily (IDV) variability are used to assess these fluctuations in power production through use of a coefficient of variation,

$$IDV = \frac{\sigma(P_{daily})}{\mu(P_{daily})} \tag{3.25}$$

$$IAV = \frac{\sigma(P_{annual})}{\mu(P_{annual})} \tag{3.26}$$

where P_{annual} is the annual power production and P_{daily} is daily power production. This method was used by Jung & Schindler (2018) to assess inter-annual variability in wind energy resources in Germany, and by Jung & Schindler (2020) for assessment of sub-annual variability of global wind energy resources as estimated through wind speed distributions.

Chapter 4

Results and analysis

4.1 Wind power potential

This section will first consider wind power potential (WPP) variability and change for the communities of focus and then for the entire domain. Potential causes of change will then be assessed.

4.1.1 Communities of focus

Wind power potential in Canada's maritime far north is relatively high compared to many more southern, inland regions of the country. The communities of focus are located on the coast or in near-coastal areas of comparatively moderate to high mean wind power potential relative to the domain average. This fact contributes to their high feasibility for renewable investment, as found by Das & Canizares (2016b). Sachs Harbour (a coastal community on the Beaufort Sea; not selected by Das & Canizares (2016b)) has the lowest community annual wind power potential (WPP_{annual}). However, WPP_{annual} is fairly comparable between communities; all lie within the range of ∼3200 to ∼4000 MWh (Table 4.1 and Figure 4.1). Sachs Harbour's 1970-1999 mean WPP_{annual} of 3197 MWh is only slightly lower than Iqaluit (3289 MWh). The highest WPP_{annual} is for the island community of Sanikiluaq at 3961 MWh.

Seasonally, mean WPP_{day} is greatest in OND for all communities, usually followed by JAS. Across all communities, mean WPP_{day} in JFM and AMJ are comparable, but the season cycle is not in exact alignment for the individual sites (Figure 4.1). All communities are projected to experience an increase in mean WPP_{annual} across the 21st century, although the magnitude and seasonality of the change vary by location. Annual increases of over 12% are projected by the end of the 21st century in Sanikiluaq, the (only) ocean grid cell location, with the highest control period WPP_{annual}. Smallest projected change occurs in Baker Lake and Rankin Inlet, with increases of 2.2% and 2.9% respectively (Table 4.1). Projected change

by season, presented in Figure 4.2, indicates that annual trends are largely driven by cold-season increases in potential energy production, which in some locations are partially offset by warm-season decreases. For all communities, projected WPP_{day} sees 'robust' increases (see Section 3.5) in JFM. JAS sees robust decreases (Sanikiluaq, Umiujaq) or no change in most communities (see Figure 4.2). Trends in AMJ and OND are variable based on location; while we project robust increases in WPP_{day} for most communities, some locations see robust decreases.

Emergence of robust changes in WPP_{day} occurs in the early 21st century for most communities, with earliest emergence in JFM, followed by OND and AMJ (Figure 4.2). However, 'substantial' changes (see Section 3.5) never emerge for the communities of Arviat, Baker Lake, and Rankin Inlet. Where substantial changes do emerge, it is not until the end of the 21st century, with the exception of Sanikiluaq and Umiujaq in southern Hudson Bay.

Inter-annual variability (IAV) and inter-daily variability (IDV) were also assessed across the 21st century to measure internal variability at different time scales using the appropriate coefficient of variation (see definitions in Section 3.8). IAV measures potential year-to-year changes in total power. IDV assesses power intermittency, capturing intra-seasonal day-to-day changes as well as inter-season variability. These issues are important for determining reliability of a wind energy-based power system.

Both IAV and IDV decrease over the 21st century for the communities of interest. Some communities see considerable decreases in ensemble mean IAV over the 21st century (up to 16%), while others see very small changes of less than 1% (see Table C.1). IDV experiences more consistent changes, decreasing between 2.5 and 10% by the end of the 21st century for all communities, with largest change in Iqaluit, and smallest (almost none) in Baker Lake (Table C.1). Changes in IDV are likely due to reductions in inter-seasonal differences. Figure 4.3 presents the ensemble mean trend in WPP_{day} across the 21st century for the city of Iqaluit, also showing the ensemble standard deviation and 5th and 95th percentiles. As can be seen in Figure 4.3, and is also true for other communities (see Appendix D and Figure 4.2), increases in JFM WPP_{day} are largely responsible for the annual change. Since JFM has the lowest or second lowest WPP_{day} in the reference period, this cold season increase reduces the seasonal cycle of wind power production.

Table 4.1: Ensemble mean WPP_{annual} for the communities of focus in the reference period (1970-1999), and change by the end of the 21st century (2070-2099; columns 2 to 4, rounded to the nearest whole number for clarity). The robustness (column 5, dimensionless) and substantiality (column 6, dimensionless) of the change are presented, with robust or substantial changes (>1) boldface (see Section 3.5).

	WPP_{ann} (MWh) 1970-99	ΔWPP_{ann} (MWh) 2070-99	$\%\Delta WPP_{ann}$ 2070-99	Robustness of change	Substantiality of change
Arviat	3552	180	5	**4.59**	0.96
Baker Lake	3473	82	2	**2.16**	0.43
Iqaluit	3289	231	7	**6.19**	**1.05**
Iqaluit CL	3301	256	8	**6.61**	**1.19**
Rankin Inlet	3804	113	3	**2.87**	0.62
Sachs Harbour	3197	256	8	**5.98**	**1.07**
Sanikiluaq	3961	486	12	**12.80**	**2.58**
Umiujaq	3418	302	9	**6.97**	**1.69**

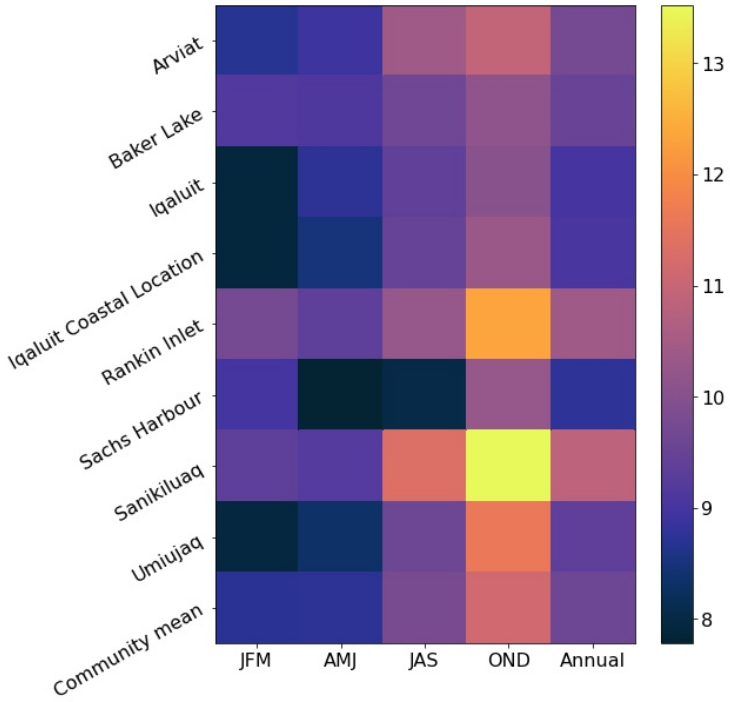

Figure 4.1: Ensemble mean WPP_{day} (MWh) by season and community in the reference period (1970-1999).

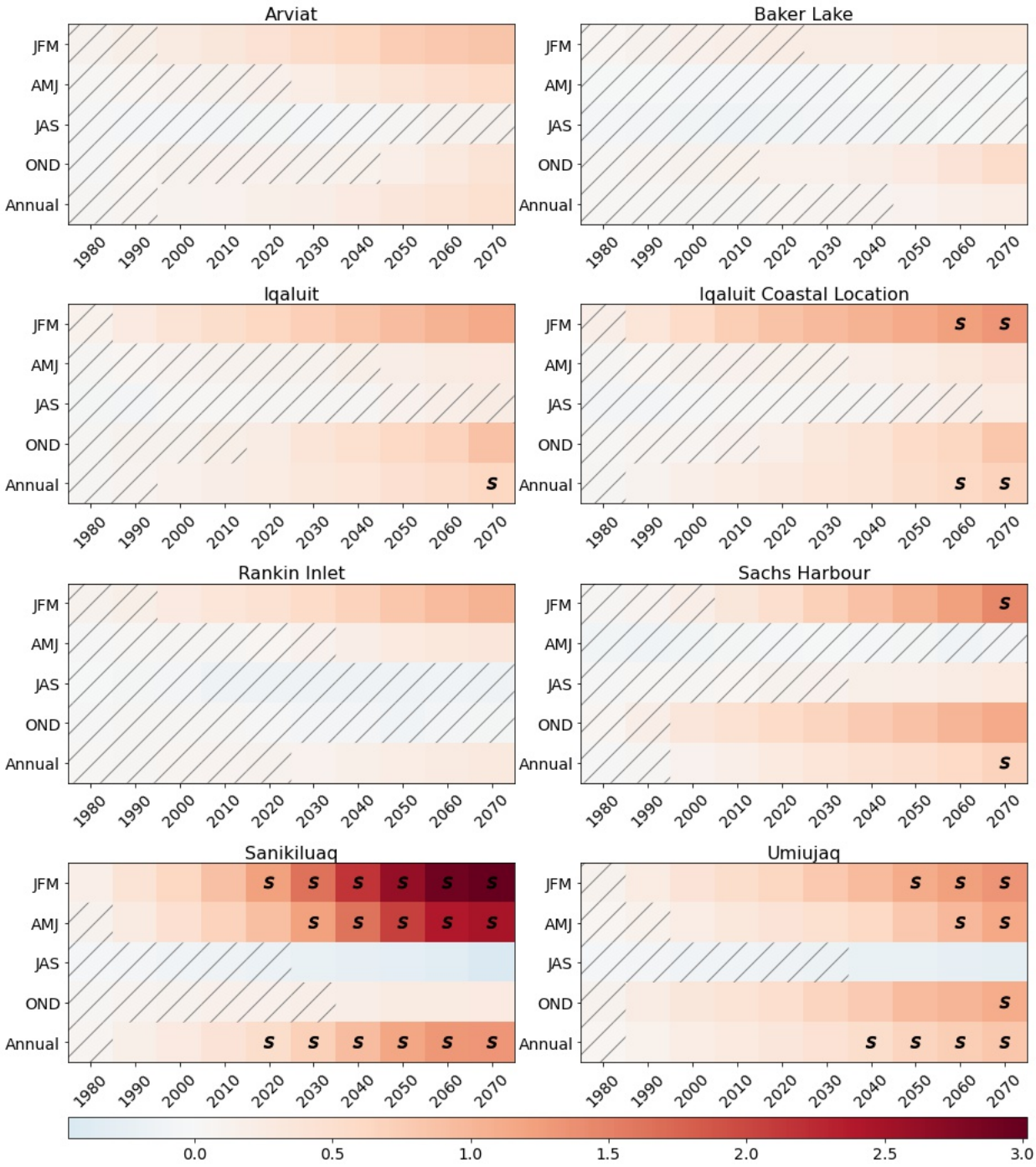

Figure 4.2: Absolute difference in WPP_{day} (MWh) from the 1970-1999 reference period by season. Mean WPP_{day} was computed over a 30-year rolling window by decade. Axis labels indicate the starting year of the period, e.g., 2070 corresponds to 2070-2099. Non-robust changes are masked with hatching. Substantial changes are indicated with a boldface "S". Each panel represents values from the model grid cell closest to the stated community.

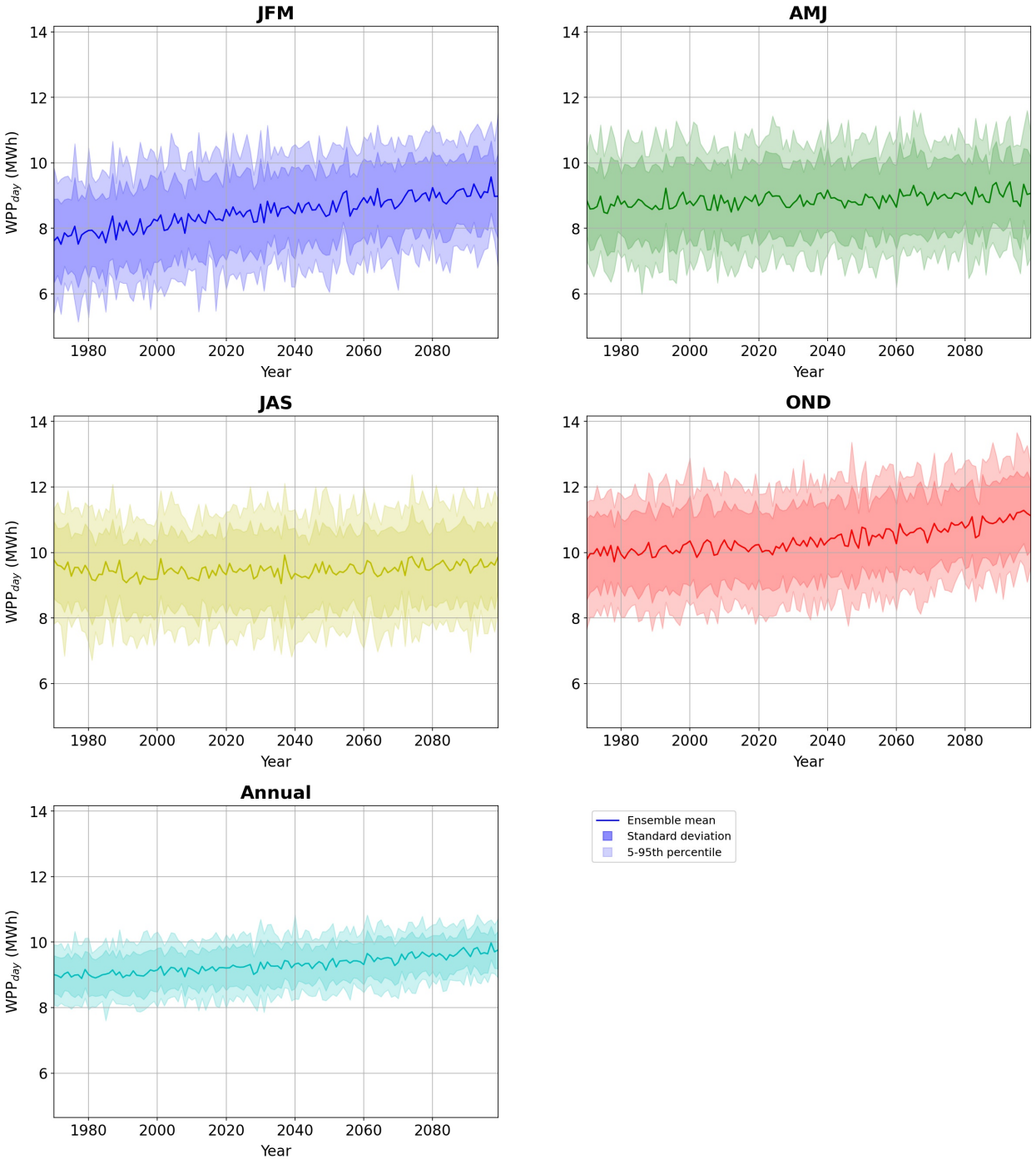

Figure 4.3: Daily wind power potential (WPP_{day}; MWh) projections for Iqaluit by season and annually from 1970 to 2100, showing the ensemble mean (dark line), standard deviation (dark shading), and 5th to 95th percentiles (light shading). Plots for other communities of focus can be found in Appendix D.

4.1.2 Northern Canada study area

Over the whole domain, annual mean WPP_{day} is generally greatest over ocean areas, including Hudson Bay, the Labrador Sea, and the portions of the Atlantic and Pacific Oceans included in the study area (Figure 4.4). Further north, the Beaufort Sea and Baffin Bay have lower annual mean *WPP* more comparable with continental areas. The continental regions east and west of Hudson Bay, as well as the Quebec-Labrador Peninsula, see higher than average *WPP*. The southern boundary of this domain aligns with the northern limit of the tree line, suggesting that it results from a transition in roughness length. Areas within the boreal forest (high roughness length) see the lowest average *WPP*, while the Canadian prairies (low roughness length) have moderate *WPP*. Across the study area, wind power potential in the reference period is greatest in cold seasons (OND, mean WPP_{day} of 9.8 MWh, and JFM, 8.2 MWh), with lowest mean WPP_{day} in AMJ (7.1 MWh; see Figure 4.5).

Robust change in 30-year mean WPP_{day} is projected for much of the study area, with the magnitude and sign of the change strongly related to latitude (Figure 4.4). The southern continental interior, much of Western Canada, and the Pacific Ocean see large, robust decreases in WPP_{day}, up to 20%, across the 21st century. Arctic regions which currently experience seasonal ice coverage as well as adjacent continental areas are projected to see robust increases in WPP_{day}, the most considerable being over ocean areas (increases up to 30%). This region of projected robust increase covers most of Nunavut, northern Quebec (including Nunavik), the Quebec-Labrador Peninsula, and the northern portions of NWT and the Yukon. Our measure of substantiality is more conservative than robustness. Substantial changes of mean WPP_{day} do not emerge for most land areas by the end of the 21st century. Only Arctic marine areas, coastal areas directly adjacent to these, and northern Quebec (east of Hudson Bay) are projected to experience substantial increases; while a smaller portion of the southern Canadian prairies and British Columbia is projected to see substantial decreases (Figure 4.4). However, considering the ensemble 5th and 95 percentiles of absolute difference in WPP_{day} (Figure 4.6), by the 2040-2069 period, most of changes are robust even at the 5th percentile, with the exception of northern continental regions.

Trends in WPP_{day} across the 21st century vary by season in both the sign and magnitude of change (Figure 4.5). Northern marine areas are generally projected to see robust increases in all seasons, with decreases only being found in Hudson Bay, Baffin Bay and the Labrador Sea in JAS. Largest increases in northern ocean areas are projected for JFM. However, Hudson Bay also sees large robust increases in AMJ, while the northwestern Canadian Arctic Archipelago has strong projected increases in OND and is the only region to see robust increases in JAS. The southern continental interior sees robust decreases in all seasons except OND, although changes are most prominent in JAS. Unlike the overall trend of decreasing

continental WPP_{day}, in OND much of the continent is projected to have robust increases in power production by the end of the 21st century. Robust decreases in power potential are projected over the Pacific Ocean in most seasons, with the exception of the southern areas in JAS and northern coastal areas in JFM. By the end of the 21st century, JAS is the only season which experiences a domain-averaged decrease in WPP_{day}, with the ensemble mean WPP_{day} becoming lower than AMJ at 7.1 MWh.

Both inter-annual (IAV) and inter-daily variability (IDV) are projected to decrease for Arctic marine and larger coastal regions, while continental interior regions see increases (Figure 4.7). Changes in IAV are considerable in some Arctic marine regions, with decreases of up to 30%, and similar magnitude IAV increases projected over parts of the Canadian prairies. However, large changes in IDV (up to 18%) are more widespread across northern marine regions, with a clear inverse relationship to *WPP* change: IDV decreases in regions of *WPP* increase, and increases in regions of *WPP* decrease. These changes in IDV are likely due to changes in the magnitude of seasonal differences. For example, in continental regions where IDV increases, the seasonal cycle is heightened: JAS (lower than average WPP_{day}) sees robust decreases, and OND (higher than average WPP_{day}) sees robust increases. Reasons behind trends in IAV are less clear. Changes in the Beaufort Sea could be due the reduced inter-annual variability of sea ice as sea ice is lost altogether. In any case, these results imply that in Arctic and adjacent coastal regions, inter- and intra-annual power potential is projected to become more stable, with reduced magnitude of seasonal *WPP* variations.

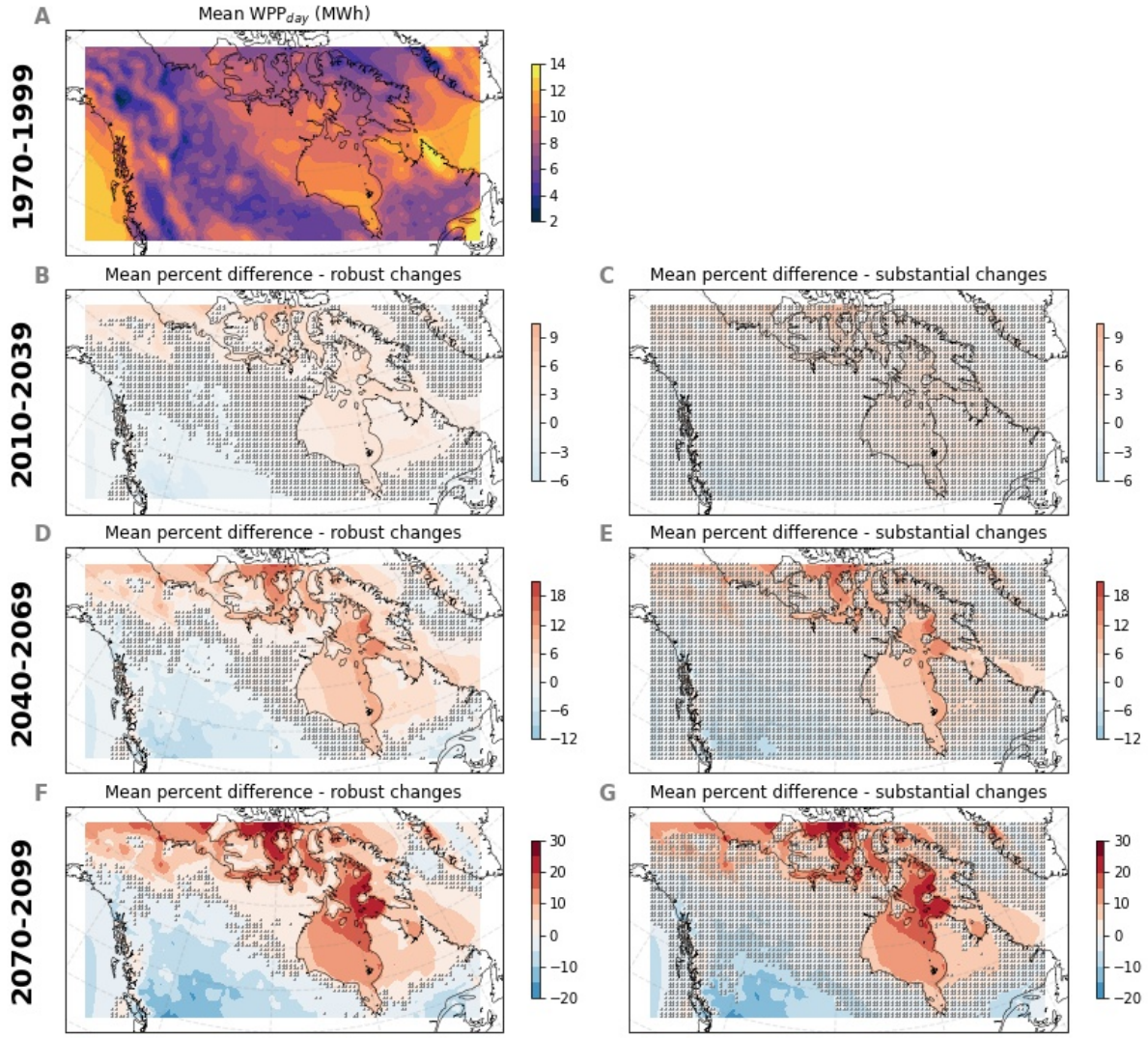

Figure 4.4: Ensemble mean reference period (1970-1999) WPP_{day} (MWh, panel A) and percent difference from the reference period (MWh) for the periods 2010-2039 (B and C), 2040-2069 (D and E), and 2070-2099 (F and G). Individual plot colourbars display the range of values for that plot, scaled so that colours are directly comparable between plots B to G. Non-robust (B, D and F) and non-substantial (C, E, and G) changes are masked with stippling.

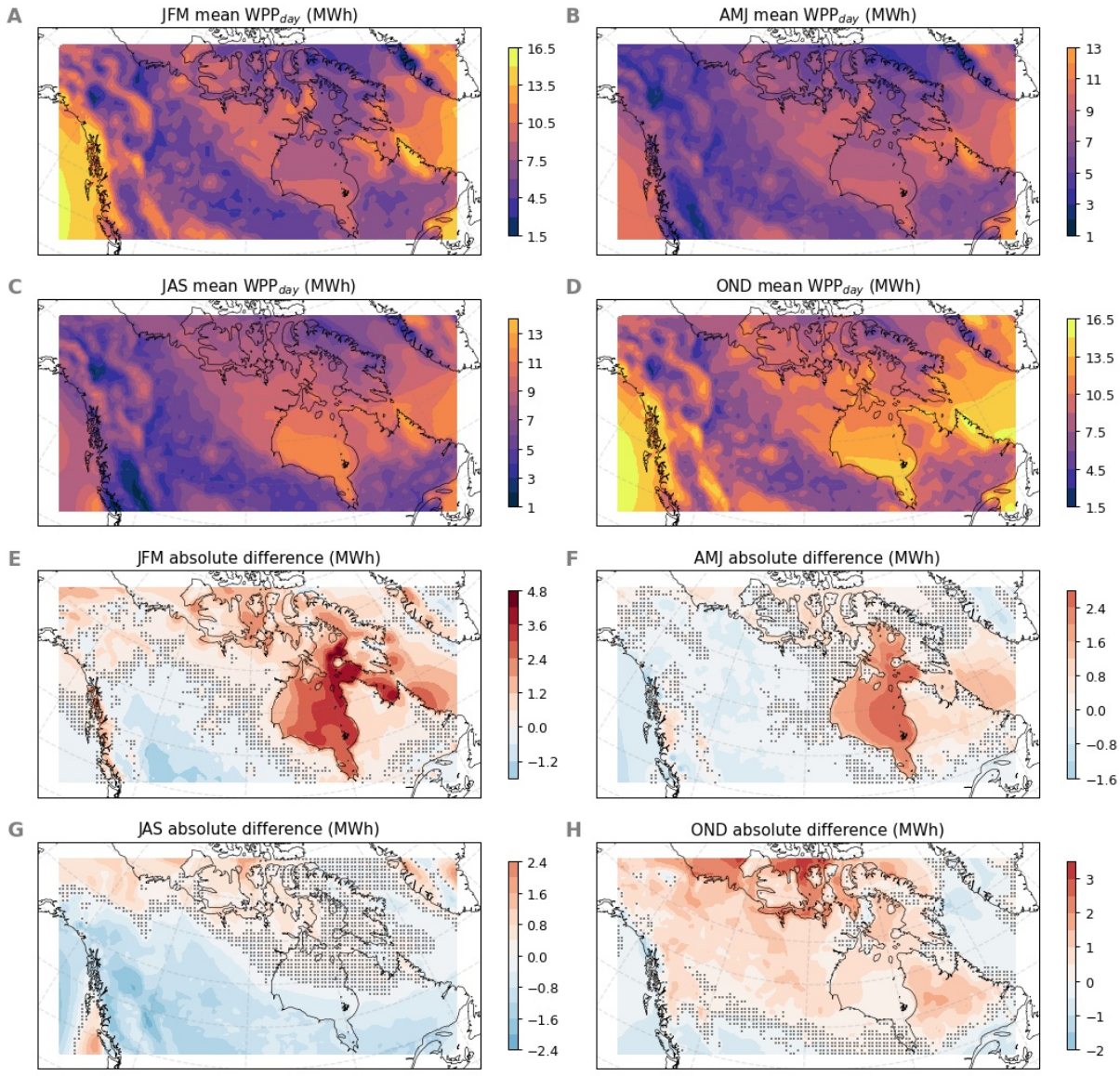

Figure 4.5: Mean WPP_{day} in the reference period (1970-1999; MWh, A to D) and ensemble mean change (MWh, E to H) by 2070-2099, by season. Individual plot colourbars display the range of values for that plot, scaled so that colours are comparable between plots for reference period power production (A to D) and mean change (E to H). Non-robust changes are masked with stippling. For plots of substantiality see Figure C.1 in Appendix C.

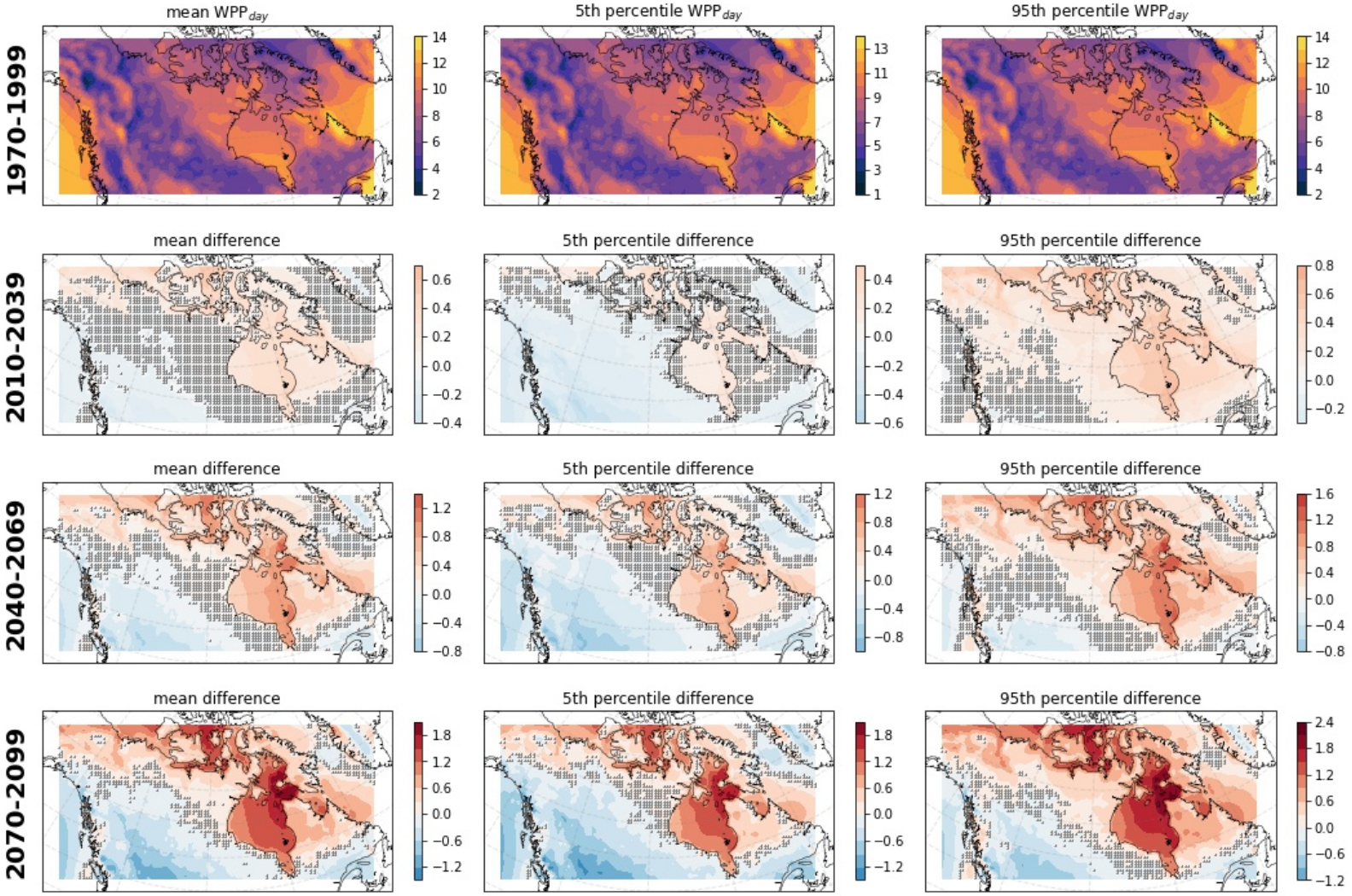

Figure 4.6: Ensemble mean (column 1), 5th percentile (column 2) and 95th percentile (column 3) daily wind power potential (WPP_{day}; MWh) in the reference period (1970-1999, row 1). Rows 2 to 4 show the absolute difference from the reference period (MWh) for the periods 2010-2039, 2040-2069, and 2070-2099. Individual plot colourbars display the range of values for that plot, scaled so that colours are comparable between plots of absolute value (row 1) and absolute difference (rows 2-4). Non-robust changes are masked with stippling.

39

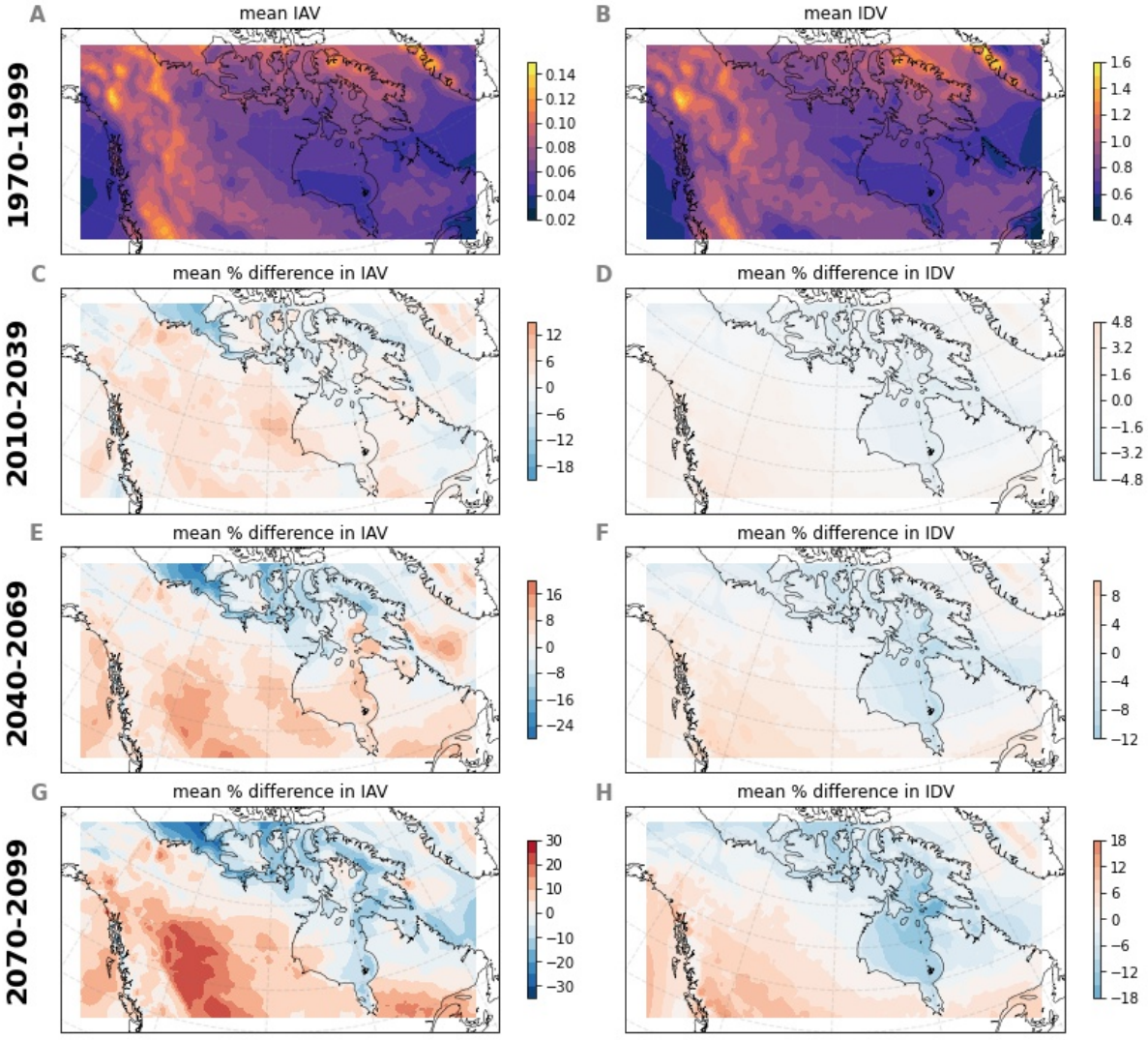

Figure 4.7: Daily wind power potential inter-annual variability (column 1) and inter-daily variability (column 2) for the reference period (1970-1999, row 1, dimensionless) and ensemble mean percent change for the periods 2010-2039, 2040-2069, and 2070-2099 (rows 2 to 4). Individual plot colourbars display the range of values for that plot, scaled so that colours are comparable between plots C to H. For plots of absolute change in IAV and IDV see Figure C.2.

4.1.3 Discussion

Trends in the CanRCM4 ensemble mean suggest that the recent wind speed stilling in mid-latitudes and positive trends at high latitudes revealed in observational (e.g., Tuller 2004; Vautard *et al.* 2010; Wan *et al.* 2010) and reanalysis (e.g., Deng *et al.* 2021) datasets until about 2010 will persist into the future. Previous ESM-based studies of projected wind speed or wind power vary widely in the magnitude, sign, and spatial pattern of change (e.g., Chen 2020). Studies generally agree on projected robust or significant increases in wind power in high latitude areas, although the extent of increases varies by study. Our results for *WPP* are consistent with the sign of wind speeds trends found by most other studies under extreme (RCP8.5 or SRES A2) climate change scenarios. Jeong & Sushama (2019) used an RCM driven by two ESMs, projecting increases for northern and eastern Canada by 2071-2100 in DJF and annually, but decreases across most of southern North America in JJA. Mioduszewski *et al.* (2018) also project decreases over most land areas of Canada, as well as increases for northern coastal areas and far northern interior regions using the CESM large ensemble simulations. Yao *et al.* (2012) also projected mean wind speed change of >5% for coastal areas off James and Hudson Bay by 2071-2100 compared to 1961-1990. However, different patterns of change were found by Jung & Schindler (2019) who found only limited increases projected by CMIP5 models, restricted to the high Arctic Archipelago and Hudson Bay, and small decreases in northern Quebec, in contrast to the present study. Further, using CMIP3 models, McInnes *et al.* (2011) found SWS increases in a northwest-southeast band across the Canadian continent where we project little or decreasing change; and no change or decreases in the high Arctic regions projected to have robust increases by the present study and others (Jeong & Sushama 2019; Mioduszewski *et al.* 2018).

Projections of multi-model ensemble (MME) wind power density change by Chen (2020) using NA-CORDEX models for the contiguous USA (excluding much of the study area) revealed changes of -20% to +20%, with decreases over the East Coast and western Canada, and increases over northern Ontario, Quebec, and Labrador, consistent in sign of change with the current study for the limited areas of overlap. Further, their projected increases in DJF WPD and decreases in JJA WPD for these northern regions of overlap are in agreement with our work. In contrast to our study, Karnauskas *et al.* (2018), using CMIP5 models, projected non-robust changes in wind power resources for most of Canada; increases were projected only for parts of the Canadian Arctic Archipelago. This result is similar to the findings of Gernaat *et al.* (2021) using an ISIMIP2b ensemble under RCP6.0[1], who found increases only in the same Arctic Archipelago regions, and non-significant decreases elsewhere, including northern continental areas (Gernaat *et al.* 2021). Qian & Zhang (2021) in a study of the Canadian Arctic Archipelago using CMIP6 models also only projected increases in the region

[1]RCP6.0 at 2100 has approximately the same radiative forcings as RCP8.5 in 2070 (Masui *et al.* 2011).

north of 72°N, and decreases to the south.

Our projections of high latitude increases in wind speeds and/or wind power potential are generally consistent with previous studies, although increasing trends are typically more spatially restricted than changes projected in the present study.[2] Over northern ocean areas, sea ice extent is closely tied with near-surface wind speeds (see following section). Due to the bias (underestimation) in sea ice coverage in CanESM2/CanRCM4 (see Section 2.5), it is likely that robust changes in the far north are apparent earlier and more broadly in CanRCM4 than other models. In the southern part of our study area, previous studies vary in sign of projected change, although many studies project decreases similar to our results. These differences demonstrate the challenges that remain in modelling of near surface wind speeds (see Section 2.5). Further, while large ensembles (as used in the present study) allow for better distinction of robust forced change from internal variability, only Mioduszewski *et al.* (2018) employed a single model large ensemble, predicting similar patterns to the present study. Other studies used smaller MME to assess significant change; Karnauskas *et al.* (2018), for example, uses a MME of 10 CMIP5 ESMs. While MMEs reduce model-related uncertainty, they may also reduce ensemble size, and therefore make detecting robust forced change from internal variability more challenging.

4.1.4 Analysis of potential causes

The divergence of projected wind and *WPP* changes between ESM-based studies makes assessment of potential causes of variability critical to understanding CanRCM4 projections. As discussed in Chapter 2, drivers of change in recent historical wind speed trends remain uncertain. Suggested causes of changing wind speed include changes in surface roughness (Vautard *et al.* 2010), boundary layer stability (Bichet *et al.* 2012; Mioduszewski *et al.* 2018), large scale circulation patterns (Torralba *et al.* 2017; Vautard *et al.* 2010), storm tracks (Yan *et al.* 2006), and ocean–atmosphere oscillations (Zeng *et al.* 2019). Changes in sea ice, storm activity, and atmospheric stability have been suggested as potential causes of near-surface wind speed (SWS) increases in the Arctic (Mioduszewski *et al.* 2018). To explore relationships between these factors, daily mean wind power potential was assessed against sea ice, atmospheric stability, roughness length, storminess, and air density. Air density was included in the analysis as it is directly related to wind power potential via Equation (3.15). For ocean areas only, roughness length was included in the analysis, as changes in model sea ice cover will result in sizable changes to surface roughness. The impact of roughness length

[2]Most studies of *WPP* change use wind speed means on longer timescales (e.g., monthly) in their calculation of wind resource estimates and change. Karnauskas *et al.* (2018) assessed the impact of using monthly versus daily mean wind speeds on wind resource estimates, finding that longer temporal averaging results in underestimation of wind power potential. However, temporal correlation between monthly versus daily estimates was high, and therefore relative change would be minimally affected (Karnauskas *et al.* 2018).

over land areas was not assessed as land use change is not included in CanRCM4 and other potential contributors to variations in roughness length are minimal. Assessment of large scale circulation patterns or ocean-atmosphere oscillations is outside the scope of this study.

Deseasonalized, linearly detrended monthly statistics for the period of 1970-1999 were used in the following analysis. Correlations were computed point-wise (by grid cell) across all ensemble members in the reference period. Table 4.2 presents the factors considered, the monthly statistic used in calculations of correlation and change, and the abbreviated name used in following discussion.

Table 4.2: Monthly variables considered in a correlation analysis with monthly mean daily power production. Variables 2 through 4 are used as a set of 'all' controlling factors over land and variables 2 to 6 are used as a set of 'all' controlling factors over ocean. Near-surface wind speed (7) in only used in some instances, as specified. All variables were detrended with linear detrending and monthly means removed before calculating correlation or partial correlation.

	Variable	Abbreviation	Monthly statistic
1	Daily power production	WPP_{day}	Mean
2	Atmospheric stability	z/L	Median
3	Storminess	S	Mean
4	Air density	ρ	Mean
5	Sea ice[a]	SIC	Mean
6	Roughness length[a]	z_0	Median
7	Near-surface wind speed[b]	SWS	Median

[a]For ocean areas only. [b]Only used in some instances, as specified.

Sea ice, surface layer stability, and roughness length

AMJ is used for sea ice partial correlation analysis in the following section, as it is a season of transitional ice cover across most of the study area during the reference period.

CanESM2/CanRCM4 exhibits a strong low bias in sea ice (e.g., Kushner *et al.* 2018; Stroeve *et al.* 2012), particularly in summertime, with modelled sea ice extent less than half of that observed (see Section 2.5). Over the 21st century, the CanRCM4 ensemble mean predicts strong decreases in sea ice concentration (SIC) in the study area (Figure 4.8, panel B), with decreases of almost 100% in almost all areas in JAS and OND (low sea ice seasons), and for Hudson Bay, the Hudson Strait, and the Labrador Sea in AMJ and JFM (high sea ice seasons; Figure 4.9). SIC is weakly negatively correlated with WPP_{day} (domain

average AMJ $\rho_{WPP,SIC}$ = -0.21). Sea ice loss has been linked to increased turbulent heat flux and decreased static stability, as measured by z/L (e.g., Deser *et al.* 2010; Overland 1985; Overland & Wang 2010). Increased heat flux over the ice-free ocean leads to decreases in static stability, resulting in enhanced turbulent transport of momentum downward into the planetary boundary layer from the free atmosphere (Knippertz *et al.* 2000). However, correlation analysis between z/L and SIC indicates little relationship between sea ice and surface layer stability (e.g., ocean average AMJ $\rho_{SIC,z/L}$ = -0.02; see Figure C.3), and the weak negative correlation between WPP_{day} and SIC was little affected by controlling for surface layer stability (AMJ $\rho_{WPP,SIC}$ = -0.21, $\rho_{WPP,SIC \cdot z/L}$ = -0.22; Figure 4.11). Despite the weak correlation, a change in median surface layer stability is clear in projections over both land and oceans (Figure 4.8).

On average, z/L increases strongly across the 21st century over northern marine areas in the Canadian Arctic Archipelago, increases moderately in the Labrador Sea, and decreases in southern Hudson Bay and the Pacific Ocean (Figure 4.8, panel F). Over land areas trends are weaker, as median stability is closer to neutral, with average z/L slightly increasing over southern regions, and decreasing over northern land areas close to the Arctic Ocean and Hudson Bay. However, there is a strong seasonal cycle in these trends, and the annual average is largely the result of AMJ and JAS changes in northern marine areas, offset by oppositely-signed trends in OND and JFM. These changes are consistent with established relationships between sea ice loss and atmospheric stability (e.g., Overland & Wang 2010, see Figure C.4). Warm-season increases in z/L over ocean areas are likely due to enhanced warming over the continent, which, after advection of airmasses over the cooler ocean results in a stable near-surface layer. Likewise, during OND and JFM, loss of sea ice results in increased upward heat flux from the relatively warm ocean and more unstable conditions. In all seasons except JFM these trends tend to bring the atmospheric stratification away from neutrality over ocean areas: unstable seasons become on average more unstable, and stable seasons become on average more stable (Figure 4.8, or Figure C.4 for change by season). This is also true for southern continental regions in most seasons. The general trend away from neutrality is the opposite of that expected given the increasing wind speeds, as high wind speeds are associated with near-neutral conditions (e.g., Arya 2001; Baas *et al.* 2016). This suggests that increasing SWS and *WPP* are not causally linked to changes in atmospheric stability.

The median stability (or instability) also appears to be important to the sign of partial correlations between *WPP* and z/L. In stable seasons/locations, correlations are negative, while in unstable seasons, correlations are positive. Over the whole year, *WPP* and z/L over continental regions (generally stable) are weakly negatively correlated ($\rho_{WPP,z/L \cdot allland}$ = -0.25) and over ocean areas (generally unstable) weakly positively correlated ($\rho_{WPP,z/L \cdot allocean}$

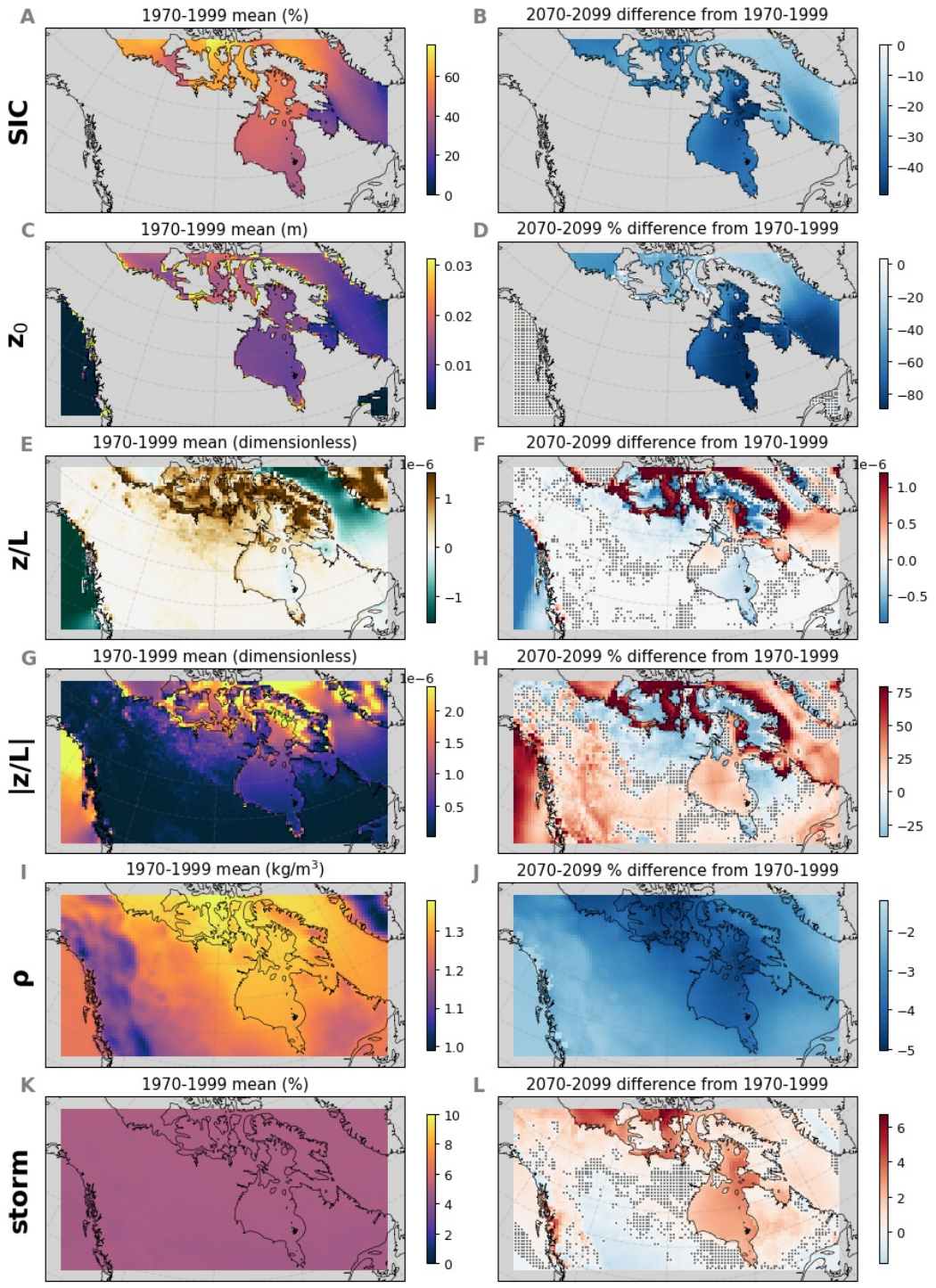

Figure 4.8: Ensemble mean in the reference period (column 1) and projected change (either absolute or percent, as indicated) by 2070-2099 (column 2) for the monthly statistics (see Table 4.2) of: (A,B) sea ice concentration (SIC); (C,D) roughness length (z_0); (E,F) surface layer stability (z/L); (G,H) absolute surface layer stability ($|z/L|$); (I,J) air density (ρ); and (K,L) storminess (percentage of time classified as storm; see Section 3.6). By construction, storminess in the reference period is almost uniform in 5% occurrence, as storm thresholds are defined based on the 95th percentile reference period winds. Non-robust changes in column 2 are masked with stippling. Grey areas over water in panel B indicates reference period sea ice concentration of less than 1%.

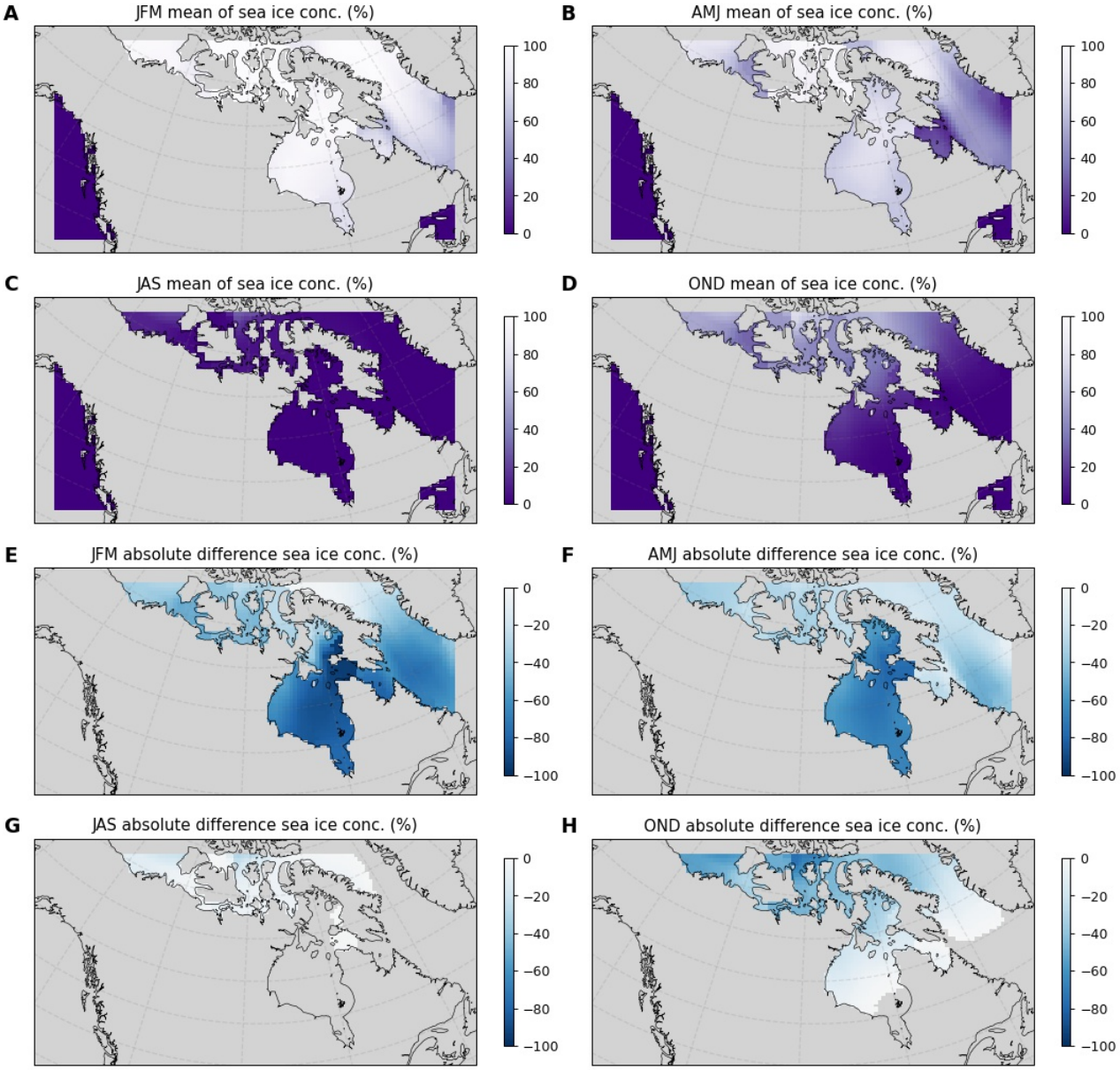

Figure 4.9: Ensemble mean sea ice concentration in the reference period (1970-1999, %, A-D) and mean absolute change by 2070-2099 (E-H), by season. Grey areas over water in panels E to H indicate reference period sea ice concentration of less than 1%. Non-robust changes are masked with stippling.

= 0.17, see Figure 4.10). These changing correlations are not consistent with the expected negative relationship between surface stability and wind speed, in which greater static instability results in enhanced turbulent transport of momentum downward and increased wind speeds (e.g., Barthelmie 1999). However, highest wind speeds are associated with near-neutral atmospheric conditions (Arya 2001; Baas *et al.* 2016; Barthelmie 1999). By taking the partial correlation of the absolute value of z/L with *WPP* controlling for all variables this result is confirmed: in all seasons, absolute stability is weakly negatively correlated with *WPP*, indicating that *WPP* is positively associated with more neutral conditions (Figure 4.10). Overall, results do not indicate that decreased static stability over increasingly ice-free ocean areas is positively related to increases in *WPP*, as suggested by some previous studies (e.g., Knippertz *et al.* 2000; Mioduszewski *et al.* 2018).[3]

Previous studies (e.g., Knippertz *et al.* 2000; Mioduszewski *et al.* 2018) also link increases in surface winds to a presumed decrease in surface roughness resulting from sea ice loss. Lower SIC decrease the surface roughness, and result in faster near-surface wind speeds and higher *WPP*. Indeed, monthly median roughness length (z_0) over ocean areas decreased strongly, with changes exceeding 80% in Hudson Bay, coinciding with a decline in mean sea ice coverage to nearly zero in these areas. No robust change occurs over ocean areas without sea ice in the reference period (Figure 4.8, panel D). Partial correlation of *WPP* and SIC controlling for both z/L and z_0 reduces the AMJ correlation $\rho_{WPP,SIC \cdot z/L,z_0}$ to -0.07 (Figure 4.11), indicating that roughness length is the most important contributor to increases in *WPP* resulting from sea ice loss in our study area.

Storminess

Climate change and its impact on meridional temperature gradients has been linked to northward shifts in storm tracks in the Northern Hemisphere (Shaw *et al.* 2016). This shift is the combined result of multiple opposing influences on storm activity. For example, amplified warming of the upper troposphere in the tropics and lower troposphere in the polar regions results in opposing effects on the meridional temperature gradients. Arctic amplification of surface temperatures reduces the surface temperature gradient, shifting storm tracks equatorward, while amplified upper troposphere warming in the tropics increases the temperature gradient, shifting storm tracks poleward (Harvey *et al.* 2014). Reduced sea ice cover has also been linked to increased atmospheric instability, baroclinicity, and therefore increased cyclogenesis (Jaiser *et al.* 2012).

[3]Knippertz *et al.* (2000) argue that this decreased stability may be particularly important over Hudson Bay, but that roughness length changes may be important over other open ocean areas (e.g. the Greenland Sea). According to Knippertz *et al.* (2000), roughness length decreases cannot explain wind speed increases over Hudson Bay, as roughness lengths in the assessed model are only reduced when sea ice cover reaches zero, a situation which rarely occurs in Hudson Bay in their study.

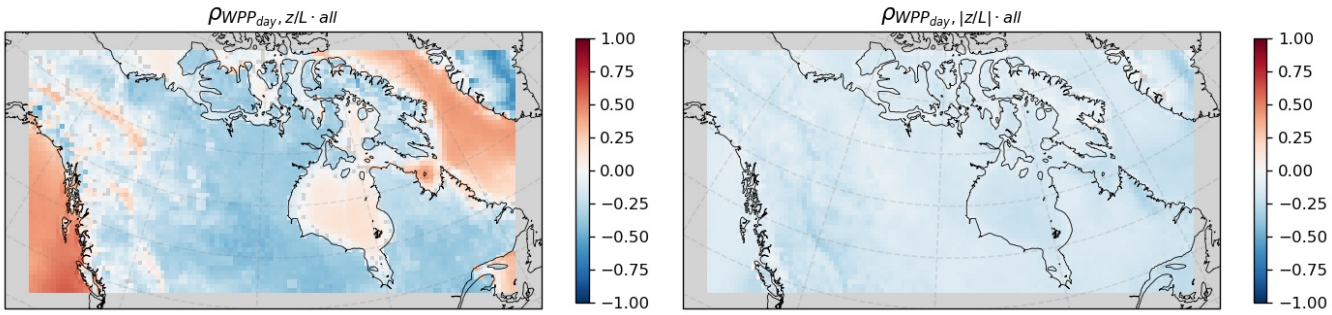

Figure 4.10: Partial correlations between detrended, deseasonalized WPP_{day} and surface layer stability in the reference period (1970-1999, all seasons) controlling for all other land or water factors as appropriate (panel 1); and the same correlations but between WPP_{day} and absolute surface layer stability (panel 2). Non-significant (p>0.05) correlations are masked out with grey.

We define storminess as the percentage of time in which SWS exceeds the 95th percentile SWS of 1970-1999 for at least 6 hours (see Section 3.6). Our study indicates that monthly mean storminess is fairly highly correlated with mean WPP_{day} in all seasons (domain mean annual $\rho_{WPP,S \cdot land} = 0.59$, $\rho_{WPP,S \cdot ocean} = 0.37$, see Figure 4.12). Across the domain, changes in storminess over the 21st century generally follow the spatial patterns projected for *WPP* change, with ensemble mean changes of greater than 100% projected in some northern marine areas, and decreases over southern Canada (see Figure 4.8 panel L; and also Figure C.5 for seasonal patterns). Correlations over ocean areas were smaller than over landmasses, likely due the fact that the mean wind speed is already closer to the turbine rated wind speed over oceans, limiting potential power production gains under high-wind conditions. Correlation of wind power density (Equation (3.13), which does not consider cut-in or cut-out wind speeds) with storminess confirms this, revealing an almost one-to-one correlation across the entire study area controlling for all factors (not shown). Further, extreme wind speeds over ocean areas may already be close to the turbine cut-out wind speed, so that increasing storminess may result in increased down-time (zero power output). Indeed, controlling for the median wind speed causes a reversal of correlations in areas with high baseline wind speed (where storm conditions could result in high-wind turbine cut-out), resulting in weak negative correlation between *WPP* and storminess over most southern (more ice-free, higher median SWS) marine areas (Figure 4.12).

The correlation between mean *WPP* and storminess is not surprising. Increases in extreme wind speeds could be due to either a rightward shift in the entire distribution of wind speeds, or a change in its skewness (a longer tail in the distribution, potentially due to changes in cyclone activity), or both. While our assessment does confirm a positive correlation between extreme wind speeds and increased power production over most land areas and the Canadian

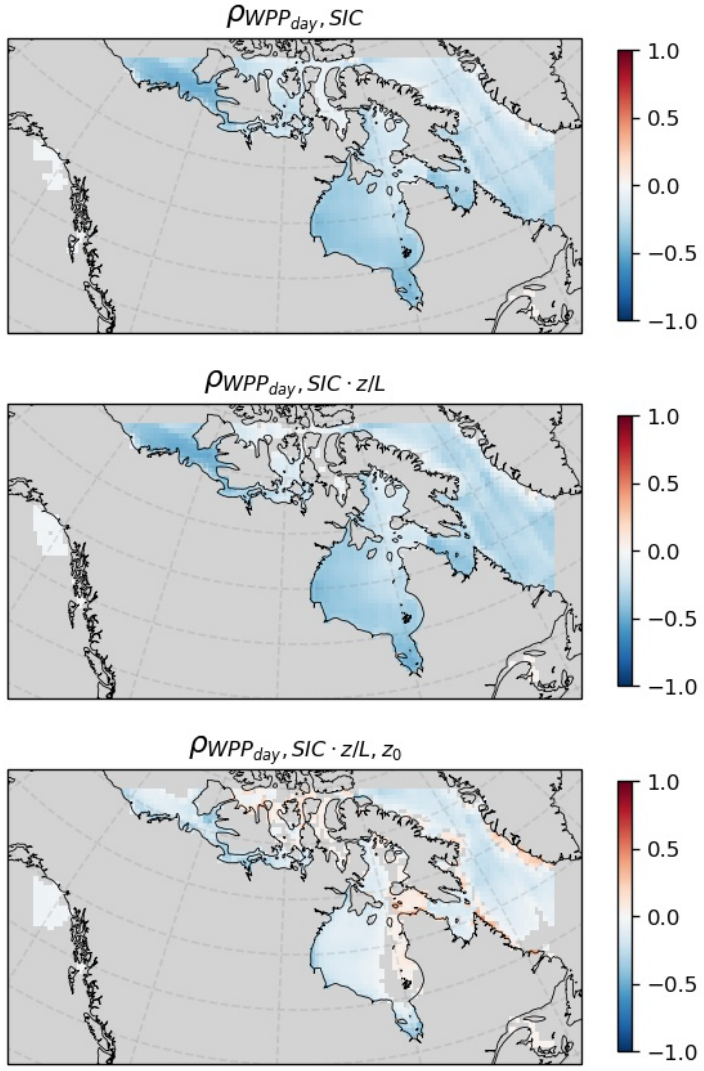

Figure 4.11: Partial correlations between detrended, deseasonalized WPP_{day} and sea ice concentration in AMJ in the reference period (1970-1999) controlling for no factors (row 1), surface stability (z/L, row 2), and z/L and roughness length (z_0; row 3). Domain average $\rho_{WPP,SIC}$= -0.21, $\rho_{WPP,SIC \cdot z/L}$ = -0.22, and $\rho_{WPP,SIC \cdot z/L,z_0}$ = -0.07. Non-significant (p>0.05) correlations are masked out with grey.

Arctic Archipelago, the reasons behind increased storminess (e.g., a shift in wind speed distribution or increased frequency of cyclonic storms) remains uncertain. Assessment of changes in synoptic activity through other methods is outside the scope of this study, but future research could consider measures using mean sea level pressure or lower-tropospheric vorticity to better understand contributions of changes in storm tracks or cyclone counts.

Air density

Air density was included in the analysis as it is directly related to wind power potential via Equation (3.15). It is also closely linked with air temperature through the Ideal Gas Law (Equation (3.6)): all other parameters remaining stationary, as temperature increases we expect density to decrease. As Arctic amplification of global warming has large impacts on northern temperatures, robust decreases in air density of up to 5% are projected (Figure 4.8, panel J), most markedly over ocean areas in cold seasons (JFM and OND), likely related to declining sea ice[4]. Due to the direct proportionality of WPP with ρ, we expect positive correlations, however, calculated $\rho_{WPP,\rho}$ is negative even controlling for all factors (domain mean annual $\rho_{WPP,\rho}$ = -0.24, $\rho_{WPP,\rho \cdot all}$ = -0.18, Figure 4.13). This suggests the existence of a strong positive relationship between temperature and SWS, which offsets the negative correlation between temperature (as a proxy for density) and WPP described via Equation (3.15). The reasons behind this correlation are unclear.

4.1.5 Conclusions

Overall, WPP is projected to increase by up to 30% across the northernmost part of the study area, including all Canadian Arctic marine areas and adjacent continental regions, with changes most pronounced in cold seasons. However, southern portions of the study area and the Pacific Ocean are projected to see moderate decreases in WPP. Both inter-annual and inter-daily variability of WPP decrease for the communities of focus. Over the whole domain, decreases in inter-daily variability are associated with regions of annual mean WPP increase, and increases with mean WPP decrease. This is due to changes that tend

[4]Indeed, air density and sea ice are positively correlated, see Figure C.3.

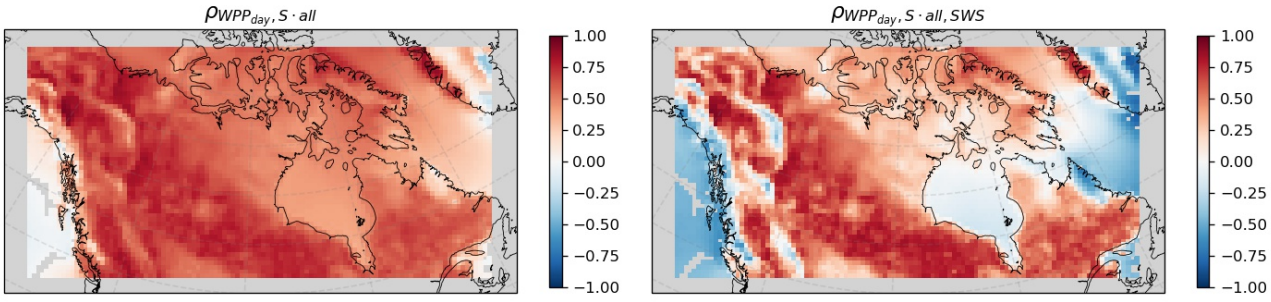

Figure 4.12: Partial correlations between detrended, deseasonalized WPP_{day} and storminess in the reference period (1970-1999, all seasons) controlling for all other land or water factors as appropriate (panel 1); and all other land or water factors as well as median near-surface wind speed (panel 2). Non-significant (p>0.05) correlations are masked out with grey.

to dampen or heighten the seasonal cycle of *WPP*.

Over the northern ocean regions, increases in *WPP* are weakly correlated with sea ice loss and associated reduced roughness lengths, while the influence of decreased atmospheric stability from cool-season sea ice loss is not apparent. Due to the bias (underestimation) in sea ice coverage in CanESM2/CanRCM4, it is likely that robust, substantial changes in the far north are apparent earlier in CanRCM4 than other models. Increases (decreases) in storminess as defined in this study play a role in northern-coastal (southern-interior) changes; however, differences in synoptic storm activity are difficult to distinguish from shifts in wind speed distribution using the methods in this work. Changes in large scale circulation patterns and ocean-atmosphere oscillations have been suggested as an important contributor to SWS variability in other works (e.g., St. George & Wolfe 2009; Torralba *et al.* 2017; Vautard *et al.* 2010; Zeng *et al.* 2019). While not directly assessed in this study, these factors are implicitly present in variations in storminess and sea ice, and could be an avenue of further study.

4.2 Solar power potential

This section will first consider solar power potential (*SPP*) variability and change for the communities of focus and then for the entire domain. Potential causes of change will then be assessed.

4.2.1 Communities of focus

Solar power potential in Canada is largely determined by latitude, due its influence on total downwelling solar radiation over the course of the year. The communities of focus are located in northern regions, and therefore have comparatively low *SPP* when considering

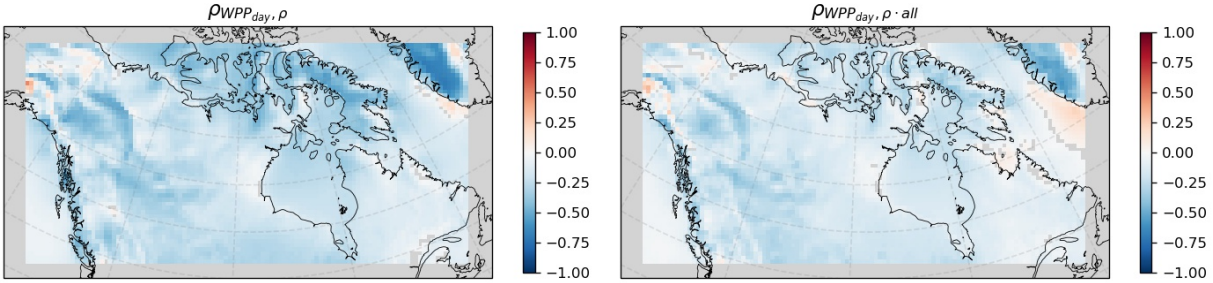

Figure 4.13: Correlation between detrended, deseasonalized WPP_{day} and air density in the reference period (1970-1999, all seasons), controlling for no factors (panel 1) or controlling for all other land or water factors as appropriate (panel 2). Non-significant (p>0.05) correlations are masked out with grey.

the domain average. Sachs Harbour, the most northerly community, has the lowest reference period annual solar power potential (SPP_{annual}) at 663 MWh, while Sanikiluaq, the most southerly community, has the highest SPP_{annual} at 881 MWh (Table 4.3 and Figure 4.14). Given the same installation capacity, the annual power potential of solar power is about 4 to 5 times lower than that of wind power for the communities of focus (see Table 4.1 for WPP_{annual}). However, *SPP* has not been optimized in this work due to the assumption of horizontal panel orientation, instead of more efficient tilted orientations (see Section 3.4). Further, this study does not take into account economic considerations of installation.

Seasonally, *SPP* has a predictable annual cycle across all communities. Mean SPP_{day} is greatest in AMJ, followed by JAS, and is lowest in OND. This strong seasonality differs from wind power potential, which exhibits slightly different annual cycles depending on location. All communities are projected to experience a decrease in mean SPP_{annual} across the 21st century (Table 4.3 and Figure 4.14), although, as for wind power, the magnitude and seasonality of the change vary by location (Figure 4.15). Annual mean decreases of $\sim$16% are projected by the end of the 21st century in Sanikiluaq and Iqaluit. The smallest change is projected for Rankin Inlet (annual mean decrease of $\sim$6%, see Table 4.3). Projected change by season, presented in Figure 4.15, indicates that annual SPP_{day} trends are chiefly driven by large AMJ decreases in potential energy production. However, by mid-century AMJ, JFM and OND all see robust and substantial decreases in SPP_{day} for all communities. JAS trends emerge later and vary in sign by location (see Figure 4.15), with more northerly locations projected to see decreases and more southerly communities projected to see increases. Time of emergence for robust changes in SPP_{annual} occurs by 2000-2029 for most communities in JFM, AMJ, and OND (Figure 4.15). In all seasons except JAS, substantial changes emerge by 2050-2079. The strength of the forced change for *SPP* is much stronger than that of *WPP*, for which robust changes emerge slightly later and less broadly, and substantial changes not at all for many communities.

Figure 4.16 presents the ensemble mean trend in SPP_{day} across the 21st century for Rankin Inlet, also showing the standard deviation and 5th and 95th percentiles. Both inter-annual variability (IAV) and intra-daily variability (IDV, measured using coefficients of variation, see Section 3.8 for definitions) increase over the course of the century for all communities (Table C.2). This result contrasts with changes to variability of *WPP*, for which decreases in both IDV and IAV are projected (see Section 4.1 and Table C.1).

4.2.2 Northern Canada study area results and discussion

Over the whole domain, annual mean SPP_{day} is largely determined by latitude through its influence on annual top of atmosphere solar irradiance (Figure 4.17, panel A). However, some

Table 4.3: Ensemble mean SPP_{annual} for the communities of focus in the reference period (1970-1999), and change by the end of the 21st century (2070-2099; columns 2 to 4, rounded to the nearest whole number for clarity). The robustness (column 5, dimensionless) and substantiality (column 6, dimensionless) of the change are presented. Note that all changes are robust and substantial (>1, boldface; see Section 3.5).

	SPP_{ann} (MWh) 1970-99	ΔSPP_{ann} (MWh) 2070-99	$\%\Delta SPP_{ann}$ 2070-99	Robustness of change	Substantiality of change
Arviat	803	-58	-7	**12.08**	**2.26**
Baker Lake	795	-68	-9	**15.06**	**2.55**
Iqaluit	773	-122	-16	**25.23**	**4.31**
Iqaluit CL	797	-107	-13	**18.61**	**3.48**
Rankin Inlet	829	-51	-6	**10.45**	**1.94**
Sachs Harbour	663	-89	-13	**14.82**	**2.52**
Sanikiluaq	881	-143	-16	**18.96**	**4.24**
Umiujaq	789	-98	-12	**14.72**	**3.01**

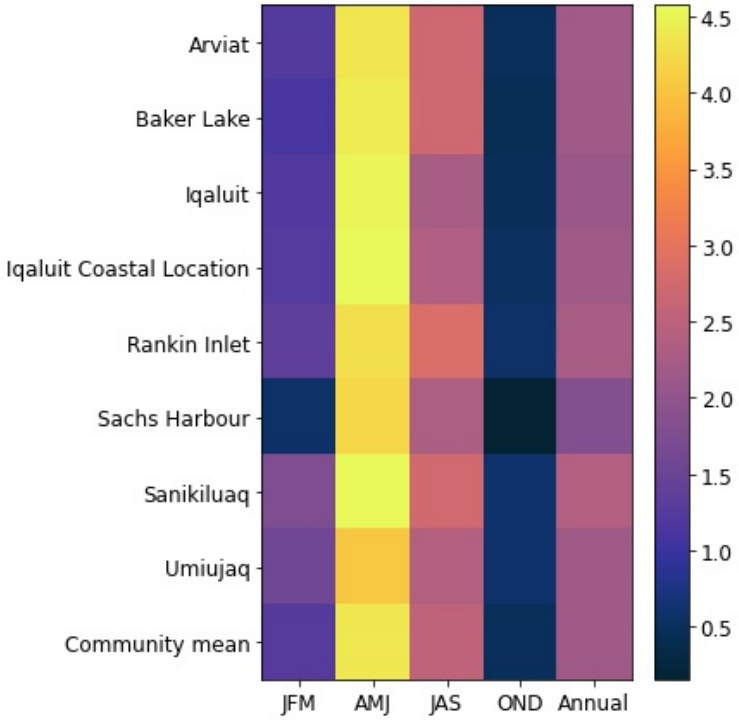

Figure 4.14: Ensemble mean SPP_{day} (MWh) by season and community in the reference period (1970-1999).

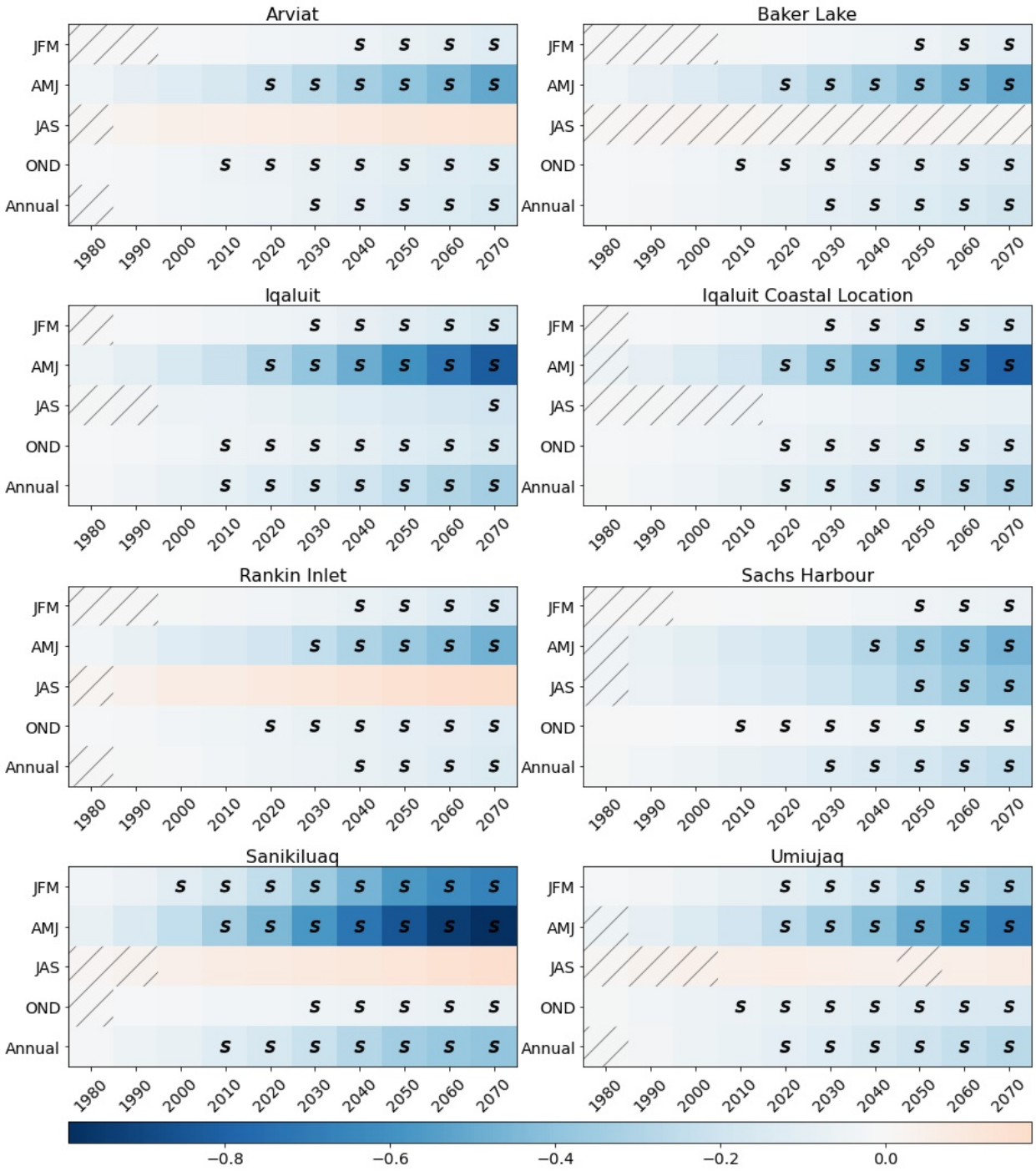

Figure 4.15: Absolute difference in mean daily solar power production (MWh) from the 1970-1999 reference period by season. Mean SPP_{day} was computed in a 30-year rolling window by decade. Axis labels indicate the starting year of the period, e.g., 2070 corresponds to 2070-2099. Non-robust changes are masked with hatching. Substantial changes are indicated with a boldface "S". Each panel represents values from the model grid cell closest to the stated community.

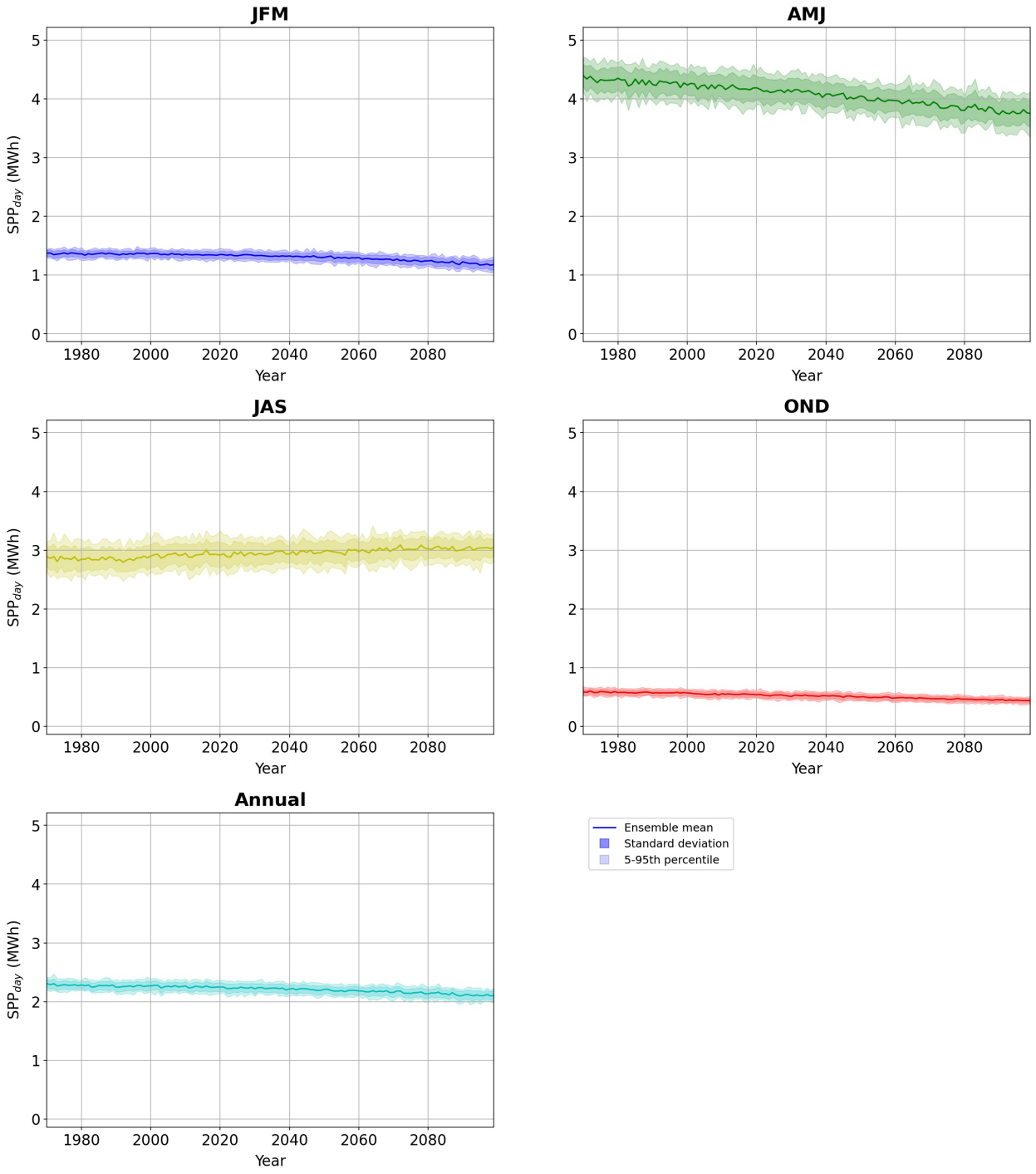

Figure 4.16: Daily solar power production (MWh) projections for Rankin Inlet by season and annually from 1970 to 2100, showing the ensemble mean (dark line), standard deviation (dark shading), and 5th to 95th percentiles (light shading). Plots for other communities of focus can be found in Appendix D.

regional hot spots stand out from this large-scale trend. CanRCM4 grid cells classified as glacier ice are identifiable by their locally high SPP_{day}, including locations in southwestern British Columbia, northern Baffin Island, Greenland, and the northern West Coast. These anomalies may be due to the multiple reflections of shortwave radiation up from the ice surface and then back down from the underside of clouds, when present. The Canadian prairies are another region of relatively high *SPP*, likely related to low cloud cover in combination with its southern location. Across the study area, mean *SPP* varies with the solar seasons (Figure 4.18). Domain average SPP_{day} in the reference period is greatest in AMJ (4.2 MWh), followed by JAS (2.8 MWh), and lowest in OND (0.6 MWh). The high *SPP* in AMJ compared to JAS is due to greater downwelling radiation, likely related to larger JAS values of cloud cover and atmospheric water (Figure C.10 and Figure C.11). In addition, over snow and ice-covered areas with low-level clouds (the Arctic is quite cloudy; Serreze & Barry 2014), multiple surface-cloud reflections can increase surface DSR considerably relative to snow and ice-free conditions (Wendler *et al.* 1981).

A robust decrease in 30-year annual mean SPP_{day} is projected over the entire study area by as early as 2010-2039, with the exception of the southern parts of ocean regions (Figure 4.17). Large decreases are projected for British Columbia and northern regions, while the southern continental interior sees more moderate decreases. Arctic regions which currently experience seasonal ice coverage, as well as adjacent continental areas, are projected to see the most considerable decreases in SPP_{day}, up to 30% over some ocean areas of Hudson Bay and the Foxe Basin. This region of large projected decrease covers most of Nunavut, Northern Quebec (including Nunavik), the Quebec-Labrador Peninsula, and the northern portions of NWT and the Yukon. Our measure of substantiality is more conservative than robustness; but substantial changes of mean SPP_{day} emerge for the entire domain by the end of the 21st century, excepting southern parts of ocean areas (Figure 4.17). In addition, looking at the ensemble 5th and 95 percentiles of absolute difference in SPP_{day} (Figure 4.19), most changes are robust even at the 5th percentile as early as 2010-2039.

Trends in SPP_{day} across the 21st century vary by season in both the sign and magnitude of change (Figure 4.18). Robust decreases are generally projected in all seasons for northern regions, excluding Hudson Bay in JAS, with greatest change in AMJ (domain average -0.5 MWh by 2070-2099), followed by JFM (-0.2 MWh). JAS is the only season for which increases in SPP_{day} are projected, and sees a strong latitudinal control: southern regions are projected to increase and northern regions to decrease. The absolute change in OND is small, due to low baseline *SPP*, but the percentage change is high (see Figure C.7 for maps of percentage change). The greatest percentage change is seen in JFM (particularly over northern ocean areas) and OND (particularly over northern continental areas). By 2070-2099, changes are substantial over almost the entire study area in all seasons except JAS

(see Figure C.7).

Inter-annual (IAV) and inter-daily variability (IDV) of solar power potential are projected to increase across the 21st century for most of the study area (Figure 4.20), with increases in IAV up to 100%. These extreme IAV increases are not monotonic in time and are highly localized, particularly in northern ocean areas. The Foxe Basin (just north of Hudson Bay) sees larger IAV in 2040-2069 than in 2070-2099, suggesting that variability in sea ice is strongly linked to variability in *SPP*. The mid-century is a period of high projected ice variability (and *SPP* variability) in the Foxe Basin, before it largely disappears in this region by the end of century, coinciding with IAV decreases (not shown). In contrast, the small straits in the western Arctic Archipelago lose sea ice later, and therefore experience higher variability at the end of the century. For inter-daily variability, increases are largely monotonic and are more spatially uniform, although still greatest over northern ocean areas. Changes in the magnitude of seasonal differences are unlikely to be a large contributor to *SPP* IDV change. *SPP* IDV is projected to increase even in regions where all seasons see a decrease in mean *SPP* (i.e., the most northerly part of the study area). Therefore, potential amplification of the seasonal cycle alone cannot explain IDV increases. These results imply that across the domain, and particularly in Arctic and adjacent coastal regions, *SPP* is projected to become less stable, especially during periods of sea ice transition.

The results of this study largely agree with other projections of change in solar power potential or solar irradiance under extreme (RCP8.5 or SRES A2) climate change scenarios. Most studies project decreases over the study area for DSR (e.g., Huber *et al.* 2016; Remund & Müller 2010; Wild *et al.* 2015a) or PV potential (e.g., Crook *et al.* 2011; Wild *et al.* 2015a; Zou *et al.* 2019). However, some studies project minimal change (Haywood *et al.* 2011) or small increases in southern Canada (using ISIMIP2b models under RCP6.0, Gernaat *et al.* 2021). Projections using CMIP5 and CMIP3 models agree with our results of strong decreases in PV potential at northern high latitudes, and larger decreases in these regions than at lower latitudes (Crook *et al.* 2011; Gernaat *et al.* 2021; Wild *et al.* 2015a; Zou *et al.* 2019).

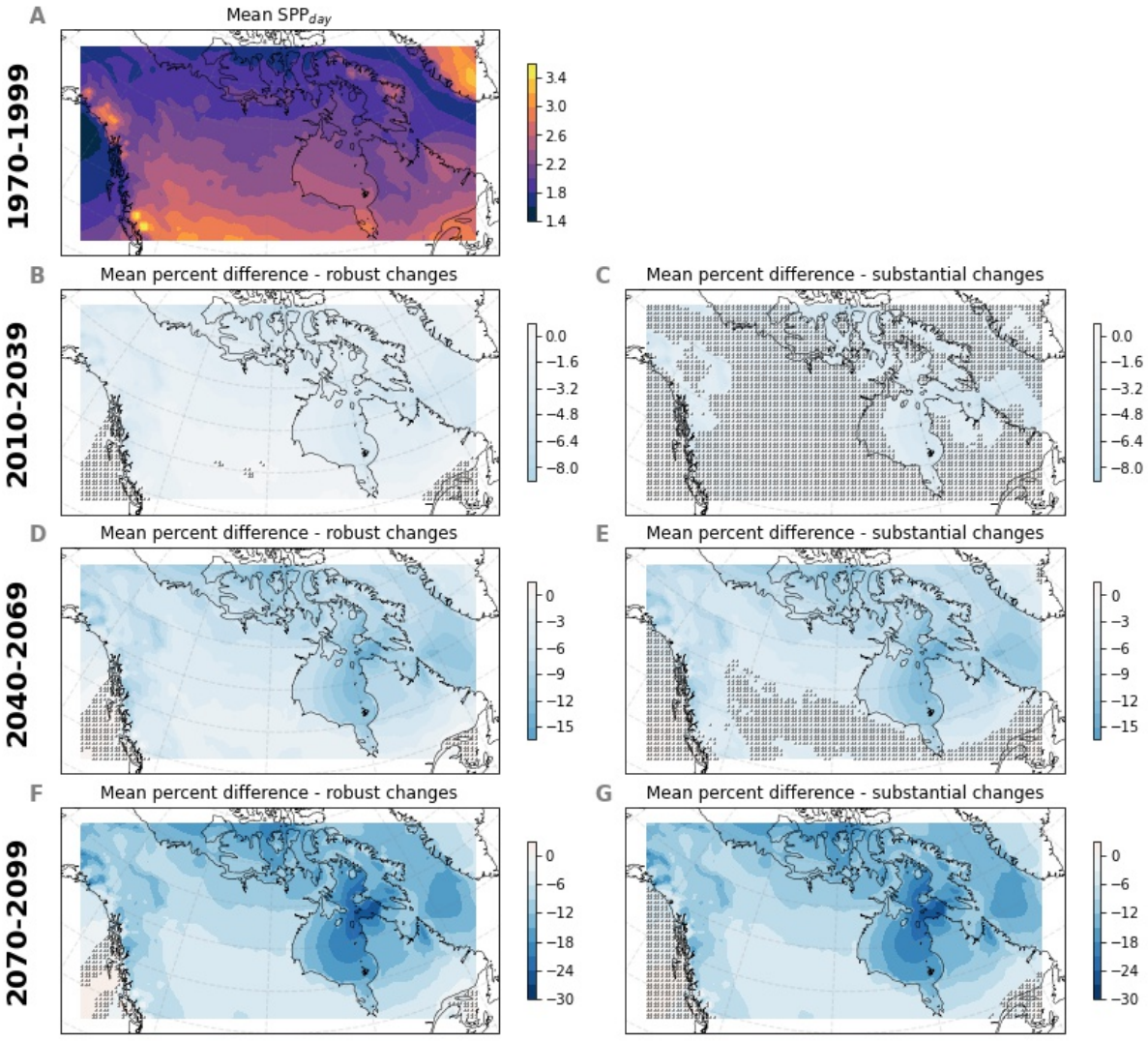

Figure 4.17: Ensemble mean reference period (1970-1999) SPP_{day} (MWh, panel A) and percent difference from the reference period for the periods 2010-2039 (B and C), 2040-2069 (D and E), and 2070-2099 (F and G). Individual plot colourbars display the range of values for that plot, scaled so that colours are comparable between plots of percent difference. Non-robust (B, D and F) and non-substantial (C, E and G) changes are masked with stippling.

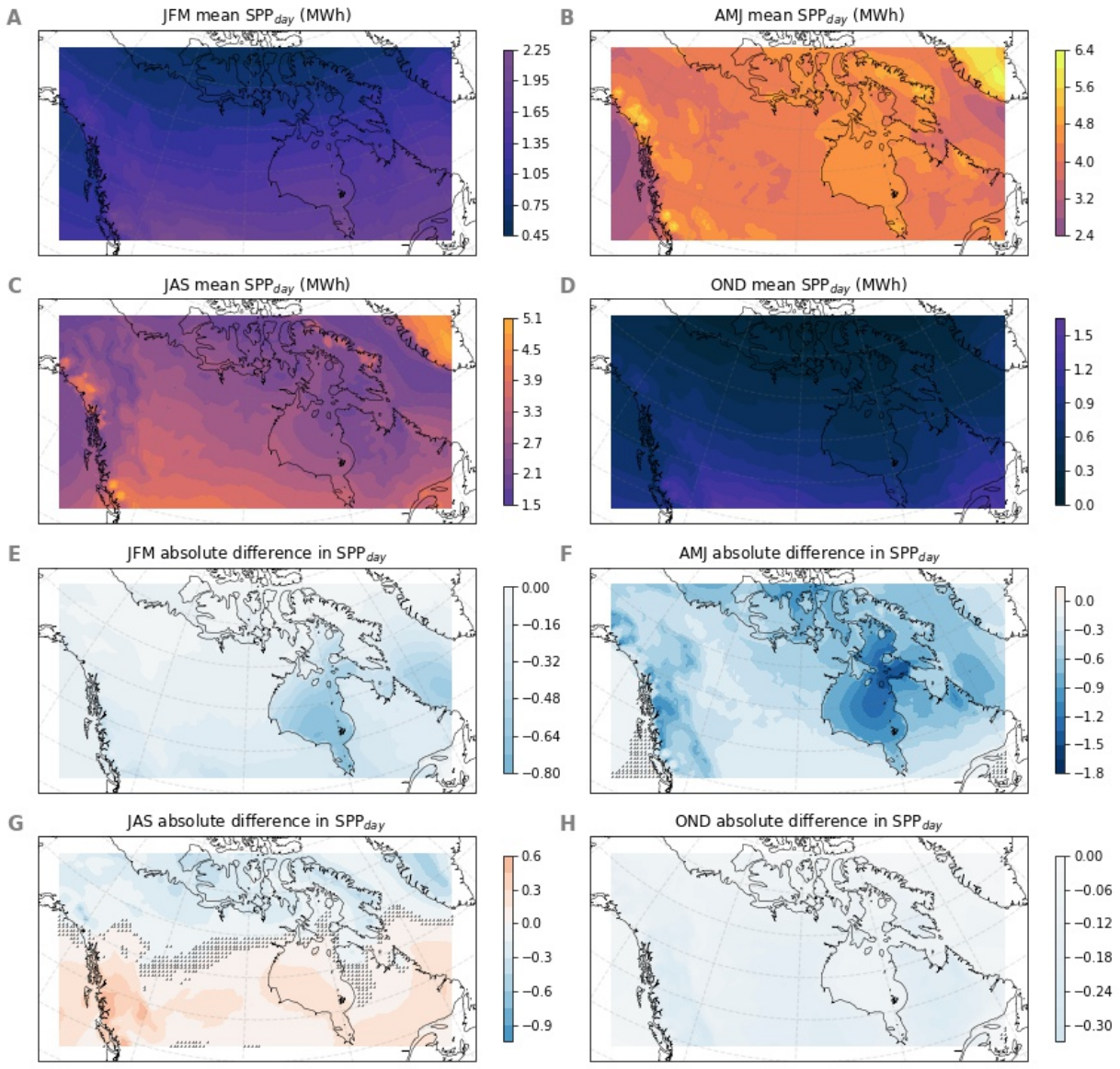

Figure 4.18: Mean SPP_{day} in the reference period (1970-1999; MWh, A to D) and ensemble mean change (MWh, E to H) by 2070-2099, by season. Individual plot colourbars display the range of values for that plot, scaled so that colours are comparable between plots for reference period power production (A to D) and mean change (E to H). Non-robust changes are masked with stippling. For plots of substantiality see Figure C.6 in Appendix C.

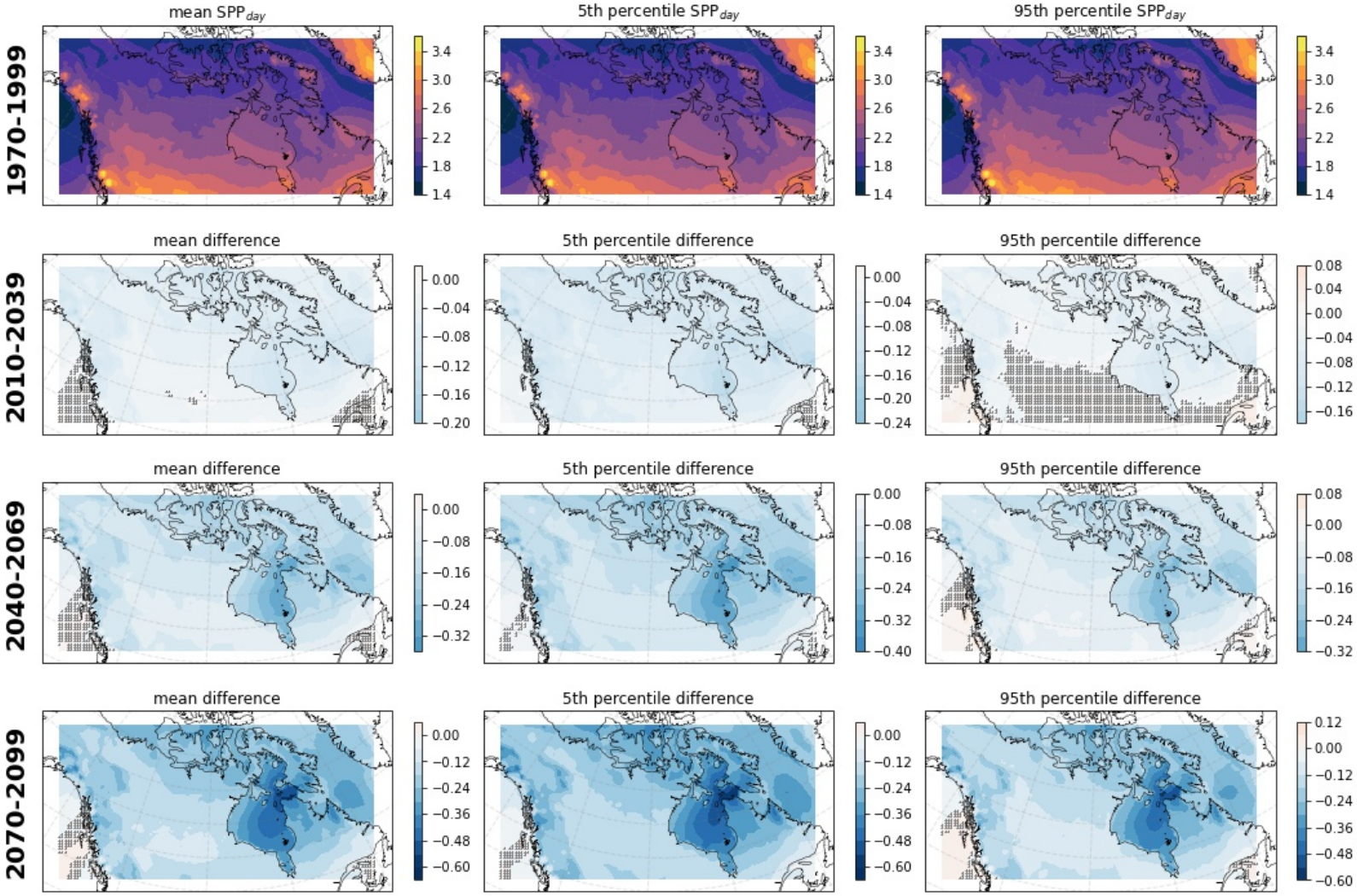

Figure 4.19: Ensemble mean (column 1), 5th percentile (column 2) and 95th percentile (column 3) daily solar power potential (SPP_{day}, MWh) in the reference period (1970-1999, row 1). Rows 2 to 4 show the absolute difference from the reference period (MWh) for the periods 2010-2039, 2040-2069, and 2070-2099. Individual plot colourbars display the range of values for that plot, scaled so that colours are comparable between plots of absolute value (row 1) absolute difference (rows 2-4). Non-robust changes are masked with stippling.

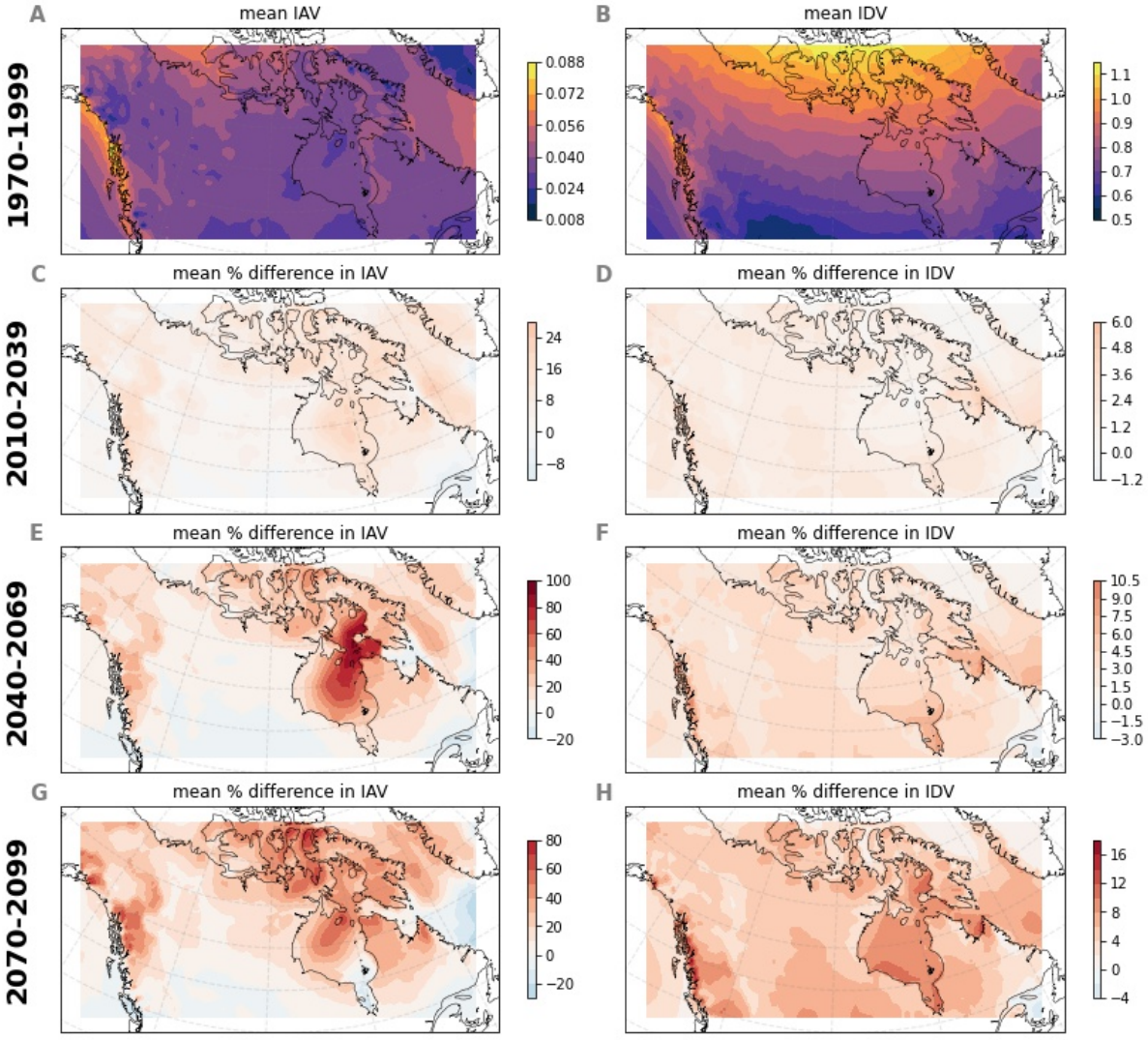

Figure 4.20: Daily solar power potential (SPP_{day}) inter-annual variability (column 1) and inter-daily variability (column 2) for the reference period (1970-1999, row 1, dimensionless) and ensemble mean percent change for the periods 2010-2039, 2040-2069, and 2070-2099 (rows 2 to 4). Individual plot colourbars display the range of values for that plot, scaled so that colours are comparable between plots of IAV change (C, E and G) and IDV change (D, F and H). For plots of absolute change in IAV and IDV see Figure C.8.

4.2.3 Analysis of potential causes

To assess the individual influence of changes in solar irradiance (DSR), temperature, and near-surface wind speed (SWS) on projected changes in *SPP*, mean SPP_{day} was also calculated using a combination of future (2070-2099) and reference period (1970-1999) inputs, as detailed in Section 3.7. As can be seen in Figure 4.21, changes due to DSR (panel C) contribute the most to the overall change in SPP_{day} (panel B), particularly over northern maritime regions. Over the continent, total change in DSR is smaller, and the influence of temperature (panel E) becomes of comparable influence to DSR. Over the Pacific Ocean, the opposing influences of increasing DSR and increasing temperature counteract one another, leading to small or non-robust changes in *SPP*. Change in wind speed (panel D) has a negligible impact over the entire study area.

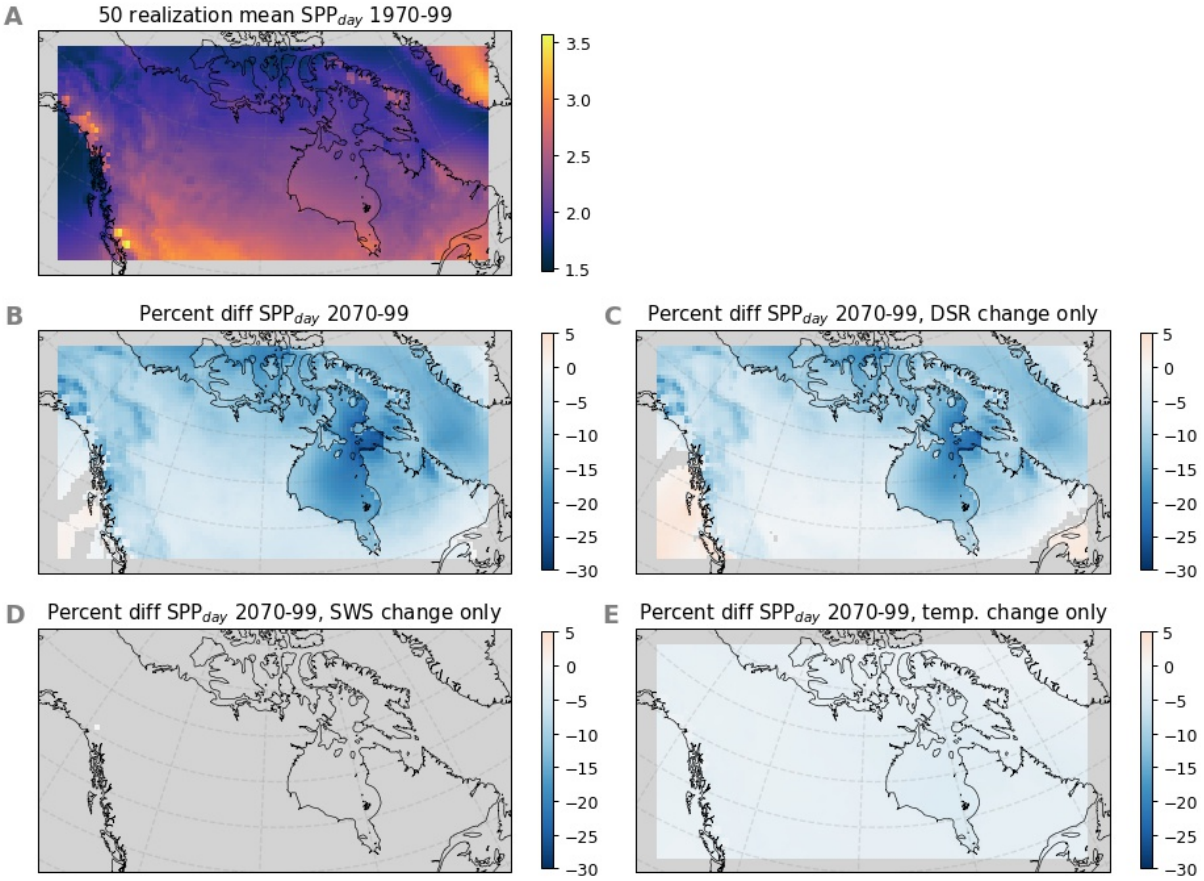

Figure 4.21: Ensemble mean SPP_{day} in the reference period (1970-1999, MWh, panel A) and percent difference in mean SPP_{day} by 2070-2099: (B) changing all factors; (C) changing DSR only; (D) changing SWS only; and (E) changing temperature only. Non-robust differences have been masked out with grey.

4.2.4 Contributors to change in downwelling solar irradiance

As the fundamental determinant of PV power, it is worthwhile to investigate potential causes of change in downwelling solar irradiance (DSR). As expected, DSR decreases robustly across the study domain over the 21st century (Figure 4.22, or Figure C.9 for change by season). Top of atmosphere irradiance has no long-term trend in CanRCM4 as transient solar forcing is not included in the model. Therefore, downwelling surface solar irradiance is determined by the extent of reflection, absorption and scattering of radiation in the atmosphere. The presence of cloud cover, radiatively active gases (largely water vapour), and aerosols are the major determinants of surface radiation (Haywood *et al.* 2011; Wild 2009). Aerosol forcings in CanRCM4 include transient black carbon, organic carbon, volcanic aerosols, and anthropogenic sulfate aerosols. Cloudiness is examined through changes in CanRCM4 total cloud area fraction (CLT) in combination with column condensed water (liquid and ice) content (CLW). As CLT does not take into account the importance of cloud-type in the amount of irradiance reflected, CLW provides some indication of the cloud characteristics (for example, low-level stratus cloud with high optical depth hold more water). Water vapour can be investigated through CanRCM4 column water vapour (CWV). Aerosol optical depth is not available from CanRCM4 output and has not been directly investigated here.

Correlation and partial correlation were calculated for DSR with potential influencing factors (see Section 3.6 for methods). However, daily means were used instead of monthly statistics in order to capture the highly variable nature of solar irradiance. Daily means were calculated using only time points where DSR>0 (as variations of, for example, cloud cover during night are irrelevant for this application). Correlations were computed for each

Table 4.4: Variables considered in a correlation analysis with mean downwelling shortwave radiation. Variables 2 through 4 are used as a set of 'all' controlling factors over land and variables 2 to 5 are used as a set of 'all' controlling factors over ocean. All variables were detrended with linear detrending and deseasonalized before calculating correlation or partial correlation.

	Variable	Abbreviation	Daily statistic
1	Downwelling shortwave radiation	DSR	$\text{Mean}_{DSR>0}$
2	Cloud area fraction	CLT	$\text{Mean}_{DSR>0}$
3	Column condensed (liquid & ice) water	CLW	$\text{Mean}_{DSR>0}$
4	Column water vapour	CWV	$\text{Mean}_{DSR>0}$
5	Sea ice[a]	SIC	Daily model output

[a]For ocean areas only.

realization using linearly detrended, deseasonalized (ordinal date mean removed[5]) values in the 1970 to 1999 period, and then averaged across the ensemble. Table 4.4 presents the factors of interest, the daily statistic used, and the abbreviated name used in the following discussion. AMJ was selected for in depth analysis of the correlations described below as it is a season of peak ice cover and solar irradiance across the study area.

Changes in cloudiness

Clouds generally reduce DSR through absorption or reflection of radiation. Local increases of DSR above its clear-sky value due to reflection from the sides of clouds are not modelled in CanRCM4. In the Arctic, low-level stratus clouds with high albedo are prevalent, particularly in the summer (Serreze & Barry 2014). Increases in cloudiness have been linked to decreases in DSR and/or PV potential over Canada under various climate change scenarios (e.g., Feron *et al.* 2021; Huber *et al.* 2016; Wild *et al.* 2015a; Zou *et al.* 2019). In general, the ocean areas of our study area are very cloudy, with some locations exceeding mean AMJ CLT of 90% in the reference period (Figure 4.22, panel C, or Figure C.10 for change by season). Robust changes in cloud characteristics are projected across the 21st century in CanRCM4 (Figure 4.22), for both CLT (panels C & D) and CLW (panels I & J). CLW shows strong increases across the domain (up to 100% in winter seasons) in all seasons except JAS (southern regions only), although more moderate increases are projected over Hudson Bay and other northern ocean areas (regions where large DSR decreases are projected, see Figure C.11). In contrast, CLT increases over most land areas, but decreases over many northern ocean areas (an absolute decrease in the range of 0 to 8% coverage, see Figure 4.22, panel D, or Figure C.10 for change by season). Projected decreases in ocean CLT contrast with the expected relationship between sea ice and cloud cover. Observational studies have shown a link between Arctic sea ice decline and increased cloudiness (Eastman & Warren 2010), and most modelling studies project increases in Arctic cloud cover (e.g., Trenberth & Fasullo 2009). While the reasoning behind the trend in CLT is unclear, overall, these results indicate that changes in cloud characteristics (i.e., optical depth) are more important in determining surface DSR in CanRCM4 than total cloud cover (i.e., areal extent). Consistent with this fact, CLW shows strong increases (up to 100%) that coincide with projected DSR decreases (and similar relationships with JAS increases).

As expected, correlations of DSR with CLT and CLW are negative (Figure 4.23, panels A and G), even when controlling for CWV and SIC (panels B and H). For CLT, correlations

[5]For DSR only, the seasonal cycle was removed using division rather than subtraction to assess relative change in DSR. This method accounts for the seasonally varying maximum possible DSR, which is controlled by top of atmosphere solar irradiance and impacts the absolute magnitude of DSR response to potential influencing factors.

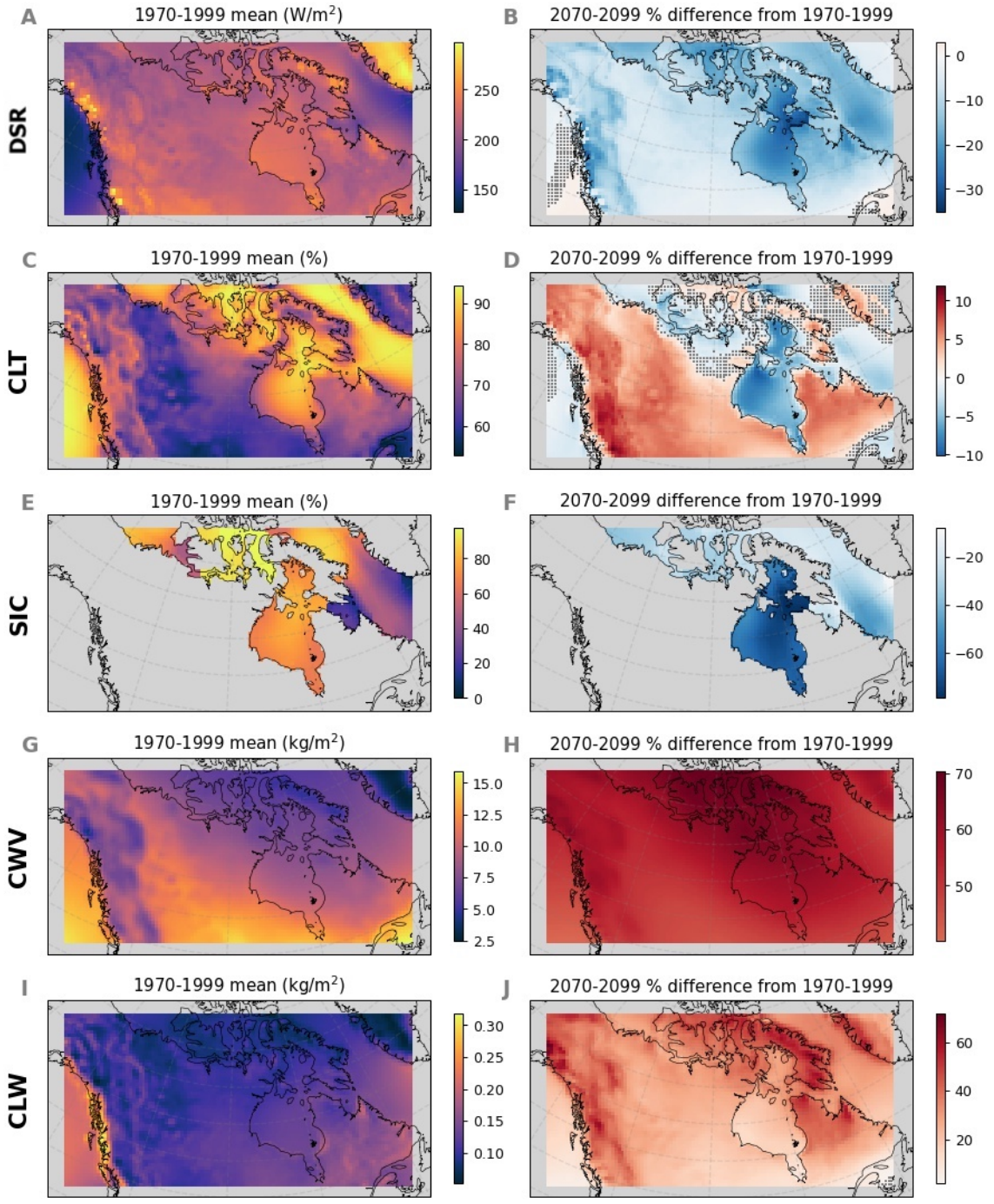

Figure 4.22: Ensemble mean in the reference period (column 1) and projected change (either absolute or percent, as indicated) in AMJ by 2070-2099 (column 2) for the variables: monthly mean downwelling shortwave radiation (DSR, A & B); monthly mean cloud area fraction (CLT, C & D); monthly mean sea ice concentration (SIC, E & F); monthly mean column water vapour (CWV, G & H); and monthly mean column liquid and ice water content (CLW, I & J). Non-robust changes in column 2 are masked with stippling. Grey areas over water in panel F indicates reference period sea ice concentration of less than 1%

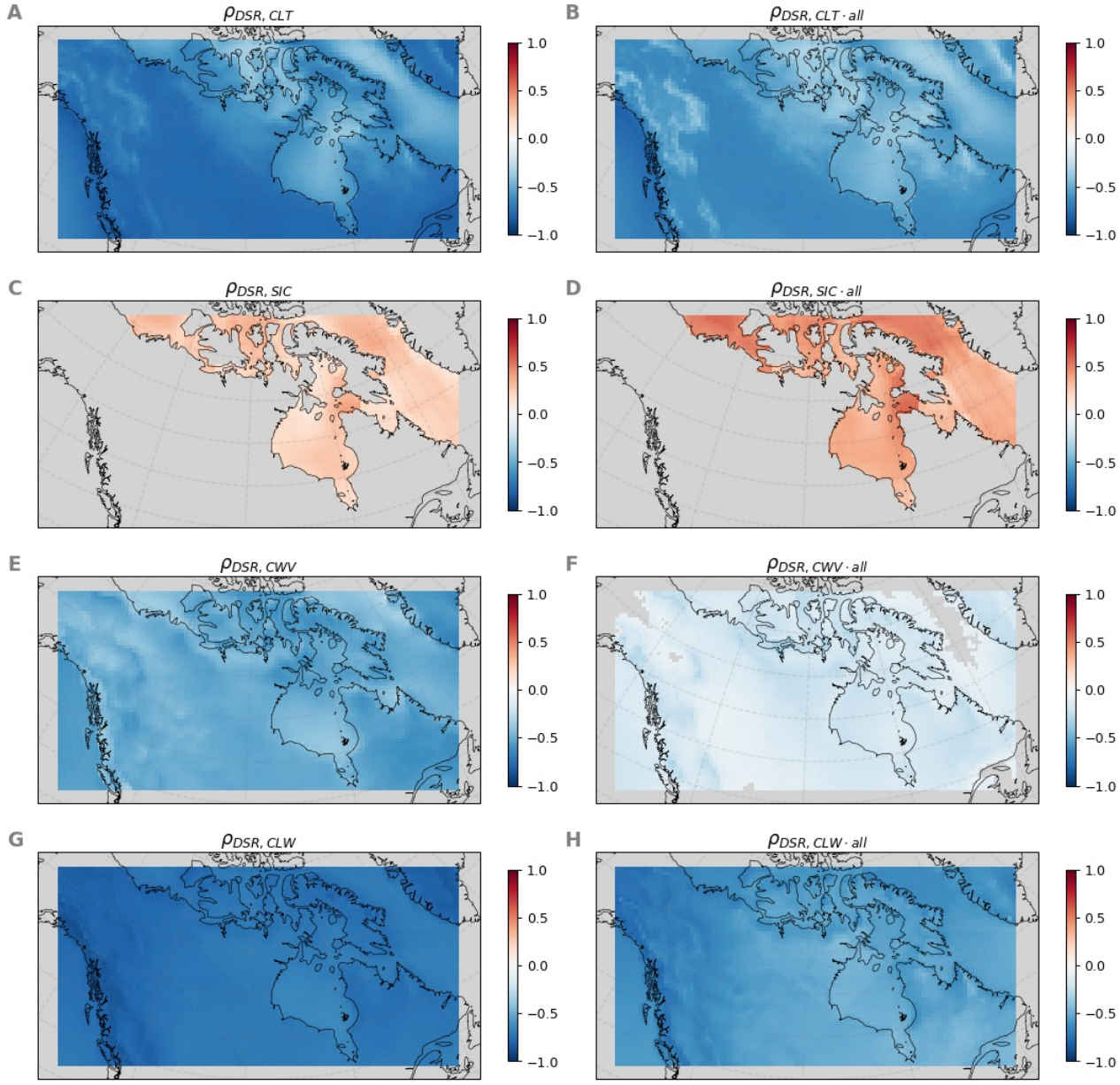

Figure 4.23: Ensemble mean AMJ correlations (column 1) and partial correlations (column 2) in the reference period (1970-1999) between downwelling shortwave radiation (DSR) and cloud area fraction (CLT, A & B), sea ice concentration (SIC, C & D) column water vapour (CWV, E & F), and column liquid and ice water content (CLW, G & H). Correlations and partial correlations are taken between daily means as described in Table 4.4. Partial correlations are taken controlling for all other land or water factors, as appropriate, however, controlling for sea ice over water areas does not notably change correlations. Non-significant ($p>0.05$) correlations are masked out with grey.

with DSR are stronger over land areas (where CLT has a long-term increasing trend in AMJ) than water areas (where CLT has a decreasing trend, panels A and B). This land-sea contrast may be because attenuation of DSR by Arctic clouds can be somewhat counteracted by multiple surface-cloud reflections when surface snow or ice is present (Serreze & Barry 2014). Under low-level stratus clouds, Wendler *et al.* (1981) found a 70% decrease in downward DSR in Barrow, Alaska during late summer (low surface albedo) relative to early spring (high surface albedo). Indeed, $\rho_{DSR,CLT \cdot all}$ over ocean areas is lower in AMJ (-0.53) than in JAS (-0.71, Figure 4.24). Controlling for sea ice does not considerably impact partial correlations in AMJ ($\rho_{DSR,CLT \cdot CWV,CLW}$ = -0.50; $\rho_{DSR,CLT \cdot all}$ = -0.53). However, this may be because sea ice is near to its greatest extent in AMJ, and so DSR will not be greatly impacted by small variations in the mostly ice-covered ocean.

In summary, column condensed water is more important than cloud area fraction in determining future changes to DSR (decreases) in CanRCM4. CLW increases robustly across the 21st century over both land and water, and is strongly negatively correlated with DSR. Meanwhile, CLT is also strongly negatively correlated with DSR, but is projected to decrease over Arctic ocean areas. Therefore, projected changes in DSR are likely linked to changes in cloud characteristics that result in more effective reflection of radiation, but not necessarily a change in overall cloud coverage over ocean areas.

Changes in column water vapour

Increasing atmospheric temperature is expected to result in increased total column water vapour (CWV) due to the Clausius-Clapeyron relationship (O'Gorman & Muller 2010). In addition to acting as a greenhouse gas, CWV is one of the most important radiatively active

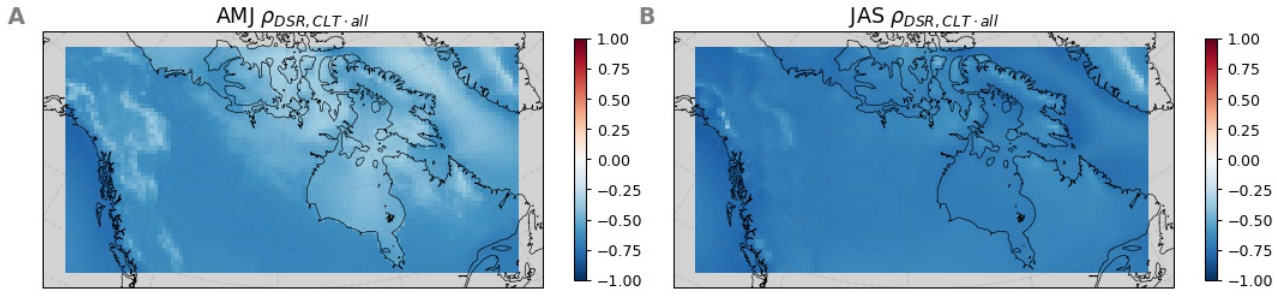

Figure 4.24: Ensemble mean AMJ and JAS partial correlations in the reference period (1970-1999) between downwelling shortwave radiation (DSR) and cloud area fraction (CLT) in AMJ (A) and JAS (B). Correlations are taken between daily means as described in Table 4.4. Partial correlations are taken controlling for all other land or water factors, as appropriate, however, controlling for sea ice over water areas does not notably change correlations. Non-significant (p>.05) correlations are masked out with grey.

gases in the shortwave (Kvalevåg & Myhre 2007), absorbing and scattering radiation in the atmosphere. Using HadGEM2-ES, Haywood *et al.* (2011) concluded that increases in atmospheric water vapour were the driving factor of large projected decreases in worldwide cloud-free DSR. Similarly, Bartók *et al.* (2017) cited atmospheric water vapour as the driver of projected 21st century DSR decreases for an RCM multi-model ensemble over Europe (where no significant change in cloudiness was projected). Our results project a robust increase in CWV by 2070-2099 in all seasons (Figure C.12), with increases up to 70% in AMJ (Figure 4.22, panel H). A moderate negative correlation between DSR and CWV is present, although partial correlation accounting for cloud factors and sea ice indicates a weak relationship (Figure 4.23, panel F). However, CWV is highly correlated with CLW (Figure 4.25) due to the dependence of column liquid water on the availability of water vapour. Controlling for cloudiness in correlations of CWV and DSR may not accurately represent the true importance of CWV on surface irradiance. Without model output clear-sky DSR and aerosol optical depth, it is difficult to unambiguously attribute all-sky DSR changes to changing column water vapour. Overall, we can conclude that column water vapour is projected to increase, and this likely contributes to decreases in DSR.

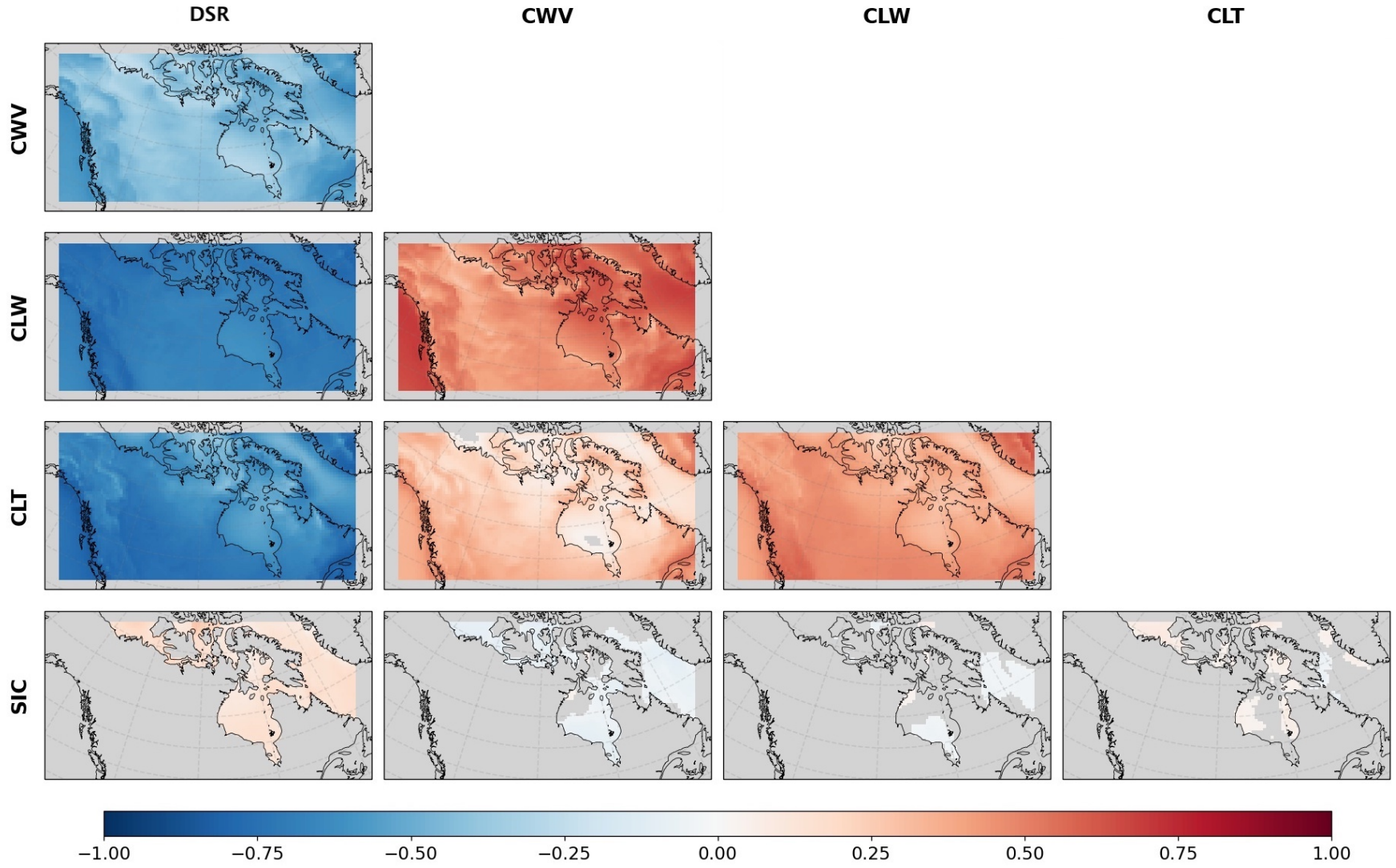

Figure 4.25: Correlation matrix for daily means as described in Table 4.4: downwelling shortwave radiation (DSR); column water vapour (CWV); column liquid and ice water content (CLW); cloud area fraction (CLT); and sea ice concentration (SIC). Land areas for SIC correlations as well as non-significant ($p>0.05$) correlations have been masked out with grey. Correlations were computed for each ensemble member for detrended, deseasonalized 1970-1999 values and then averaged across the ensemble.

69

Sea ice concentration and aerosols

Daily sea ice concentration (SIC) is weakly positively correlated with DSR (Figure 4.23, panel C), a relationship that grows stronger once cloud factors and column water vapour are accounted for (panel D). While our results indicate SIC is largely uncorrelated with cloud factors (Figure 4.25), decreases in sea ice have been linked to enhanced surface fluxes and conditions conducive to cloud formation (Huang *et al.* 2019). However, thick cloud cover is also connected to enhanced sea ice melt through increased downward longwave flux (Huang *et al.* 2019), although likely on timescales longer than the daily averages used in our correlation analysis. The positive correlation between SIC and DSR controlling for all factors indicates that other contributors to DSR variation are related to sea ice presence or absence.

Loss of sea ice can increase aerosols through generation of sea salt aerosols over the open ocean (Haywood *et al.* 2011). The CanRCM4 bulk aerosol scheme includes sea salt aerosols (see Scinocca *et al.* 2016 and references therein). Further, while aerosol forcings in RCP8.5 prescribe decreasing anthropogenic aerosol emissions, and decreases in aerosol optical depth (AOD) are projected for most of North America (e.g., Chen 2021; Haywood *et al.* 2011), not all parts of the globe are projected to see decreases in AOD (Westervelt *et al.* 2015). Many studies project increasing AOD over northern ocean areas over the 21st century. Haywood *et al.* (2011) project increases in AOD over ocean areas of the study area (and decreases over land areas) by the end of the 21st century, attributing marine region increases to sea-salt aerosol generation. Using GFDL CM3, Westervelt *et al.* (2015) projected increases in total AOD over Hudson Bay and northern Quebec and Labrador by the end of the 21st century. Huber *et al.* (2016) projected increases in AOD over northern Canada from 1995-99 to 2035-39 using E39C-A and ECHAM5-HAM. While Feron *et al.* (2021) used 7 CMIP5 models under RCP4.5, and projected decrease in aerosol optical depth by 2036-2065 in northern Canada, a relatively small impact of sea ice may be expected under this more moderate climate change scenario in the relatively near future. Overall, most studies agree that projected AOD will increase with climate change over northern high latitudes. AOD is not available as standard CanRCM4 output and so was not directly investigated here. However, future work could investigate its contributions to 21st century DSR change through available aerosol output fields from CanRCM4's parent model, CanESM2.

4.2.5 Conclusions

A robust decrease in 30-year mean SPP_{day} is projected over the entire study area by as early as 2010-2039. Arctic regions which currently experience seasonal ice coverage, as well as adjacent continental areas, are projected to see the largest decreases in SPP_{day}, of up

to 30%. The projected northern high-latitude decreases largely agree with other studies of solar photovoltaic potential or solar irradiance in northern Canada (e.g., Huber *et al.* 2016; Wild *et al.* 2015a; Zou *et al.* 2019). Seasonally, the greatest change is projected for AMJ over northern parts of the study area. Inter-annual and inter-daily variability are projected to increase across the 21st century, associated with less stable solar power potential, and have a strong connection to periods of sea-ice transition.

Decreases in *SPP* can be attributed to projected DSR reductions over the 21st century. DSR changes are associated with increasing cloud cover (CLT) over continental areas, and are strongly associated with changes in cloud characteristics (optical depth, indicated through increases in CLW) over both ocean and water areas. Over areas which typically experience seasonal ice or snow coverage in the reference period, diminishing extent may partially offset cloud cover changes by reducing the amount of radiation from multiple surface-cloud reflections. Changes in clear-sky (cloud free) DSR may also contribute to all-sky DSR changes through changes in water vapour or aerosols. Projected increases in atmospheric column water vapour are likely linked with decreases in overall DSR. While prescribed anthropogenic aerosol loading is expected to decrease in most future scenarios, prognostic aerosol concentrations may increase over parts of the study area (e.g., increased sea salt loading due to sea ice loss). Aerosol contributions were not investigated here because AOD is not a standard output field from CanRCM4. However, future investigation of available aerosol fields from CanESM2 may provide insight into the importance of aerosols in DSR changes.

4.3 Covariability of wind power and solar power

As discussed in previous chapters, both wind and solar power vary on sub-daily to inter-annual time scales, although the characteristics of their variability differ. Solar power, in particular, exhibits large, predictable daily and seasonal cycles, while wind power exhibits more stochastic behaviour with moderate seasonal variations. The covariability of wind and solar power is investigated here to assess if combined wind-solar installations could be used to minimize sub-annual power variability.

Correlations between detrended, deseasonalized monthly mean WPP_{day} and SPP_{day} (referred to for the remainder of this section as *WPP* and *SPP*) indicate that there is a weak negative correlation between solar and wind power in most of the study area (Figure 4.26, panel A). However, in the Canadian prairies, just leeward of the Rocky Mountains, correlations are weakly positive; the association of wind and solar power is likely due to the characteristic influence of flow over the Western Cordillera (e.g., dry Chinook winds). The largely negative correlations indicate that – relative to the monthly average – months of lower wind power are more likely to have slightly higher solar power, and vice versa. This correlation structure remains largely constant across the 21st century, with the exception of the Labrador Sea (Figure 4.26, A and C). If the seasonal cycle is retained when taking correlations, relationships are much stronger and negative across the study area, with the greatest correlations over Pacific Canada (Figure 4.26, B and D). This result indicates that the annual cycle of wind and solar power complement each other such that months/seasons of low *WPP* can be expected to have higher than average *SPP*, and vice versa, and that combined wind-solar installations could reduce seasonal variability in power output. The annual cycles of *WPP* and *SPP* are illustrated for the communities of focus in Figure 4.27. While wind power production typically peaks in OND and experiences a summer minimum, solar power production peaks in the summer months with a winter minimum. Correlations of monthly *WPP* with *SPP* including the seasonal cycle range between -0.10 and -0.51 for the communities of focus (see Table C.3 in Appendix C). Figure 4.28 shows scatter plots of *WPP* and *SPP* for detrended values in Arviat, both deseasonalized and including the seasonal cycle. The weak correlations of *WPP* with *SPP* are apparent from the rounded point clouds. Also apparent in OND and JFM are a high number of zero values for *SPP* due to months of total darkness.

Since monthly mean wind and solar power are negatively correlated due to their approximately oppositely-phased seasonal cycles, a combined wind/solar installation reduces intra-annual variability. The coefficient of variation (CoV) of monthly mean values is used to assess intra-annual variability relative to average power output. As shown in Figure 4.29, the CoV of a combined installation of equal capacity wind and solar power for 1970-1999

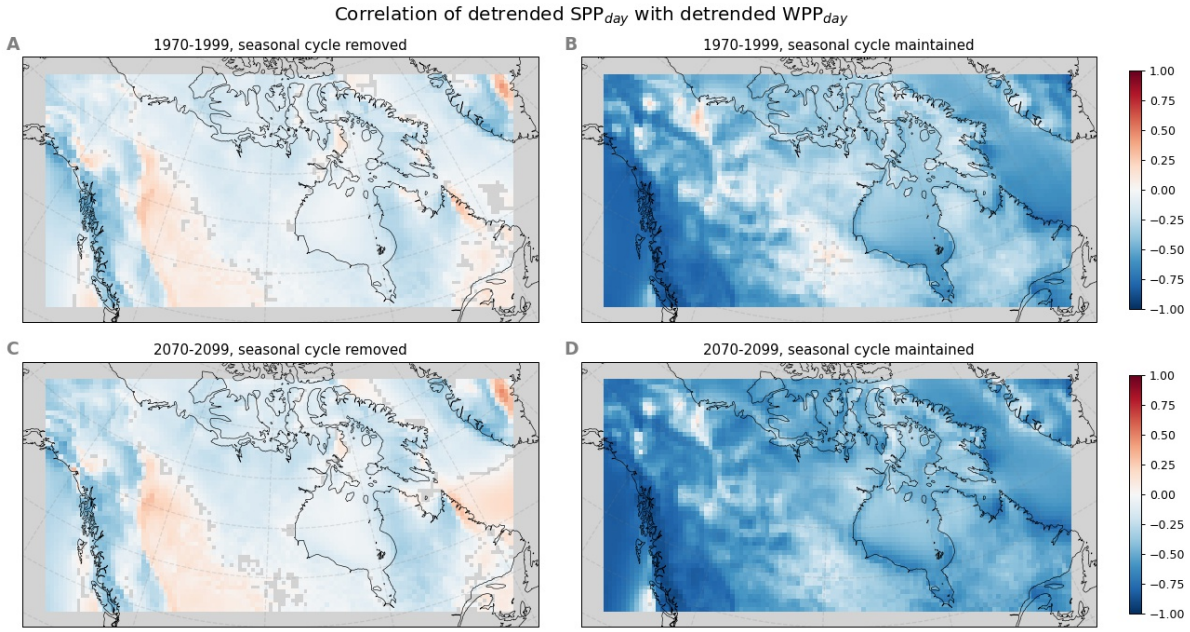

Figure 4.26: Correlations between monthly mean *WPP* and monthly mean *SPP* in the reference period (1970-1999, A and B) and end of century (2070-2099, C and D), for detrended values with seasonal cycle removed (A and C) and detrended values retaining the seasonal cycle (B and D). Non-significant ($p>0.05$) values have been masked with grey.

(panel A) is lower than the CoV of either solely wind (panel C) or solely solar (panel E). Installation of double the wind power capacity compared to solar capacity (i.e., doubling the number of turbines per grid cell in our analysis, panel D) or double the solar power capacity to wind (doubling the solar panels per grid cell, panel F) results in higher CoV or marginal decreases across the domain. Large decreases in CoV are seen only in coastal and mountainous British Columbia for a two-to-one solar to wind ratio. Over the 21st century, the combined CoV is expected to decrease in some northern maritime regions (panel B), where we see greatest change in *WPP* (see Figure 4.4), and to increase in other regions. These changes are likely driven by individual changes in IDV of both wind and solar power, as discussed in the sections above, rather than changes in covariability of the two. The negative correlations between monthly wind and solar power as well as reduced CoV from combined installations show that combined power generation stabilizes power supplies over the course of the year, with increasing stability in most of the Canadian high latitudes into the 21st century.

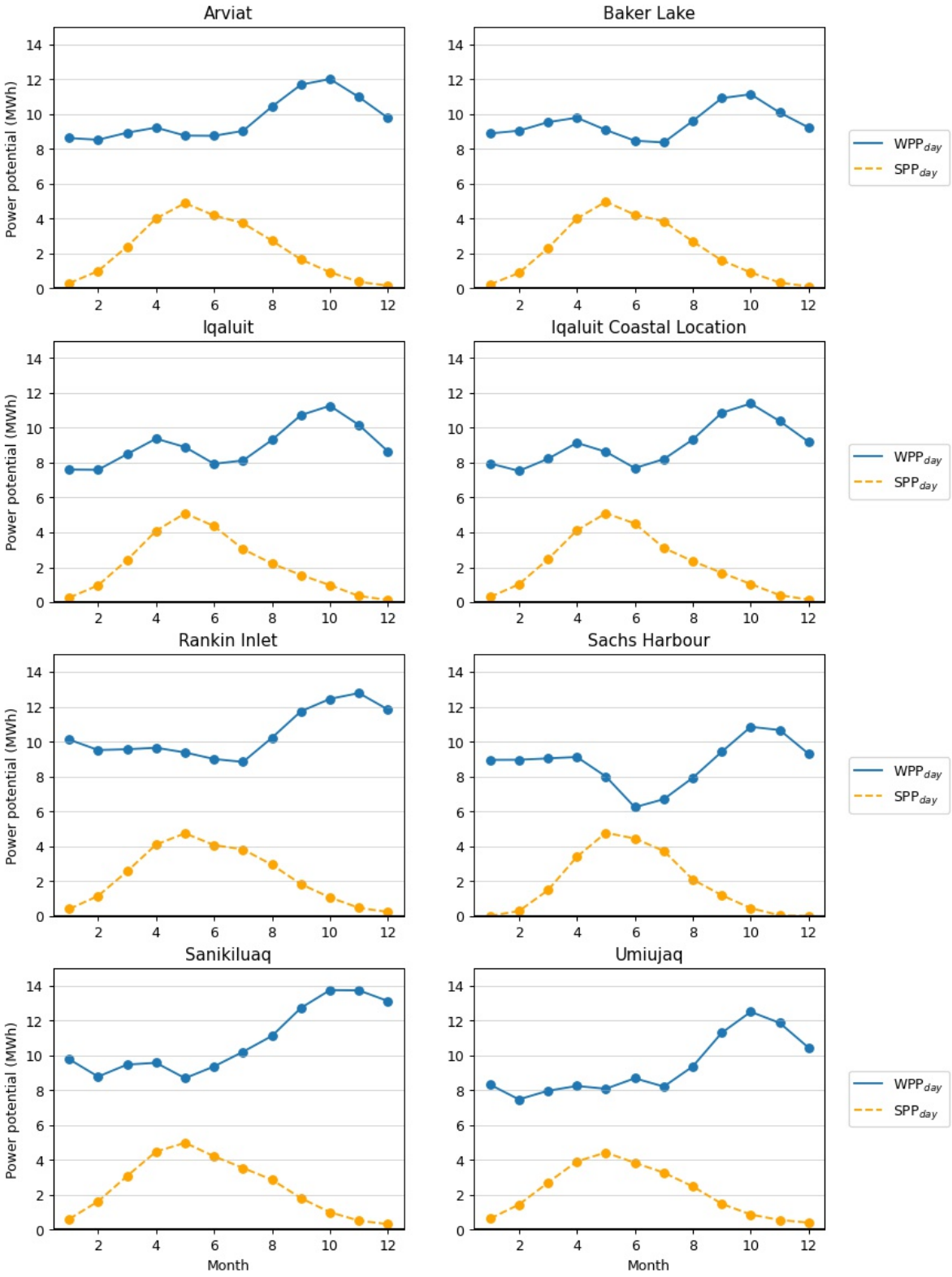

Figure 4.27: Annual cycle of monthly mean WPP_{day} and monthly mean SPP_{day} in 1970-1999 for communities of focus, assuming an equal installation capacity of 900 kW for both power types. Values are taken from the closest gridpoint to the latitude and longitude of each community.

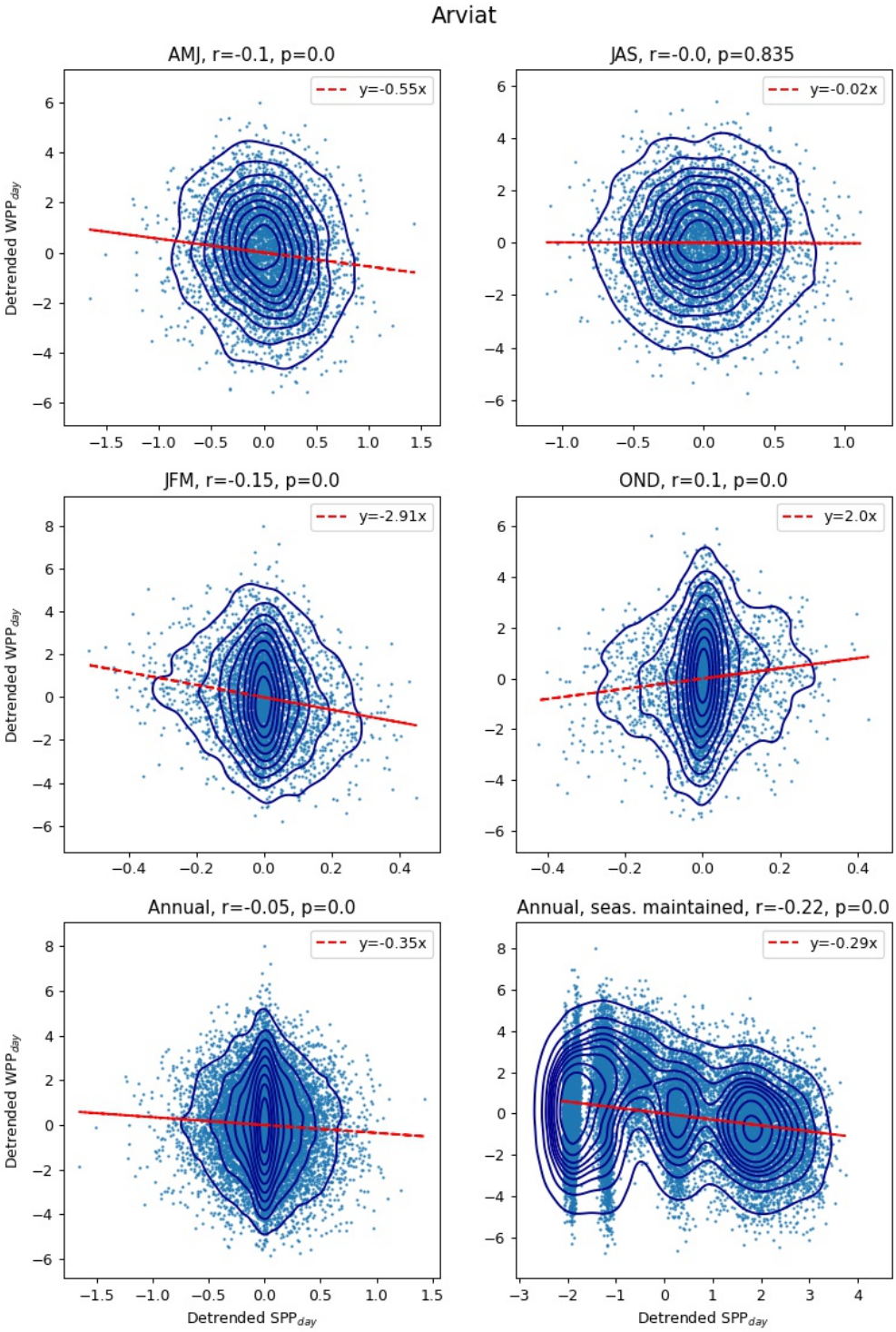

Figure 4.28: Scatter plots of anomalies (detrended values with the seasonal cycle removed) of *WPP* and *SPP* in Arviat in the reference period, except in the final panel in column 2, where detrended values with the seasonal cycle retained are presented.

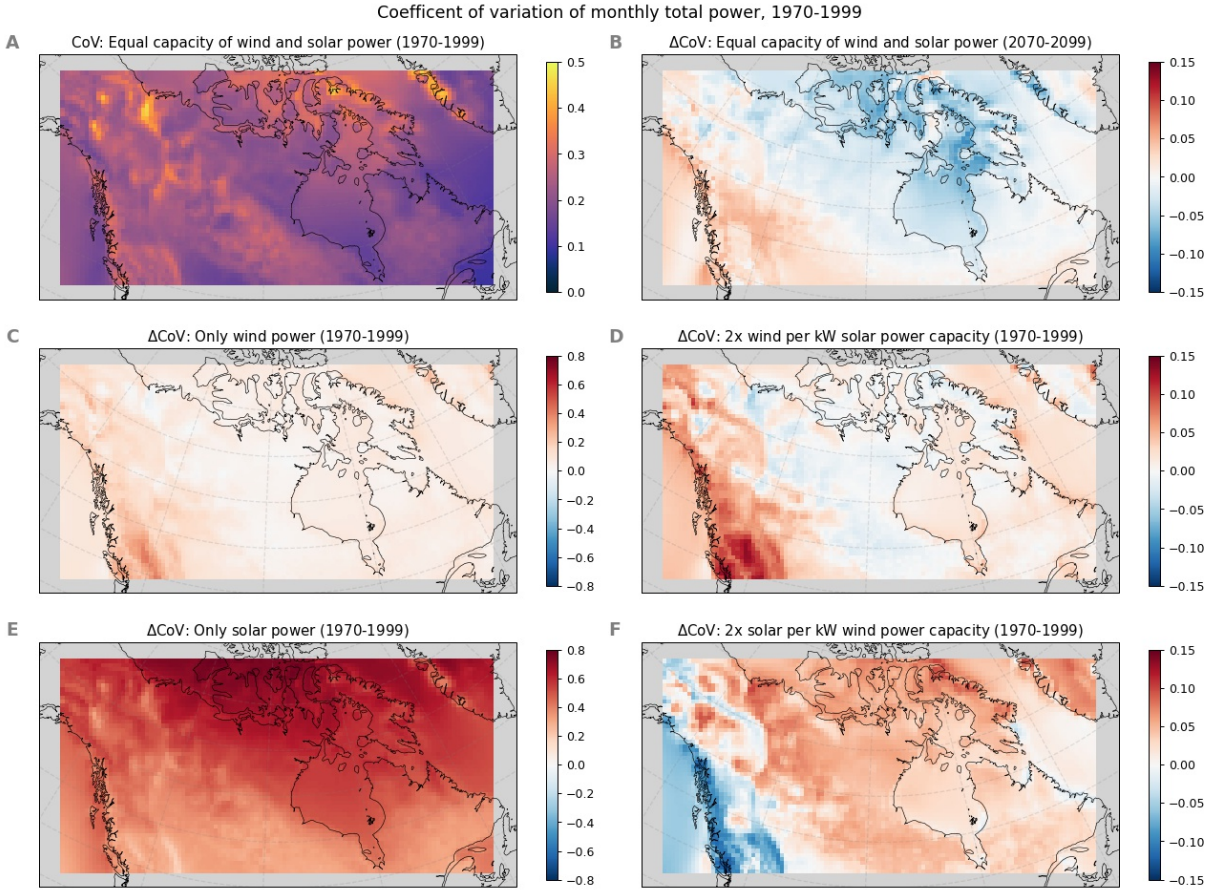

Figure 4.29: Coefficient of variation (CoV) of monthly mean *WPP* and monthly mean *SPP*, and its changes (ΔCoV), for various combinations of wind and solar power capacity: A) CoV in the reference period assuming equal capacity of wind and solar installed; B) absolute change in CoV by 2070-2099 from A (the reference period); C) absolute difference in CoV from A, with only wind power installed; D) absolute difference in CoV from A, when wind capacity is twice that of solar; E) absolute difference in CoV from A, only solar power installed; F) absolute difference in CoV from A, when solar capacity is twice that of wind. Note different scale bars between panels in column 1 and panels in column 2. For maps of absolute values, see Figure C.13.

Chapter 5

Conclusions

The objectives of this work were to use the large ensemble of the CanRCM4 regional climate model to assess current and future wind and solar energy potential, variability, and covariability in the Canadian north, and to consider potential mechanisms of change.

Overall, robust increases in annual average wind power potential (*WPP*) are projected (up to 30%) across the northernmost part of the study area by 2070-2099, with changes most pronounced in cold seasons. Decreases in *WPP* are projected for southern areas. Solar power potential (*SPP*) is projected to experience decreases across the study area in all seasons except JAS, with robust changes emerging by as early as 2010-2039, and being most prominent in AMJ. These results largely agree with other studies projecting *WPP* or wind speed increases in the far north and decreases in southern Canada (e.g., Gernaat *et al.* 2021; Jeong & Sushama 2019; Karnauskas *et al.* 2018; Mioduszewski *et al.* 2018) and decreases in *SPP* or downwelling shortwave radiation across the domain (e.g., Crook *et al.* 2011; Huber *et al.* 2016; Wild *et al.* 2015a; Zou *et al.* 2019).

Inter-annual variability (IAV) and inter-daily variability (IDV) are inversely related to power stability, and are generally greater for *SPP* than *WPP*. For *WPP*, southern increases and northern decreases are seen for both IAV and IDV. IDV trends are due to changes that tend to dampen (heighten) the seasonal cycle of *WPP* in the north (south). For solar power potential, IAV and IDV are projected to increase across the domain over the 21st century, such that the greatest changes have a strong connection over the northern ocean to periods of sea ice transition. For the focal communities, *WPP* stability is projected to increase, while *SPP* stability is projected to decrease.

Monthly mean *WPP* and *SPP* are negatively correlated, with approximately oppositely-phased seasonal cycles. Combined wind/solar installations are therefore shown to reduce sub-annual variability relative to individual installations of either wind or solar. Combined power generation may stabilize power supplies over the course of the year, with increasing

stability in most of the Canadian high latitudes into the 21st century.

Drivers of change in *WPP* and *SPP* are complex, but changes in sea ice across the 21st century will play an important role for both *WPP* and *SPP*. Over the northern ocean regions, increases in *WPP* are weakly correlated with sea ice loss and associated reduced roughness lengths, while the influence of decreased atmospheric stability in cool-season sea ice loss is not apparent. Increases (decreases) in storminess (as defined in this study) play a role in northern-coastal (southern-interior) changes, but changes in synoptic storm activity are difficult to distinguish from shifts in wind speed distribution. CanESM2/CanRCM4 underestimates SIC relative to historical observations (Kushner *et al.* 2018). Moreover, CanRCM4 simulates larger future surface air temperature change compared to other NA-CORDEX RCMs (Bukovsky & Mearns 2020). Therefore, it is likely that robust, substantial changes in the far north are apparent earlier in CanRCM4 than other models.

Decreases in *SPP* can be attributed to projected DSR reductions over the 21st century. DSR changes are strongly associated with changes in cloud characteristics (optical depth, indicated through large increases in column condensed water content) over all areas. Large projected increases in atmospheric column water vapour may also be linked with decreases in overall DSR. While prescribed anthropogenic aerosol loading is expected to decrease in most future scenarios, prognostic aerosols may increase in the study area (e.g., increased sea salt loading due to sea ice loss). Aerosol contributions were not investigated here because AOD is not a standard output field from CanRCM4. Inclusion of AOD and clear-sky DSR in future RCM output would improve investigations into mechanisms of *SPP* change. Alternatively, examining aerosol output fields from the driving model, CanESM2, may clarify the relative contribution of changing AOD over the 21st century. The cloud area fraction response (decreases) in CanRCM4 over areas of declining sea ice also merits further study. The trend opposes the expected relationship given projected DSR decreases, and the results of many other studies. Assessment of changes in variability of cloud fraction over time may also be useful, and potentially linked to increasing *SPP* variability.

Other factors not directly assessed in this study likely play a role in *WPP* and *SPP* variability and change, including changing large scale circulation patterns and ocean-atmosphere oscillations. While the impacts of these factors are indirectly felt through storminess and sea ice measures, this could be investigated in future work. Further, our measure of storminess does not allow for changes in cyclonic storm activity to be distinguished from shifts in wind speed distributions. An interesting direction of future research would be the use of alternate measures of synoptic activity (e.g., mean sea level pressure or lower-tropospheric vorticity) to better understand contributions of changes in storm properties.

The decision to use 3-hr model output for estimates of wind and solar power resources in this study increases precision relative to daily or monthly means (Karnauskas *et al.* 2018).

However, climate models contain biases in their estimates of absolute wind and solar resources (e.g., Wild *et al.* 2015b), and so are possibly most useful in assessments of variability and change. With this in mind, future work may benefit from a simplification of our methods. Using monthly means and/or exclusion of the Monin-Obukhov Stability Theory in extrapolation of wind speeds would substantially reduce required computing resources, while retaining reliable information about projected change and climate variability. Alternatively, inclusion of hub height wind speeds (e.g., 100 m) in future model output would be valuable for assessments of *WPP* variability and change, and would negate the need for trade-offs between computing time and accuracy.

Using the CanRCM4 large ensemble has allowed for partitioning and characterization of internal climate variability and projected forced change. As a regional climate model, CanRCM4 also provides better representation of geographical features and associated influences on atmospheric processes than ESM ensembles. However, use of a single model has increased the potential for uncertainty associated with model bias, which becomes increasingly important over internal variability at longer timescales (Hawkins & Sutton 2009). The notable sea ice bias in CanRCM4/CanESM2 will certainly impact projected times of emergence in the present study, resulting in an early-emergence bias for features associated with sea ice loss. Future work could consider using the NA-CORDEX multi-model ensemble of RCMs to study wind and solar power in the Canadian north, similar to the work of Chen (2020, 2021) for the USA. However, consideration should first be given to more detailed treatment of aerosols in these RCMs, which has marked impacts on DSR projections (Chen 2021).

Overall, northern regions of Canada and our focal communities show high potential for renewable energy generation across the 21st century, particularly for wind energy. Projected increases to wind power resources and wind power stability in the focal communities could enhance the cost-savings and emissions reductions predicted based on current climate assessments (Das & Canizares 2016b). Despite projected decreases to *SPP*, our results suggest that combined wind-solar installations will produce more stable annual power supplies relative to solely wind or solar power, both now and in the future. With ever improving technologies and declining costs, the viability of renewable power in the north is likely to become even more certain in coming years.

Bibliography

1. Abatzoglou, J. T., Williams, A. P. & Barbero, R. Global emergence of anthropogenic climate change in fire weather indices. *Geophysical Research Letters* **46,** 326–336 (2019).
2. Abdella, K. & McFarlane, N. A new second-order turbulence closure scheme for the planetary boundary layer. *Journal of the Atmospheric Sciences* **54,** 1850–1867 (1997).
3. Abdella, K. & McFarlane, N. Parameterization of the surface-layer exchange coefficients for atmospheric models. *Boundary-Layer Meteorology* **80,** 223–248 (1996).
4. Arya, P. S. *Introduction to Micrometeorology* (Elsevier, 2001).
5. Atkinson, D. E. Observed storminess patterns and trends in the circum-Arctic coastal regime. *Geo-Marine Letters* **25,** 98–109 (2005).
6. Augustine, J. A. & Hodges, G. B. Variability of Surface Radiation Budget Components Over the US From 1996 to 2019—Has Brightening Ceased? *Journal of Geophysical Research: Atmospheres* **126,** e2020JD033590 (2021).
7. Baas, P., Bosveld, F. & Burgers, G. The impact of atmospheric stability on the near-surface wind over sea in storm conditions. *Wind Energy* **19,** 187–198 (2016).
8. Barthelmie, R. The effects of atmospheric stability on coastal wind climates. *Meteorological Applications* **6,** 39–47 (1999).
9. Bartók, B. *et al.* Projected changes in surface solar radiation in CMIP5 global climate models and in EURO-CORDEX regional climate models for Europe. *Climate Dynamics* **49,** 2665–2683 (2017).
10. Beljaars, A. & Holtslag, A. Flux parameterization over land surfaces for atmospheric models. *Journal of Applied Meteorology* **30,** 327–341 (1991).
11. Beniston, M. *et al.* Future extreme events in European climate: an exploration of regional climate model projections. *Climatic Change* **81,** 71–95 (2007).
12. Bichet, A., Wild, M., Folini, D. & Schär, C. Causes for decadal variations of wind speed over land: Sensitivity studies with a global climate model. *Geophysical Research Letters* **39** (2012).
13. Bukovsky, M. S. & Mearns, L. O. Regional climate change projections from NA-CORDEX and their relation to climate sensitivity. *Climatic Change* **162,** 645–665 (2020).

14. Candlish, L. M., Iacozza, J., Lukovich, J. V., Horton, B. & Barber, D. G. Sea ice climatology in the Canadian Western Arctic: thermodynamic versus dynamic controls. *International Journal of Climatology* **35,** 1867–1880 (2015).

15. Carrillo, C., Montaño, A. O., Cidrás, J. & Dıaz-Dorado, E. Review of power curve modelling for wind turbines. *Renewable and Sustainable Energy Reviews* **21,** 572–581 (2013).

16. Chen, L. Impacts of climate change on wind resources over North America based on NA-CORDEX. *Renewable Energy* **153,** 1428–1438 (2020).

17. Chen, L. Uncertainties in solar radiation assessment in the United States using climate models. *Climate Dynamics* **56,** 665–678 (2021).

18. Cheng, C. S., Lopes, E., Fu, C. & Huang, Z. Possible impacts of climate change on wind gusts under downscaled future climate conditions: Updated for Canada. *Journal of Climate* **27,** 1255–1270 (2014).

19. Christensen, J. H., Hewitson, B., Busuioc, A., *et al. Regional climate projections. In 'Climate change 2007: the physical science basis. Contribution of Working Group I to the Fourth Assessment Report of the Intergovernmental Panel on Climate Change'.(Eds S Solomon, D Qin, M Manning, Z Chen, M Marquis, KB Averyt, M Tignor, HL Miller) pp. 847–940* 2007.

20. Collins, M. *et al.* in *Climate Change 2013-The Physical Science Basis: Contribution of Working Group I to the Fifth Assessment Report of the Intergovernmental Panel on Climate Change* 1029–1136 (Cambridge University Press, 2013).

21. Côté, J. *et al.* The operational CMC–MRB global environmental multiscale (GEM) model. Part I: Design considerations and formulation. *Monthly Weather Review* **126,** 1373–1395 (1998).

22. Crook, J. A., Jones, L. A., Forster, P. M. & Crook, R. Climate change impacts on future photovoltaic and concentrated solar power energy output. *Energy & Environmental Science* **4,** 3101–3109 (2011).

23. Cutforth, H. & Judiesch, D. Long-term changes to incoming solar energy on the Canadian Prairie. *Agricultural and Forest Meteorology* **145,** 167–175 (2007).

24. Daines, J. T., Monahan, A. H. & Curry, C. L. Model-based projections and uncertainties of near-surface wind climate in western Canada. *Journal of Applied Meteorology and Climatology* **55,** 2229–2245 (2016).

25. Das, I. & Canizares, C. *Renewable Energy Deployment in Canadian Arctic â Phase II: Feasibility Studies Report on Selected Communities of Nunavut and Northwest Territories* tech. rep. (University of Waterloo, Waterloo Institute of Sustainable Energy, Waterloo, ON, 2016), 77.

26. Das, I. & Canizares, C. *Renewable Energy Deployment in Canadian Arctic Phase I: Pre-Feasibility Studies and Community Engagement Report* tech. rep. (University of Waterloo, Waterloo Institute of Sustainable Energy, Waterloo, ON, 2016), 72.

27. Demain, C., Journée, M. & Bertrand, C. Evaluation of different models to estimate the global solar radiation on inclined surfaces. *Renewable Energy* **50,** 710–721 (2013).

28. Deng, K., Azorin-Molina, C., Minola, L., Zhang, G. & Chen, D. Global Near-Surface Wind Speed Changes over the Last Decades Revealed by Reanalyses and CMIP6 Model Simulations. *Journal of Climate* **34,** 2219–2234 (2021).

29. Deser, C., Knutti, R., Solomon, S. & Phillips, A. S. Communication of the role of natural variability in future North American climate. *Nature Climate Change* **2,** 775–779 (2012).

30. Deser, C., Phillips, A., Bourdette, V. & Teng, H. Uncertainty in climate change projections: the role of internal variability. *Climate Dynamics* **38,** 527–546 (2012).

31. Deser, C., Tomas, R., Alexander, M. & Lawrence, D. The seasonal atmospheric response to projected Arctic sea ice loss in the late twenty-first century. *Journal of Climate* **23,** 333–351 (2010).

32. Diaconescu, E. P., Gachon, P., Laprise, R. & Scinocca, J. F. Evaluation of precipitation indices over North America from various configurations of regional climate models. *Atmosphere-Ocean* **54,** 418–439 (2016).

33. Donat, M. *et al.* Reanalysis suggests long-term upward trends in European storminess since 1871. *Geophysical Research Letters* **38** (2011).

34. Dutton, E. G. *et al.* Decadal variations in surface solar irradiance as observed in a globally remote network. *Journal of Geophysical Research: Atmospheres* **111** (2006).

35. Earl, N., Dorling, S., Hewston, R. & Von Glasow, R. 1980–2010 variability in UK surface wind climate. *Journal of Climate* **26,** 1172–1191 (2013).

36. Eastman, R. & Warren, S. G. Interannual variations of Arctic cloud types in relation to sea ice. *Journal of Climate* **23,** 4216–4232 (2010).

37. Emergya Wind Technologies. *DW54 900kW* Brochure.

38. Emergya Wind Technologies. *DW61 900kW* Brochure.

39. Eyring, V. *et al.* Overview of the Coupled Model Intercomparison Project Phase 6 (CMIP6) experimental design and organization. *Geoscientific Model Development* **9,** 1937–1958 (2016).

40. Feron, S., Cordero, R. R., Damiani, A. & Jackson, R. B. Climate change extremes and photovoltaic power output. *Nature Sustainability* **4,** 270–276 (2021).

41. Feser, F. *et al.* Storminess over the North Atlantic and northwestern Europe—A review. *Quarterly Journal of the Royal Meteorological Society* **141,** 350–382 (2015).

42. Flato, G. *et al.* in *Climate change 2013: the physical science basis. Contribution of Working Group I to the Fifth Assessment Report of the Intergovernmental Panel on Climate Change* 741–866 (Cambridge University Press, 2014).

43. Foken, T. 50 years of the Monin–Obukhov similarity theory. *Boundary-Layer Meteorology* **119,** 431–447 (2006).

44. Francis, J. A. & Vavrus, S. J. Evidence for a wavier jet stream in response to rapid Arctic warming. *Environmental Research Letters* **10,** 014005 (2015).

45. Frieler, K. *et al.* Assessing the impacts of 1.5 C global warming–simulation protocol of the Inter-Sectoral Impact Model Intercomparison Project (ISIMIP2b). *Geoscientific Model Development* **10,** 4321–4345 (2017).

46. Gernaat, D. E. *et al.* Climate change impacts on renewable energy supply. *Nature Climate Change* **11,** 119–125 (2021).

47. Giorgi, F. & Bi, X. Time of emergence (TOE) of GHG-forced precipitation change hot-spots. *Geophysical Research Letters* **36** (2009).

48. Harvey, B., Shaffrey, L. & Woollings, T. Equator-to-pole temperature differences and the extra-tropical storm track responses of the CMIP5 climate models. *Climate Dynamics* **43,** 1171–1182 (2014).

49. Hausfather, Z. & Peters, G. P. Emissions – the 'business as usual' story is misleading. *Nature* **577,** 618–620 (2020).

50. Hawkins, E. & Sutton, R. The potential to narrow uncertainty in regional climate predictions. *Bulletin of the American Meteorological Society* **90,** 1095–1108 (2009).

51. Hawkins, E. & Sutton, R. Time of emergence of climate signals. *Geophysical Research Letters* **39** (2012).

52. Haywood, J. M. *et al.* The roles of aerosol, water vapor and cloud in future global dimming/brightening. *Journal of Geophysical Research: Atmospheres* **116** (2011).

53. Holmgren, W. F., Hansen, C. W. & Mikofski, M. A. pvlib python: A python package for modeling solar energy systems. *Journal of Open Source Software* **3,** 884 (2018).

54. Hu, Z.-Z., Kumar, A., Jha, B. & Huang, B. An analysis of forced and internal variability in a warmer climate in CCSM3. *Journal of Climate* **25,** 2356–2373 (2012).

55. Huang, Y. *et al.* Thicker clouds and accelerated Arctic sea ice decline: The atmosphere-sea ice interactions in spring. *Geophysical Research Letters* **46,** 6980–6989 (2019).

56. Huber, I. *et al.* Do climate models project changes in solar resources? *Solar Energy* **129,** 65–84 (2016).

57. Hueging, H., Haas, R., Born, K., Jacob, D. & Pinto, J. G. Regional changes in wind energy potential over Europe using regional climate model ensemble projections. *Journal of Applied Meteorology and Climatology* **52,** 903–917 (2013).

58. Hundecha, Y., St-Hilaire, A., Ouarda, T., El Adlouni, S. & Gachon, P. A nonstationary extreme value analysis for the assessment of changes in extreme annual wind speed over the Gulf of St. Lawrence, Canada. *Journal of Applied Meteorology and Climatology* **47,** 2745–2759 (2008).

59. International Electrotechnical Commission. *IEC 61400-12-1: Wind turbines-Part 12-1: Power performance measurements of electricity producing wind turbines* (Geneva, Switzerland, 2005).

60. Jaiser, R., Dethloff, K., Handorf, D., Rinke, A. & Cohen, J. Impact of sea ice cover changes on the Northern Hemisphere atmospheric winter circulation. *Tellus A: Dynamic Meteorology and Oceanography* **64,** 11595 (2012).

61. Jeong, D. I., Cannon, A. J. & Morris, R. J. Projected changes to wind loads coinciding with rainfall for building design in Canada based on an ensemble of Canadian regional climate model simulations. *Climatic Change* **162,** 821–835 (2020).

62. Jeong, D. I., Cannon, A. J. & Zhang, X. Projected changes to extreme freezing precipitation and design ice loads over North America based on a large ensemble of Canadian regional climate model simulations. *Natural Hazards and Earth System Sciences* **19,** 857–872 (2019).

63. Jeong, D. I. & Sushama, L. Projected changes to mean and extreme surface wind speeds for North America based on regional climate model simulations. *Atmosphere* **10,** 497 (2019).

64. Jeong, D. I. & Sushama, L. Rain-on-snow events over North America based on two Canadian regional climate models. *Climate Dynamics* **50,** 303–316 (2018).

65. Jerez, S. *et al.* The CLIMIX model: A tool to create and evaluate spatially-resolved scenarios of photovoltaic and wind power development. *Renewable and Sustainable Energy Reviews* **42,** 1–15 (2015).

66. Jerez, S. *et al.* The impact of climate change on photovoltaic power generation in Europe. *Nature Communications* **6,** 1–8 (2015).

67. Johnson, D. L. & Erhardt, R. J. Projected impacts of climate change on wind energy density in the United States. *Renewable Energy* **85,** 66–73 (2016).

68. Jung, C. & Schindler, D. Changing wind speed distributions under future global climate. *Energy Conversion and Management* **198,** 111841 (2019).

69. Jung, C. & Schindler, D. On the inter-annual variability of wind energy generation–a case study from Germany. *Applied Energy* **230,** 845–854 (2018).

70. Jung, C. & Schindler, D. The annual cycle and intra-annual variability of the global wind power distribution estimated by the system of wind speed distributions. *Sustainable Energy Technologies and Assessments* **42,** 100852 (2020).

71. Karnauskas, K. B., Lundquist, J. K. & Zhang, L. Southward shift of the global wind energy resource under high carbon dioxide emissions. *Nature Geoscience* **11,** 38–43 (2018).

72. Kent, E. C., Fangohr, S. & Berry, D. I. A comparative assessment of monthly mean wind speed products over the global ocean. *International Journal of Climatology* **33,** 2520–2541 (2013).

73. King, D. L., Kratochvil, J. A. & Boyson, W. E. *Photovoltaic Array Performance Model* (United States. Department of Energy, 2004).

74. Kjellström, E. *et al.* European climate change at global mean temperature increases of 1.5 and 2 C above pre-industrial conditions as simulated by the EURO-CORDEX regional climate models. *Earth System Dynamics* **9,** 459–478 (2018).

75. Knippertz, P., Ulbrich, U. & Speth, P. Changing cyclones and surface wind speeds over the North Atlantic and Europe in a transient GHG experiment. *Climate Research* **15,** 109–122 (2000).

76. Köberle, A. C., Gernaat, D. E. & van Vuuren, D. P. Assessing current and future techno-economic potential of concentrated solar power and photovoltaic electricity generation. *Energy* **89,** 739–756 (2015).

77. Krishnan, A. & Bhaskaran, P. K. Performance of CMIP5 wind speed from global climate models for the Bay of Bengal region. *International Journal of Climatology* **40,** 3398–3416 (2020).

78. Kushner, P. J. *et al.* Canadian snow and sea ice: assessment of snow, sea ice, and related climate processes in Canada's Earth system model and climate-prediction system. *The Cryosphere* **12,** 1137–1156 (2018).

79. Kvalevåg, M. M. & Myhre, G. Human impact on direct and diffuse solar radiation during the industrial era. *Journal of Climate* **20,** 4874–4883 (2007).

80. Lawrance, A. On conditional and partial correlation. *The American Statistician* **30,** 146–149 (1976).

81. Leung, A. C., Gough, W. A., Butler, K. A., Mohsin, T. & Hewer, M. J. Characterizing observed surface wind speed in the Hudson Bay and Labrador regions of Canada from an aviation perspective. *International Journal of Biometeorology,* 1–15 (2020).

82. Lynch, A. H., Curry, J. A., Brunner, R. D. & Maslanik, J. A. Toward an integrated assessment of the impacts of extreme wind events on Barrow, Alaska. *Bulletin of the American Meteorological Society* **85,** 209–222 (2004).

83. Mankin, J. S., Lehner, F., Coats, S. & McKinnon, K. A. The value of initial condition large ensembles to robust adaptation decision-making. *Earth's Future* **8,** e2012EF001610 (2020).

84. Manwell, J. F., McGowan, J. G. & Rogers, A. L. *Wind Energy Explained: Theory, Design and Application* (John Wiley & Sons, 2002).

85. Masui, T. *et al.* An emission pathway for stabilization at 6 Wm^{-2} radiative forcing. *Climatic Change* **109,** 59–76 (2011).

86. Mavromatakis, F., Kavoussanaki, E., Vignola, F. & Franghiadakis, Y. Measuring and estimating the temperature of photovoltaic modules. *Solar Energy* **110,** 656–666 (2014).

87. Mavromatakis, F. *et al.* Modeling the photovoltaic potential of a site. *Renewable Energy* **35,** 1387–1390 (2010).

88. McInnes, K. L., Erwin, T. A. & Bathols, J. M. Global Climate Model projected changes in 10 m wind speed and direction due to anthropogenic climate change. *Atmospheric Science Letters* **12,** 325–333 (2011).

89. McVicar, T. R. *et al.* Global review and synthesis of trends in observed terrestrial near-surface wind speeds: Implications for evaporation. *Journal of Hydrology* **416,** 182–205 (2012).

90. Miao, H. *et al.* Evaluation of Northern Hemisphere surface wind speed and wind power density in multiple reanalysis datasets. *Energy* **200,** 117382 (2020).

91. Mioduszewski, J., Vavrus, S. & Wang, M. Diminishing Arctic sea ice promotes stronger surface winds. *Journal of Climate* **31,** 8101–8119 (2018).

92. Nam, C., Bony, S., Dufresne, J.-L. & Chepfer, H. The 'too few, too bright'tropical low-cloud problem in CMIP5 models. *Geophysical Research Letters* **39** (2012).

93. Natural Resources Canada. *Glencore RAGLAN Mine Renewable Electricity Smart-Grid Pilot Demonstration* www.nrcan.gc.ca/science-and-data/funding-partnerships/funding-opportunities/current-investments/glencore-raglan-mine-renewable-electricity-smart-grid-pilot-demonstration/16662 (2021).

94. O'Gorman, P. & Muller, C. J. How closely do changes in surface and column water vapor follow Clausius–Clapeyron scaling in climate change simulations? *Environmental Research Letters* **5,** 025207 (2010).

95. Optis, M., Monahan, A. & Bosveld, F. C. Moving beyond Monin–Obukhov similarity theory in modelling wind-speed profiles in the lower atmospheric boundary layer under stable stratification. *Boundary-layer Meteorology* **153,** 497–514 (2014).

96. Overland, J. E. Atmospheric boundary layer structure and drag coefficients over sea ice. *Journal of Geophysical Research: Oceans* **90,** 9029–9049 (1985).

97. Overland, J. E. & Wang, M. Large-scale atmospheric circulation changes are associated with the recent loss of Arctic sea ice. *Tellus, Series A: Dynamic Meteorology and Oceanography* **62,** 1–9. ISSN: 02806495 (2010).

98. Pérez, J. C., González, A., Dıaz, J. P., Expósito, F. J. & Felipe, J. Climate change impact on future photovoltaic resource potential in an orographically complex archipelago, the Canary Islands. *Renewable Energy* **133,** 749–759 (2019).

99. Pinard, J.-P. Wind climate of the Whitehorse area. *Arctic,* 227–237 (2007).

100. Pryor, S. & Barthelmie, R. Assessing climate change impacts on the near-term stability of the wind energy resource over the United States. *Proceedings of the National Academy of Sciences* **108,** 8167–8171 (2011).

101. Pryor, S. & Barthelmie, R. Assessing the vulnerability of wind energy to climate change and extreme events. *Climatic Change* **121,** 79–91 (2013).

102. Pryor, S., Barthelmie, R. & Kjellström, E. Potential climate change impact on wind energy resources in northern Europe: analyses using a regional climate model. *Climate Dynamics* **25,** 815–835 (2005).

103. Pryor, S. *et al.* Wind speed trends over the contiguous United States. *Journal of Geophysical Research: Atmospheres* **114** (2009).

104. Qian, H. & Zhang, R. Future changes in wind energy resource over the Northwest Passage based on the CMIP6 climate projections. *International Journal of Energy Research* **45,** 920–937 (2021).

105. Quitoras, M. R., Campana, P. E. & Crawford, C. Exploring electricity generation alternatives for Canadian Arctic communities using a multi-objective genetic algorithm approach. *Energy Conversion and Management* **210,** 112471 (2020).

106. Ravestein, P., Van der Schrier, G., Haarsma, R., Scheele, R. & Van den Broek, M. Vulnerability of European intermittent renewable energy supply to climate change and climate variability. *Renewable and Sustainable Energy Reviews* **97,** 497–508 (2018).

107. Redilla, K., Pearl, S., Bieniek, P. & Walsh, J. Wind climatology for Alaska: historical and future. *Atmospheric and Climate Sciences* **9,** 683–702 (2019).

108. Remund, J. & Müller, S. C. *Trends in global radiation between 1950 and 2100* in *10th EMS Annual Meeting, 10th European Conference on Applications of Meteorology (ECAM). European Meteorological Society (EMS), Zurich* (2010).

109. Romanou, A. *et al.* 20th century changes in surface solar irradiance in simulations and observations. *Geophysical Research Letters* **34** (2007).

110. Sanford, T., Frumhoff, P. C., Luers, A. & Gulledge, J. The climate policy narrative for a dangerously warming world. *Nature Climate Change* **4,** 164–166 (2014).

111. Schwalm, C. R., Glendon, S. & Duffy, P. B. RCP8. 5 tracks cumulative CO2 emissions. *Proceedings of the National Academy of Sciences* **117,** 19656–19657 (2020).

112. Scinocca, J. *et al.* Coordinated global and regional climate modeling. *Journal of Climate* **29,** 17–35 (2016).

113. Screen, J. A., Simmonds, I. & Keay, K. Dramatic interannual changes of perennial Arctic sea ice linked to abnormal summer storm activity. *Journal of Geophysical Research: Atmospheres* **116** (2011).

114. Sepp, M. & Jaagus, J. Changes in the activity and tracks of Arctic cyclones. *Climatic Change* **105,** 577–595. ISSN: 01650009 (2011).

115. Serreze, M. C. *Arctic and Antarctic: Arctic Climate* Second Edi, 107–115. ISBN: 9780123822260. http://dx.doi.org/10.1016/B978-0-12-382225-3.00072-4 (Elsevier, 2015).

116. Serreze, M. C. & Barry, R. G. *The Arctic Climate System* (Cambridge University Press, 2014).

117. Shaw, T. *et al.* Storm track processes and the opposing influences of climate change. *Nature Geoscience* **9,** 656–664 (2016).

118. Skoplaki, E. & Palyvos, J. A. On the temperature dependence of photovoltaic module electrical performance: A review of efficiency/power correlations. *Solar Energy* **83,** 614–624 (2009).

119. Smits, A., Klein Tank, A. & Können, G. Trends in storminess over the Netherlands, 1962–2002. *International Journal of Climatology: A Journal of the Royal Meteorological Society* **25,** 1331–1344 (2005).

120. Solaun, K. & Cerdá, E. Climate change impacts on renewable energy generation. A review of quantitative projections. *Renewable and Sustainable Energy Reviews* **116,** 109415 (2019).

121. St. George, S. & Wolfe, S. A. El Niño stills winter winds across the southern Canadian Prairies. *Geophysical Research Letters* **36** (2009).

122. Stanfield, R. E. *et al.* Assessment of NASA GISS CMIP5 and post-CMIP5 simulated clouds and TOA radiation budgets using satellite observations. Part I: Cloud fraction and properties. *Journal of Climate* **27,** 4189–4208 (2014).

123. Stanhill, G. Solar irradiance, air pollution and temperature changes in the Arctic. *Philosophical Transactions of the Royal Society of London. Series A: Physical and Engineering Sciences* **352,** 247–258 (1995).

124. Stanhill, G. & Cohen, S. Global dimming: a review of the evidence for a widespread and significant reduction in global radiation with discussion of its probable causes and possible agricultural consequences. *Agricultural and Forest Meteorology* **107,** 255–278 (2001).

125. Stroeve, J. C. *et al.* Trends in Arctic sea ice extent from CMIP5, CMIP3 and observations. *Geophysical Research Letters* **39** (2012).

126. Sun, S. & Verseghy, D. Introducing water-stressed shrubland into the Canadian Land Surface Scheme. *Journal of Hydrology* **579,** 124157 (2019).

127. TamizhMani, G., Ji, L., Tang, Y., Petacci, L. & Osterwald, C. *Photovoltaic module thermal/wind performance: long-term monitoring and model development for energy rating* in *NCPV and Solar Program Review Meeting Proceedings, 24-26 March 2003, Denver, Colorado (CD-ROM)* (2003).

128. Tian, Q., Huang, G., Hu, K. & Niyogi, D. Observed and global climate model based changes in wind power potential over the Northern Hemisphere during 1979–2016. *Energy* **167,** 1224–1235 (2019).

129. Tobin, I. *et al.* Assessing climate change impacts on European wind energy from ENSEMBLES high-resolution climate projections. *Climatic Change* **128,** 99–112 (2015).

130. Torralba, V., Doblas-Reyes, F. J. & Gonzalez-Reviriego, N. Uncertainty in recent near-surface wind speed trends: a global reanalysis intercomparison. *Environmental Research Letters* **12,** 114019 (2017).

131. Trenberth, K. E. & Fasullo, J. T. Global warming due to increasing absorbed solar radiation. *Geophysical Research Letters* **36** (2009).

132. Tuller, S. E. Measured wind speed trends on the west coast of Canada. *International Journal of Climatology: A Journal of the Royal Meteorological Society* **24,** 1359–1374 (2004).

133. Van der Wiel, K. *et al.* Meteorological conditions leading to extreme low variable renewable energy production and extreme high energy shortfall. *Renewable and Sustainable Energy Reviews* **111,** 261–275 (2019).

134. Van Vuuren, D. P. *et al.* The representative concentration pathways: an overview. *Climatic Change* **109,** 5–31 (2011).

135. Vautard, R., Cattiaux, J., Yiou, P., Thépaut, J.-N. & Ciais, P. Northern Hemisphere atmospheric stilling partly attributed to an increase in surface roughness. *Nature Geoscience* **3,** 756–761 (2010).

136. Verseghy, D. *The Canadian Land Surface Scheme (Version 3.4), Technical Documentation (Version 1.1)* tech. rep. January (Environment Canada, 2009), 180.

137. Verseghy, D. L. The Canadian land surface scheme (CLASS): its history and future. *Atmosphere-Ocean* **38,** 1–13 (2000).

138. Vial, J., Dufresne, J.-L. & Bony, S. On the interpretation of inter-model spread in CMIP5 climate sensitivity estimates. *Climate Dynamics* **41,** 3339–3362 (2013).

139. Von Salzen, K. *et al.* The Canadian fourth generation atmospheric global climate model (CanAM4). Part I: representation of physical processes. *Atmosphere-Ocean* **51,** 104–125 (2013).

140. Wan, H., Wang, X. L. & Swail, V. R. Homogenization and trend analysis of Canadian near-surface wind speeds. *Journal of Climate* **23,** 1209–1225 (2010).

141. WASA Group. Changing waves and storms in the Northeast Atlantic? *Bulletin of the American Meteorological Society* **79,** 741–760 (1998).

142. Weisse, R., Von Storch, H. & Feser, F. Northeast Atlantic and North Sea storminess as simulated by a regional climate model during 1958–2001 and comparison with observations. *Journal of Climate* **18,** 465–479 (2005).

143. Wendler, G., Eaton, F. D. & Ohtake, T. Multiple reflection effects on irradiance in the presence of Arctic stratus clouds. *Journal of Geophysical Research: Oceans* **86,** 2049–2057 (1981).

144. Westervelt, D., Horowitz, L., Naik, V., Golaz, J.-C. & Mauzerall, D. Radiative forcing and climate response to projected 21st century aerosol decreases. *Atmospheric Chemistry and Physics* **15,** 12681–12703 (2015).

145. Whan, K., Zwiers, F. & Sillmann, J. The influence of atmospheric blocking on extreme winter minimum temperatures in North America. *Journal of Climate* **29,** 4361–4381 (2016).

146. Wild, M. Decadal changes in radiative fluxes at land and ocean surfaces and their relevance for global warming. *Wiley Interdisciplinary Reviews: Climate Change* **7,** 91–107 (2016).

147. Wild, M. Global dimming and brightening: A review. *Journal of Geophysical Research: Atmospheres* **114** (2009).

148. Wild, M. Short-wave and long-wave surface radiation budgets in GCMs: a review based on the IPCC-AR4/CMIP3 models. *Tellus A: Dynamic Meteorology and Oceanography* **60,** 932–945 (2008).

149. Wild, M., Folini, D., Henschel, F., Fischer, N. & Müller, B. Projections of long-term changes in solar radiation based on CMIP5 climate models and their influence on energy yields of photovoltaic systems. *Solar Energy* **116,** 12–24 (2015).

150. Wild, M., Grieser, J. & Schär, C. Combined surface solar brightening and increasing greenhouse effect support recent intensification of the global land-based hydrological cycle. *Geophysical Research Letters* **35** (2008).

151. Wild, M. *et al.* From dimming to brightening: Decadal changes in solar radiation at Earth's surface. *Science* **308,** 847–850 (2005).

152. Wild, M. *et al.* The energy balance over land and oceans: an assessment based on direct observations and CMIP5 climate models. *Climate Dynamics* **44,** 3393–3429 (2015).

153. Yan, Z., Bate, S., Chandler, R., Isham, V. & Wheater, H. Changes in extreme wind speeds in NW Europe simulated by generalized linear models. *Theoretical and Applied Climatology* **83,** 121–137 (2006).

154. Yao, Y., Huang, G. H. & Lin, Q. Climate change impacts on Ontario wind power resource. *Environmental Systems Research* **1,** 1–11 (2012).

155. Zeng, Z. *et al.* A reversal in global terrestrial stilling and its implications for wind energy production. *Nature Climate Change* **9,** 979–985 (2019).

156. Zou, L. *et al.* Global surface solar radiation and photovoltaic power from Coupled Model Intercomparison Project Phase 5 climate models. *Journal of Cleaner Production* **224,** 304–324 (2019).

Appendix A: Summary of previous research

91

Table A.1: Summary of previous studies of projected 21st century change in near-surface wind speed (SWS) or wind power potential (*WPP*) in the study area. Use of Regional Climate Models (RCM) or Earth System Models (ESM) is indicated, as well as the reference period (ref. period) and projection period (proj. period) of stated results, if relevant. Geographical scope is listed in the table, but summarized relevant projections are generally specific to the study area.

Study	Scenario[a]	Scope	SWS/ *WPP*	RCM/ ESM	Model(s)	Ref. period	Proj. period	Relevant projections
Chen (2020)	RCP8.5	Contiguous US and southern Canada	SWS and *WPP*	RCM	12 NA-CORDEX models	1971-2000	2071-2100	MME mean predicts SWS change between -10% and 10%, and wind power density changes of between -20% and 20%, with decreases over the East Coast, western Canada and the USA, and increases over northern Ontario, Quebec, and Labrador. Northern increases are driven by DJF, MAM, and SON increases and offset by JJA decreases, although only DJF and JJA see high agreement between models in this region.
Daines *et al.* (2016)	SRES A2	Western Canada	SWS and *WPP*	RCM	CRCM driven by 2 ESMs (ECHAM5, CGCM)	2031-2060	1971-2000	ECHAM5-driven model: Modest decreases or no change in SWS and WPD. CGCM-driven model: Modest increases in SWS, large increases in WPD.

continued . . .

92

Table A.1 continued.

Study	Scenario[a]	Scope	SWS/ *WPP*	RCM/ ESM	Model(s)	Ref. period	Proj. period	Relevant projections
Gernaat *et al.* (2021)	RCP6.0	Global	SWS and *WPP* (technical potential)[b]	ESM	4 ISIMIP2b models	1970-2000	2070-2100	Non-significant decreases in SWS, from 0-5% for much of Canada, with increases only in the northern parts of the Canadian Arctic Archipelago (again excluding Baffin Island) and the Arctic Ocean. This change corresponds to non-significant projected decreases of about 0-10% in wind power potential, with greatest decreases projected for Nunavut, northern Quebec, and Labrador.
Jeong & Sushama (2019)	RCP4.5, RCP 8.5	North America	SWS	RCM	Limited area GEM model driven by CanESM2, MPI-ESM	1981-2010	2071-2100	RCP8.5: Mean wind speed increases up to 0.5 m/s in northern Canada for both driving ESMs. Decreases in summer (JJA) mean wind speeds for most of North America, excluding northern Canada.
Jung & Schindler (2019)	RCP8.5	Global	SWS	ESM	12 CMIP5 ESMs	2006-2019	2073-2099	Increases (<0.4 m/s) in mean wind speed for Hudson Bay and the northern part of the Canadian Arctic Archipelago, with some decreases in Eastern Canada, Baffin Island and southern Alberta and BC.

continued ...

93

Table A.1 continued.

Study	Scenario[a]	Scope	SWS/ *WPP*	RCM/ ESM	Model(s)	Ref. period	Proj. period	Relevant projections
Karnauskas *et al.* (2018)	RCP4.5, RCP8.5	Global	*WPP*	ESM	10 CMIP5 models	1980-2005	2080-2100	RCP8.5: Decrease in annual mean wind power by the end of the century over the central USA and Eastern Canada. Most of mainland Canada is projected to experience non-robust changes to annual mean power; increases are projected only for parts of the Canadian Arctic Archipelago, with the exception of Baffin Island.
McInnes *et al.* (2011)	SRES A1B	Global	SWS	ESM	19 CMIP3 models	1981-2000	2081-2100	Increases in mean (>10%) and 99th percentile annual and DJF wind speeds in a northwest-to-southeast band across central and northern Canada.
Mioduszewski *et al.* (2018)	RCP8.5	Arctic (north of 50°N)	SWS	ESM	CESM-LE	1971-2000	2071-2100	Increases for northern marine and coastal areas and far northern interior regions, especially those adjacent to Hudson Bay and parts of Nunavut. Arctic domain increases of up to 3 m/s projected.
Qian & Zhang (2021)	CP8.5	Part of Canadian Arctic Archipelago	*WPP*	ESM	7 models from CMIP6	1980-2014	2076-2100	RCP8.5: Wind energy density will increase in the region North of 72°N, but largely decrease to the south, with impacts as great as 30%.

continued ...

94

Table A.1 continued.

Study	Scenario[a]	Scope	SWS/ *WPP*	RCM/ ESM	Model(s)	Ref. period	Proj. period	Relevant projections
Redilla *et al.* (2019)	RCP8.5	Alaska, station-based	SWS	RCM	WRF driven by CM3, CCSM4	1980-2014	2065-2099	More significant wind speed changes for one driving ESM than the other, but both showed similar trends and seasonality in projected changes: increases in cold season wind speeds, and decreases in warm season wind speeds, with increases more common in northwestern and coastal locations, and decreases more common in southern and inland locations.
Yao *et al.* (2012)	SRES A2, SRES B2	Ontario	SWS	RCM	PRECIS driven by HadAM3P	1961-1990	2071-2100	SRES-A2: Mean wind speed decreases in southern Ontario of up to 5%, and increases of >5% for coastal areas off James and Hudson Bay.

[a] Comparing global temperature change and anthropogenic forcings between RCP and SRES scenarios, SRES A1FI is comparable to RCP 8.5, SRES A1B to RCP 6.0, and SRES B1 to RCP 4.5. SRES A2 falls between RCP6.0 and RCP8.5, but RCP8.5 was based on SRES A2 (Van Vuuren *et al.* 2011).

[b] Technical potential accounts for land-use and system performance constraints. ISIMIP2b includes land-use change related to agricultural management (Frieler *et al.* 2017).

Table A.2: Summary of previous studies of projected 21st century change in surface downwelling solar radiation (DSR) or solar power potential (*SPP*) in the study area. Use of Regional Climate Models (RCM) or Earth System Models (ESM) is indicated, as well as the reference period (ref. period) and projection period (proj. period) of stated results, if relevant. Geographical scope is listed in the table, but summarized relevant projections are generally specific to the study area.

Study	Scenario[a]	Scope	DSR/ *SPP*	RCM/ ESM	Model(s)	Ref. period	Proj. period	Relevant projections
Crook *et al.* (2011)	SRES A1B	Global	*SPP*	ESM	HadGEM1 and HadCM3 (CMIP3)			Decreases of about 10% in PV output in high latitude regions from 2010 to 2080, including northern Canada.
Feron *et al.* (2021)	RCP4.5	Global	*SPP*	ESM	7 CMIP5 models	1961-1990	2036-2065	Decreases in MME mean of about 5% in PV potential in northern Canada, which largely coincides with increases in cloud fraction and decrease in aerosol optical depth in this region.
Gernaat *et al.* (2021)	RCP6.0	Global	DSR, *SPP* tech. pot.[b]	ESM	4 ISIMIP2b models	1971-2000	2071-2100	Significant decreases in solar irradiance over Arctic Canada (mainly the Canadian Arctic Archipelago), with moderate increases in southern regions of Canada. This corresponds to significant decreases in PV and concentrated solar power technical potential in these northern regions, and non-significant changes elsewhere.

continued ...

96

Table A.2 continued.

Study	Scenario[a]	Scope	DSR/ SPP	RCM/ ESM	Model(s)	Ref. period	Proj. period	Relevant projections
Haywood *et al.* (2011)	RCP8.5	Global	DSR	ESM	HadGEM2-ES	2000	2090	Large decreases in cloud-free DSR, with a global average of approximately 5.7 W/m^2, attributed largely to increases in atmospheric water vapour, which is offset by decreases in aerosols. Trends in all-sky DSR over most areas are minimal, as decreases in cloud cover offset the cloud-free DSR dimming.
Huber *et al.* (2016)	SRES A1B	Global	DSR	ESM	E39C-A and ECHAM5-HAM	1995-1999	2035-2039	Decreases in northern Canada averaging almost 5 W/m^2 (about 2%), coinciding with increasing cloud cover over most of the region, as well as increases (decreases) in aerosol optical depth over northern (southern) Canada.
Remund & Müller (2010)	SRES A2	Global	DSR	ESM	18 models	1961-1990	2080-2099	Small decreases in DSR over most of globe, with some regions of brightening (e.g., Mediterranean).

continued ...

97

Table A.2 continued.

Study	Scenario[a]	Scope	DSR/ SPP	RCM/ ESM	Model(s)	Ref. period	Proj. period	Relevant projections
Wild *et al.* (2015a)	RCP8.5	Global	DSR and *SPP*	ESM	39 CMIP5 models	2006-2015	Trends until 2050	Dimming in most parts of the globe, corresponding to significant negative trends in estimated PV power output in northern Canada, with little or no change in southern Canada. The multi-model median projects significant increases in cloud cover over polar areas and some parts of northern Canada, associated with significant decreasing trends in all-sky radiation over much of Canada. Clear-sky radiation changes are much smaller, close to zero or slightly negative across the globe.
Zou *et al.* (2019)	RCP8.5	Global	*SPP*	ESM	36 CMIP5 models			Worldwide average decrease of 0.67 kWh/m^2/year during 2006 to 2100. Stronger decreasing trends found in high latitudes, including most of northern Canada, coinciding with increases in cloud cover in these regions.

[a] Comparing global temperature change and anthropogenic forcings between RCP and SRES scenarios, SRES A1FI is comparable to RCP 8.5, SRES A1B to RCP 6.0, and SRES B1 to RCP 4.5. SRES A2 falls between RCP6.0 and RCP8.5, but RCP8.5 was based on SRES A2 (Van Vuuren *et al.* 2011).

[b] Technical potential accounts for land-use and system performance constraints. ISIMIP2b includes land-use change related to agricultural management (Frieler *et al.* 2017).

Appendix B: Determining friction velocity and roughness length from CanRCM4 output

Instantaneous roughness length (z_0) and friction velocity (u_*) are not available as part of CanRCM4 output. Friction velocity can be calculated using eastward and northward downward wind stress (τ_0), which is only available on a 6-hourly basis, unlike most other parameters (1- or 3-hourly). Wind stress is related to u_* by:

$$u_* = (\tau_0/\rho)^{1/2} \tag{B.1}$$

One of these two unknown parameters (friction velocity or roughness length) can be calculated at a 3-hourly basis from Equations 3.2 and 3.11, if the other parameter is known. Three methods of determining these two parameters were explored:

1. Assuming a temporally static roughness length, calculate friction velocity from 6-hourly wind stress using Equation (B.1), up-sample friction velocity to 3-hourly. Hereafter, the friction velocity calculated from CanRCM4 wind stress output will be referred to as $u_{*,RCM}$.

2. Assuming a temporally static roughness length, calculate friction velocity from Equation (3.2) at each time step using the iterative function *scipy.optimize.fsolve* from Scipy 1.5.1 in Python 3.8.3. The *fsolve* function returns roots of equations defined by $f(x) = 0$, and was given the starting estimate $u_{*,RCM}$. Hereafter, the friction velocity determined via this method will be referred to as $u_{*,sol}$.

3. Adjust Method 1 by solving for roughness length (hereafter $z_{0,sol}$) at each time step using Equation (3.2) and $u_{*,RCM}$. This temporally varying z_0 can be interpreted as a correction factor reflecting the complex physical processes which are not reproducible due to averaging in model output.

Method 1 has the advantage of being substantially less computationally intensive than Method 2. However, Method 2 provides a more accurate estimate of u_*, as model output is available at 3-hr versus 6-hr timescales, and should theoretically result in a value of $v_{10,u*,sol}$ identical to model output near-surface winds ($v_{10,model}$). However, Method 2 it is not solvable at all time points (i.e., no real roots are found). In the period of 1970 to 1999, a solution was found 86 to 95% of the time for the communities of focus. Where no solution is found, $u_{*,sol}$ is set to $u_{*,RCM}$. However, wind stress based $u_{*,RCM}$ and solved $u_{*,sol}$ differ substantially, as shown in Figure B.1, resulting in large differences in estimated 10 m wind speeds and $v_{10,model}$.

Method 3 is less computationally intensive and, as with Method 2, should also result in identical calculations of 10 m wind speeds ($v_{10,z0,sol}$) and $v_{10,model}$. However, $z_{0,sol}$ estimates

were widely distributed, to be expected given the inconsistencies between $u_{*,RCM}$ and $u_{*,sol}$ (Figure B.1). A realistic $z_{0,sol}$ parameter (< 10 m) was found almost 99% of the time. In the approximately 1% of cases in which a physically unrealistic $z_{0,sol}$ was found (i.e. z_0 >10 m), $z_{0,sol}$ was calculated using linear interpolation. It is worth noting that locations with larger average $z_{0,sol}$ have on average a lower proportion of $u_{*,sol}$ found.

To assess Methods 1 to 3, $u_{*,RCM}$, $u_{*,sol}$ and $z_{0,sol}$ were input into Equation (3.2), as appropriate, to calculate 10 m wind speeds ($v_{10,u*,RCM}$, $v_{10,u*,sol}$, $v_{10,z0,sol}$, respectively). Figure B.2 (column 1) shows overlaid histograms of calculated and model output 10 m winds for the focal communities, demonstrating substantial variation in the distribution of v_{10}. Median $v_{10,model}$ was significantly different from $v_{10,other}$ for all Methods and locations (p <0.01, df=98), however, the median difference is typically, although not always, greatest for $v_{10,u*,RCM}$ and considerably lower for $v_{10,z0,sol}$ (Table B.1). Method 3 showed minimum error, with the difference in means least among the three Methods by a factor of at least 10.

A test case of extrapolated wind speed to 35 and 50 m hub heights was completed for the three methods. The considerable differences are carried forward to the 35 and 50 m heights, as can be discerned in Figure B.2 (columns 2 and 3). However, in cases where $v_{u*,sol}$ is found there is great consistency between hub height $v_{u*,sol}$ and $v_{z0,sol}$ for most locations. Histograms of filtered 50 m wind speeds demonstrate very high agreement between the two methods for all locations except Iqaluit and Iqaluit Coastal Location (Figure B.4). Looking at the box plots in Figure B.5, it is evident that these locations with high discrepancy in wind speeds aloft also have the largest and most variable results for $z_{0,sol}$, related to larger differences between $u_{*,RCM}$ and $u_{*,sol}$ (Figure B.1). In Iqaluit and Iqaluit Coastal Location in 1970-1999, the mean of the absolute difference between $u_{*,RCM}$ and $u_{*,sol}$ is ∼0.15 m/s, while the average for other locations ranges from 0.04 to 0.09 m/s. These large differences in $u_{*,sol}$ compared to $u_{*,RCM}$ will result in under- or over-estimation of $v_{u*,sol}$ winds aloft compared to $v_{z0,sol}$.

Two methods for reducing error in $u_{*,RCM}$ and $u_{*,sol}$ were explored:

a. Use effective velocity (v_{eff}) instead of $v_{10,model}$ when solving for u_* in Method 2. v_{eff} takes into account the contributions of free convection and deep convection to gustiness, and modifies wind speed by:

$$v_{eff} = \sqrt{v^2 + v_1^2 + v_2^2} \tag{B.2}$$

where $v_1 = \beta w_*$ and $v_2 = log(1 + 6.69P_c - 0.47P_c^2)$. P_c is convective precipitation in cm/day, β is 0.55 and w_* is the free-convection velocity scale, given by:

$$w_* = \left(\frac{g}{T}\overline{w'\theta'_s}z_i\right)^{1/3} \tag{B.3}$$

where $\overline{w'\theta'_s}$ is the kinematic surface heat flux and z_i is the boundary layer depth. z_i model output is only available on a 6-hr basis as a time point (not time mean).

b. Using displacement height, d, to account for impact of obstacles such as trees. And modifying Equation (3.2) according to:

$$v(z) = \frac{u_*}{k}\left[ln\left(\frac{z-d}{z_0}\right) - \Psi\left(\frac{z}{L}\right)\right] \tag{B.4}$$

In CanRCM4, displacement height is related to z_0 by $d = 7 * z_0$ (Verseghy 2009).

Exploration of adjustments (a) and (b) above to had no appreciable difference; there remained considerable inconsistencies between $u_{*,RCM}$ and $u_{*,sol}$ and therefore $v_{10,u*,RCM}$ and $v_{10,u*,sol}$.

In summary, due to the ease of computing and consistency of 10 m wind speeds, Method 3 was selected. Overall, there is high agreement of $v_{z0,sol}$ near-surface winds with model output. There is also high agreement between $v_{u*,sol}$ and $v_{z0,sol}$ winds aloft for most locations. Expected discrepancies in these wind speeds occur when the difference between $u_{*,RCM}$ and $u_{*,sol}$ is large, which happens in some locations (e.g., Iqaluit and Iqaluit Coastal Location) more than others. We conclude that error associated with the use of $z_{0,sol}$ in combination with $u_{*,RCM}$ (Method 3) is lower than the other two methods considered. Potential errors in the wind speeds aloft due to this method should not affect study results, as the focus is on quantifying variability in power production over time, and any errors will be consistently applied.

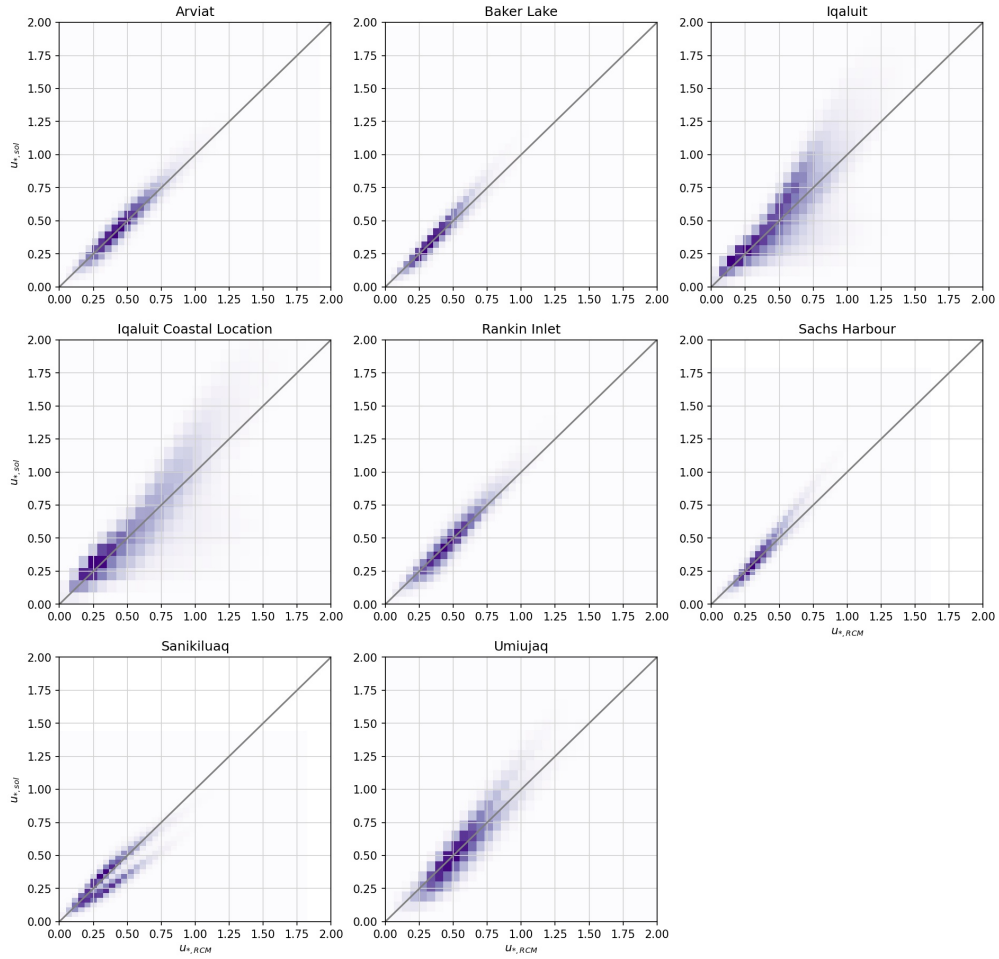

Figure B.1: Two-dimensional histograms of $u_{*,RCM}$ versus $u_{*,sol}$ for all 50 realizations, 1970 to 1999. Information was filtered to include only those time points at which $u_{*,sol}$ was found.

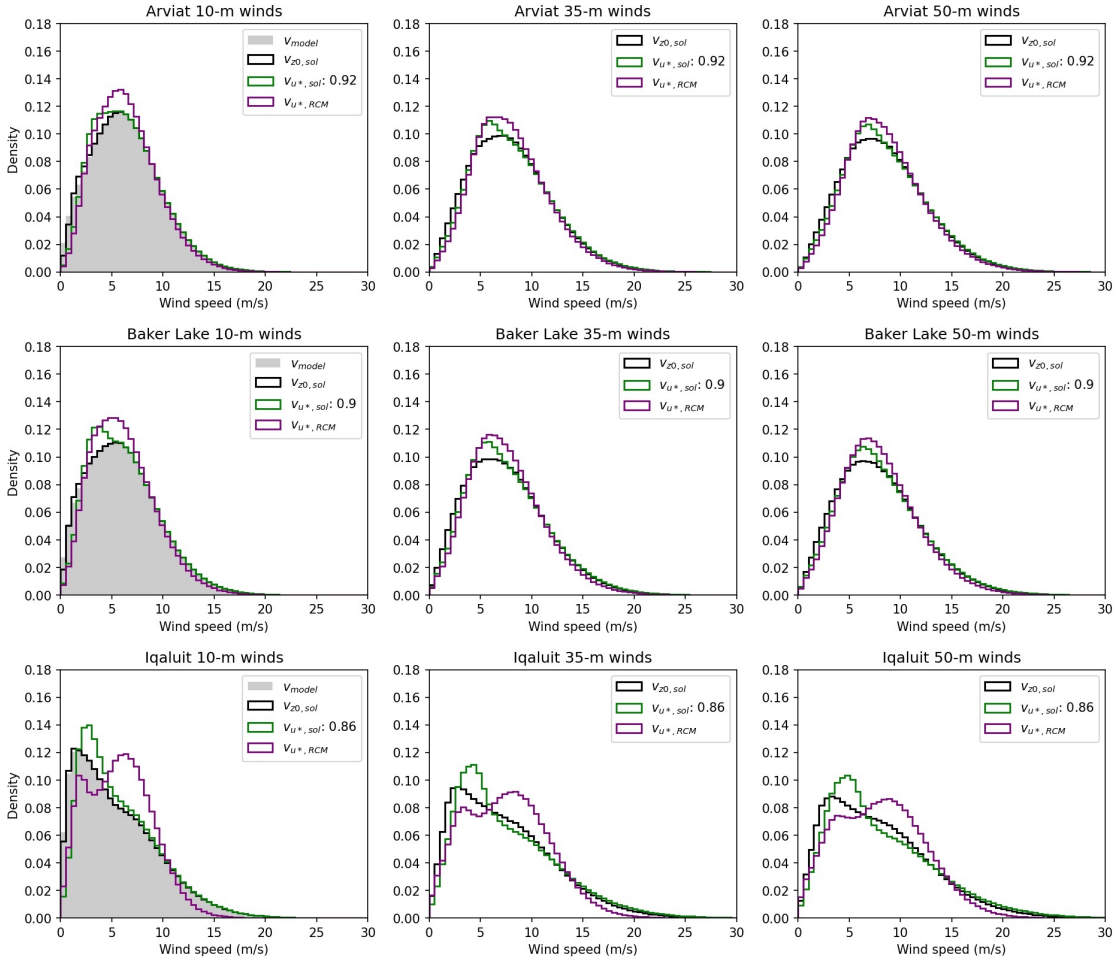

Figure B.2: Overlaid histograms of $v_{u*,RCM}$ (purple), $v_{u*,sol}$ (green), $v_{z0,sol}$ (black), and v_{model} (grey) at 10, 35, and 50 m heights (columns 1 to 3, respectively). v_{model} is only available for the 10 m height. Each row represents a different focal community, as indicated. Data from all 50 realizations from 1970 to 1999. See Figure B.3 below for the remaining locations.

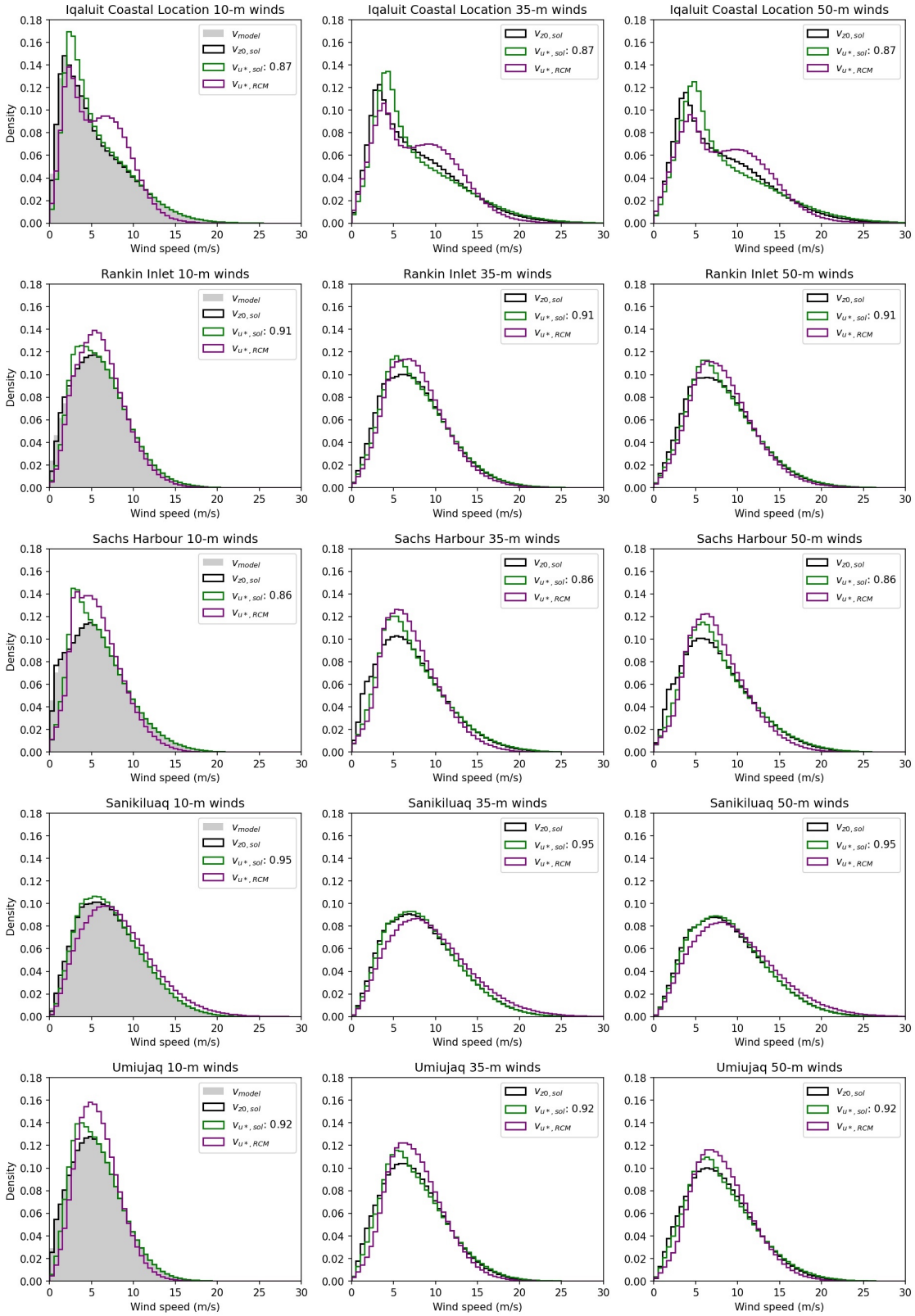

Figure B.3: Figure B.2 continued.

Table B.1: 50-realization mean of median 1970-1999 model output 10 m wind speed (column 2), as well as the mean difference ($v_{10,model}$ minus $v_{10,other}$) for the 3 methods (column 3 to 5). All values m/s; all differences are significant (p <0.001, df=98).

Location	Median $v_{10,model}$	$\Delta v_{10,z0,sol}$	$\Delta v_{10,u*,sol}$	$\Delta v_{10,u*,RCM}$
Arviat	6.119	0.000	0.001	-0.014
Baker Lake	5.803	0.000	0.001	-0.034
Iqaluit	4.811	0.000	0.219	0.909
Iqaluit Coastal Location	4.425	0.000	0.156	0.984
Rankin Inlet	5.701	0.000	0.002	0.111
Sachs Harbour	5.398	0.000	0.001	-0.012
Sanikiluaq	6.845	0.000	0.046	0.827
Umiujaq	5.333	0.000	0.004	0.187

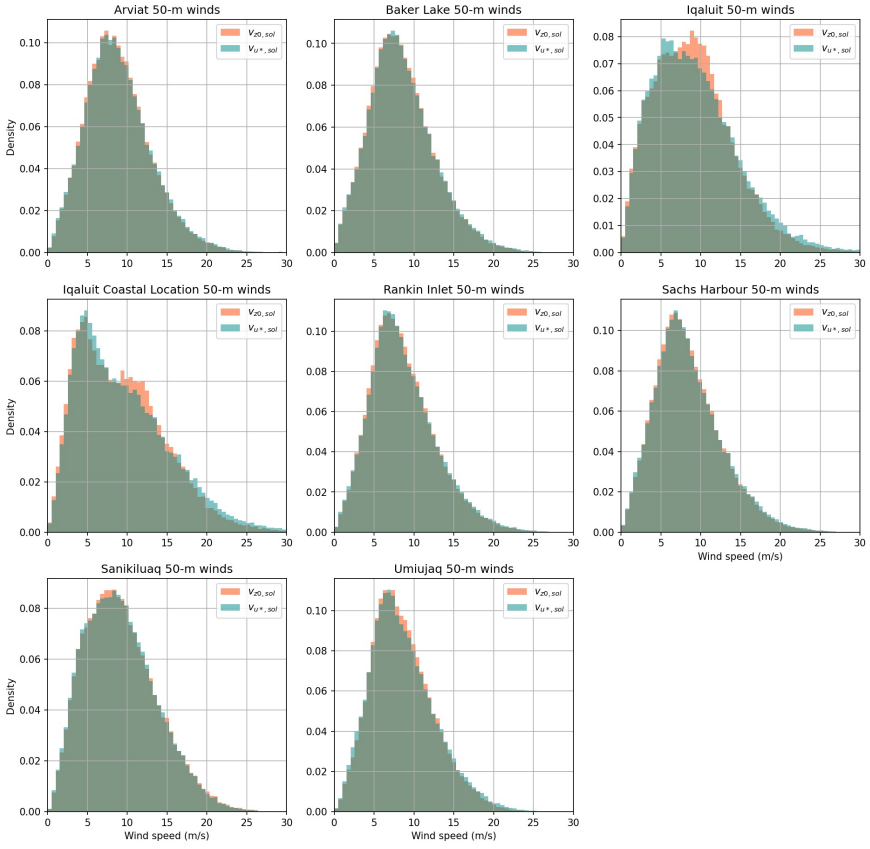

Figure B.4: Overlaid histogram of $v_{50,u*,RCM}$ versus $v_{50,z0,sol}$ for all 50 realizations, 1970 to 1999. Information was filtered to include only those time points at which $u_{*,sol}$ was found.

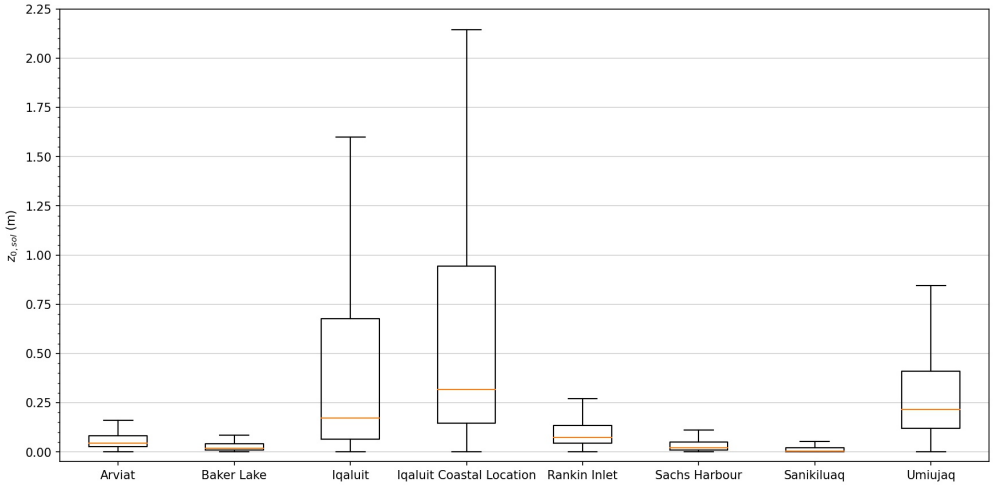

Figure B.5: Box plots of $z_{0,sol}$ for all 50 realizations, 1970-1999, after linear interpolation was applied. Outliers have been excluded for clarity, but $z_{0,sol}$ ranges up to 10 m for all locations.

Appendix C: Supplementary material

C.1 Wind power potential: Supplementary material

Table C.1: Inter-annual and inter-daily variability (as measured through coefficient of variation WPP_{day}, see Section 3.8) in the reference period (1970-1999) by the end of the 21st century (2070-2099), showing the ensemble mean with the ensemble minimum and maximum in brackets.

	IAV 1970-1999	IAV 2070-2099	IDV 1970-1999	IDV 2070-2099
	mean (min, max)	mean (min, max)	mean (min, max)	mean (min, max)
Arviat	0.05 (0.03, 0.06)	0.05 (0.03, 0.07)	0.70 (0.69, 0.72)	0.67 (0.65, 0.68)
Baker Lake	0.06 (0.04, 0.07)	0.06 (0.04, 0.08)	0.72 (0.71, 0.74)	0.71 (0.69, 0.73)
Iqaluit	0.07 (0.05, 0.09)	0.06 (0.04, 0.09)	0.82 (0.80, 0.84)	0.76 (0.75, 0.78)
Iqaluit CL	0.07 (0.04, 0.09)	0.06 (0.04, 0.08)	0.83 (0.81, 0.84)	0.76 (0.75, 0.78)
Rankin Inlet	0.05 (0.04, 0.06)	0.05 (0.04, 0.07)	0.65 (0.63, 0.67)	0.631 (0.62, 0.65)
Sachs Harbour	0.08 (0.05, 0.11)	0.06 (0.05, 0.08)	0.82 (0.81, 0.84)	0.77 (0.75, 0.79)
Sanikiluaq	0.05 (0.04, 0.06)	0.04 (0.03, 0.05)	0.64 (0.62, 0.65)	0.57 (0.55, 0.58)
Umiujaq	0.05 (0.04, 0.06)	0.05 (0.04, 0.06)	0.72 (0.71, 0.74)	0.67 (0.66, 0.69)

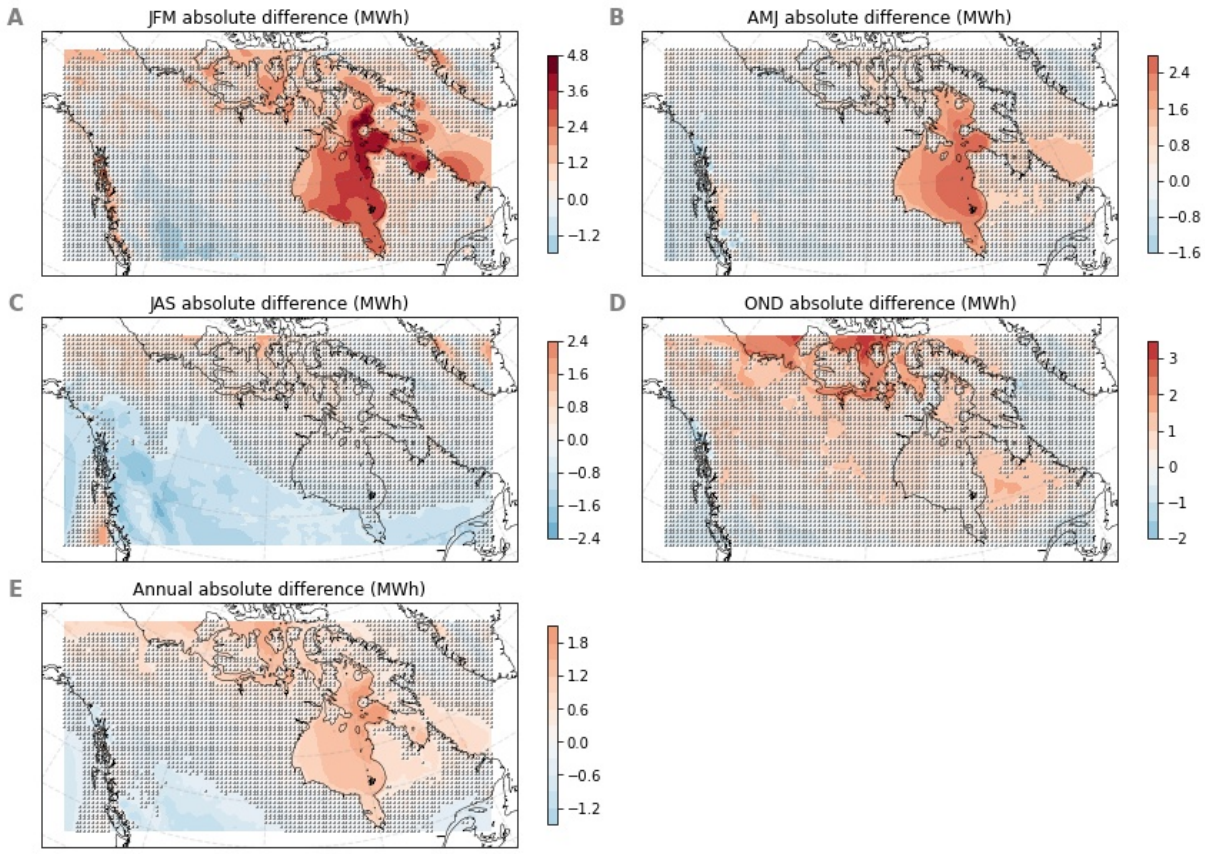

Figure C.1: Ensemble mean change in daily wind power potential (WPP_{day}; MWh) by 2070-2099 from the reference period (1970-1999), by season. Individual plot colourbars display the range of values for that plot, but colours are comparable between plots. Non-substantial changes are masked with hatching.

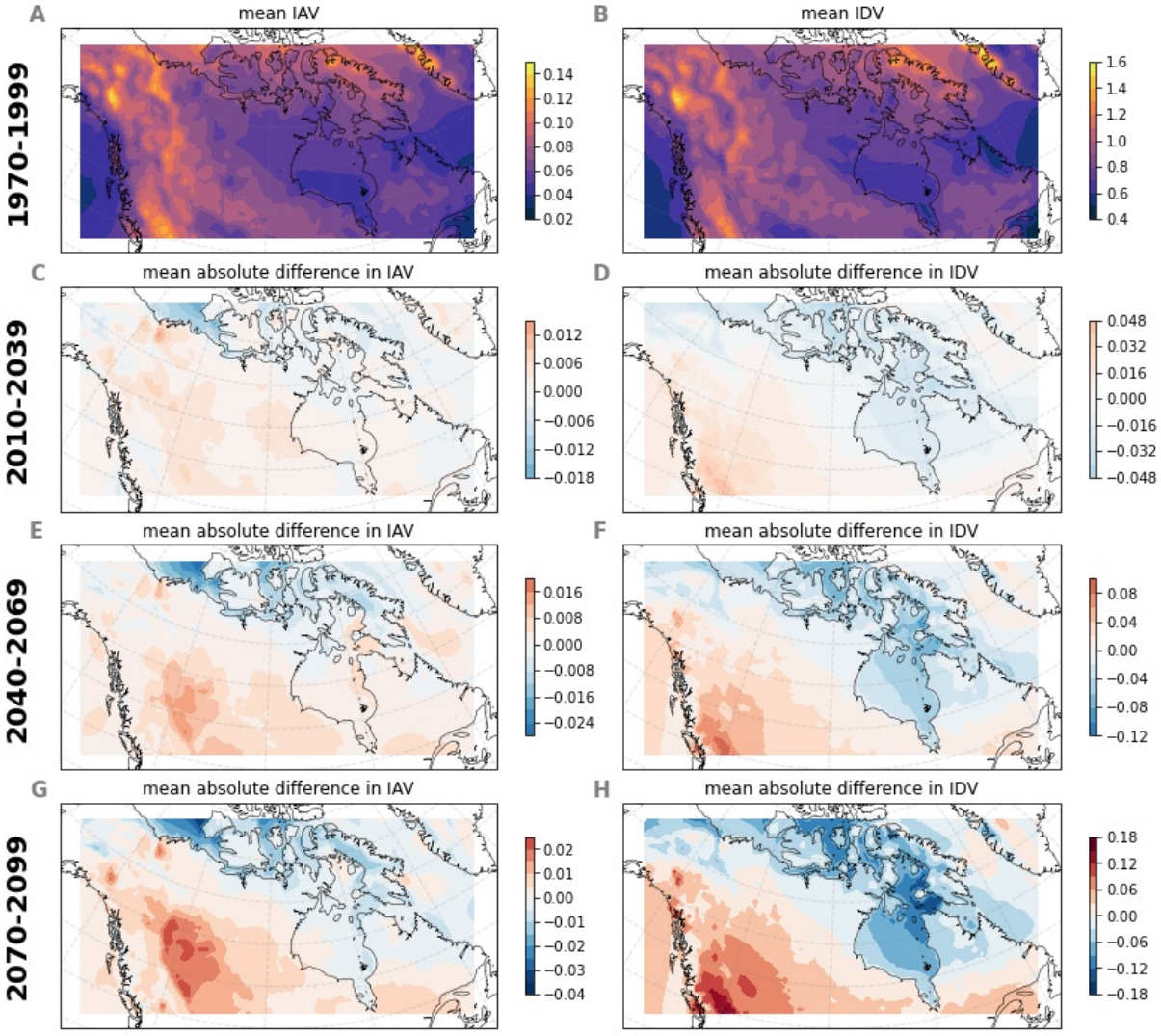

Figure C.2: Daily wind power potential inter-annual variability (column 1) and inter-daily variability (column 2) for the reference period (1970-1999, row 1, dimensionless) and ensemble mean change for the periods 2010-2039, 2040-2069, and 2070-2099 (rows 2 to 4, dimensionless). Individual plot colourbars display the range of values for that plot, scaled so that colours are comparable between plots of IAV change (C, E, and G) and IDV change (D, F, and H).

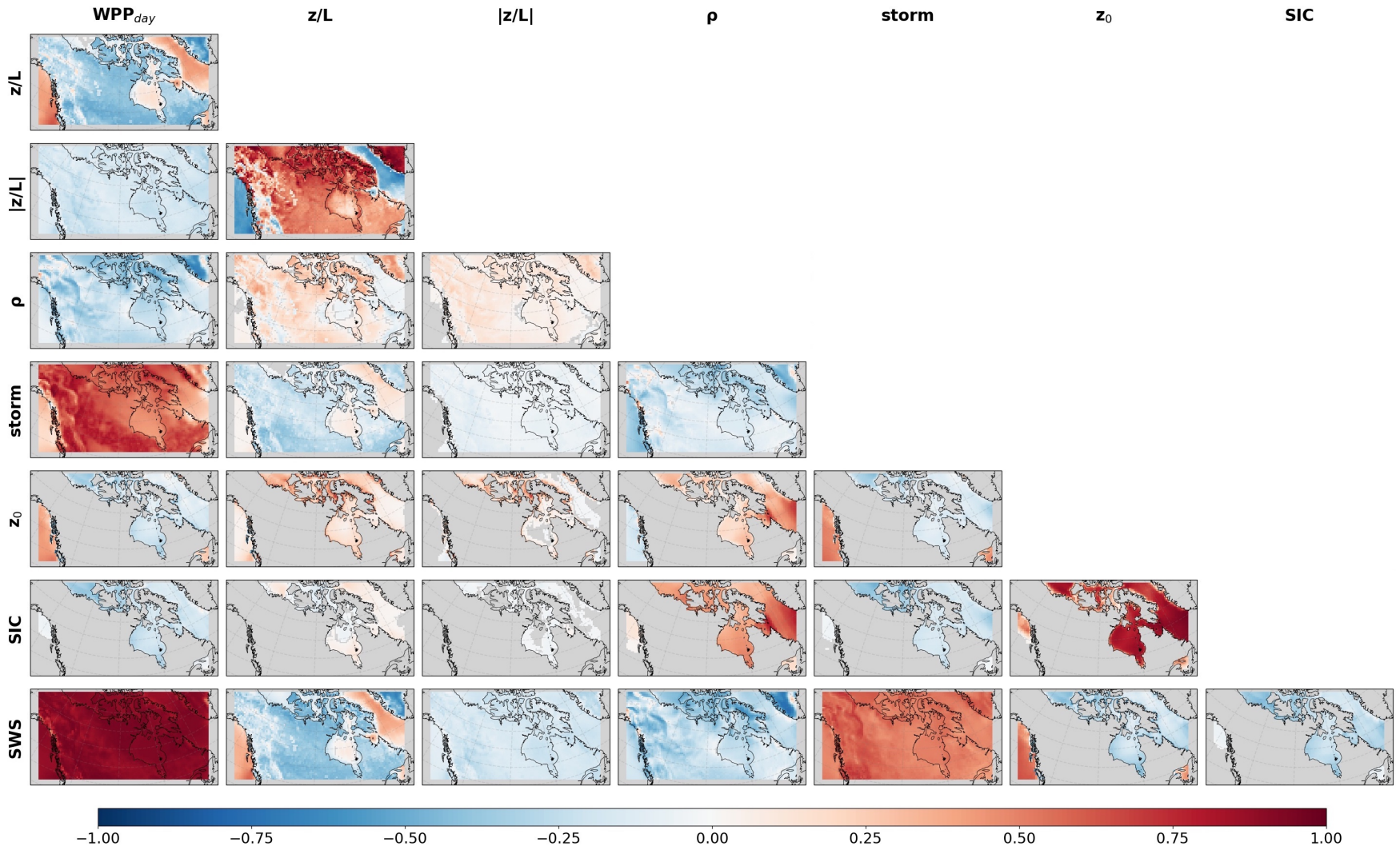

Figure C.3: Correlation matrix for the variables: daily wind power (WPP_{day}); monthly median surface layer stability (z/L); absolute surface layer stability ($|z/L|$); air density (ρ); storminess (percentage of time classified as storm); roughness length (z_0); sea ice concentration (SIC); and near-surface wind speed (SWS). Land areas for SIC and z_0 as well as non-significant (p>0.05) correlations have been masked out with grey. Correlations are taken across all ensemble members using detrended, deseasonalized 1970-1999 monthly statistics at described in Table 4.2.

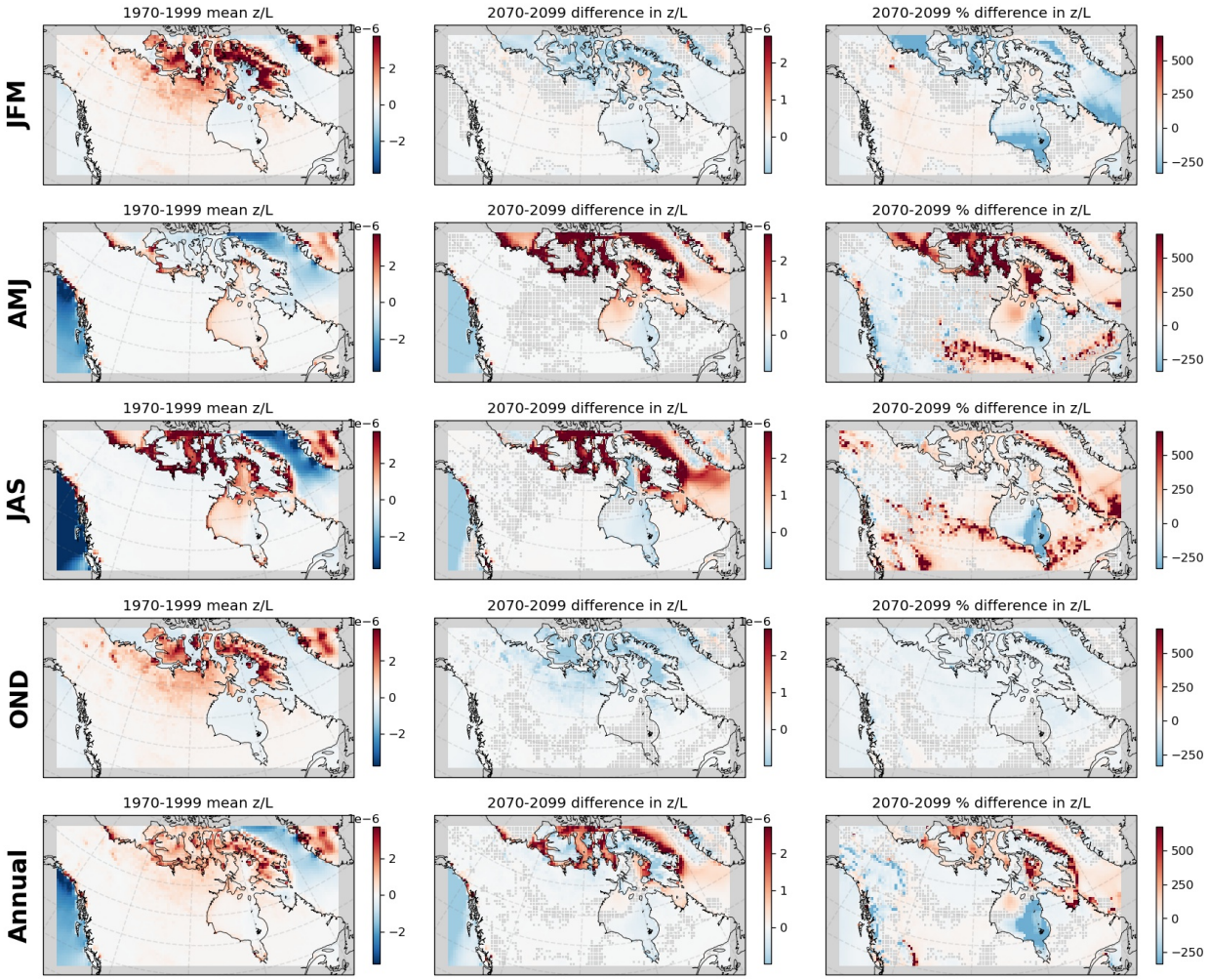

Figure C.4: Mean surface layer stability (z/L) in the reference period (1970-1999, column 1) and difference by 2070-2099 as absolute (column 2) and percent (column 3) by season (rows 1-4) and annually (column 5). Non-robust changes are masked with stippling.

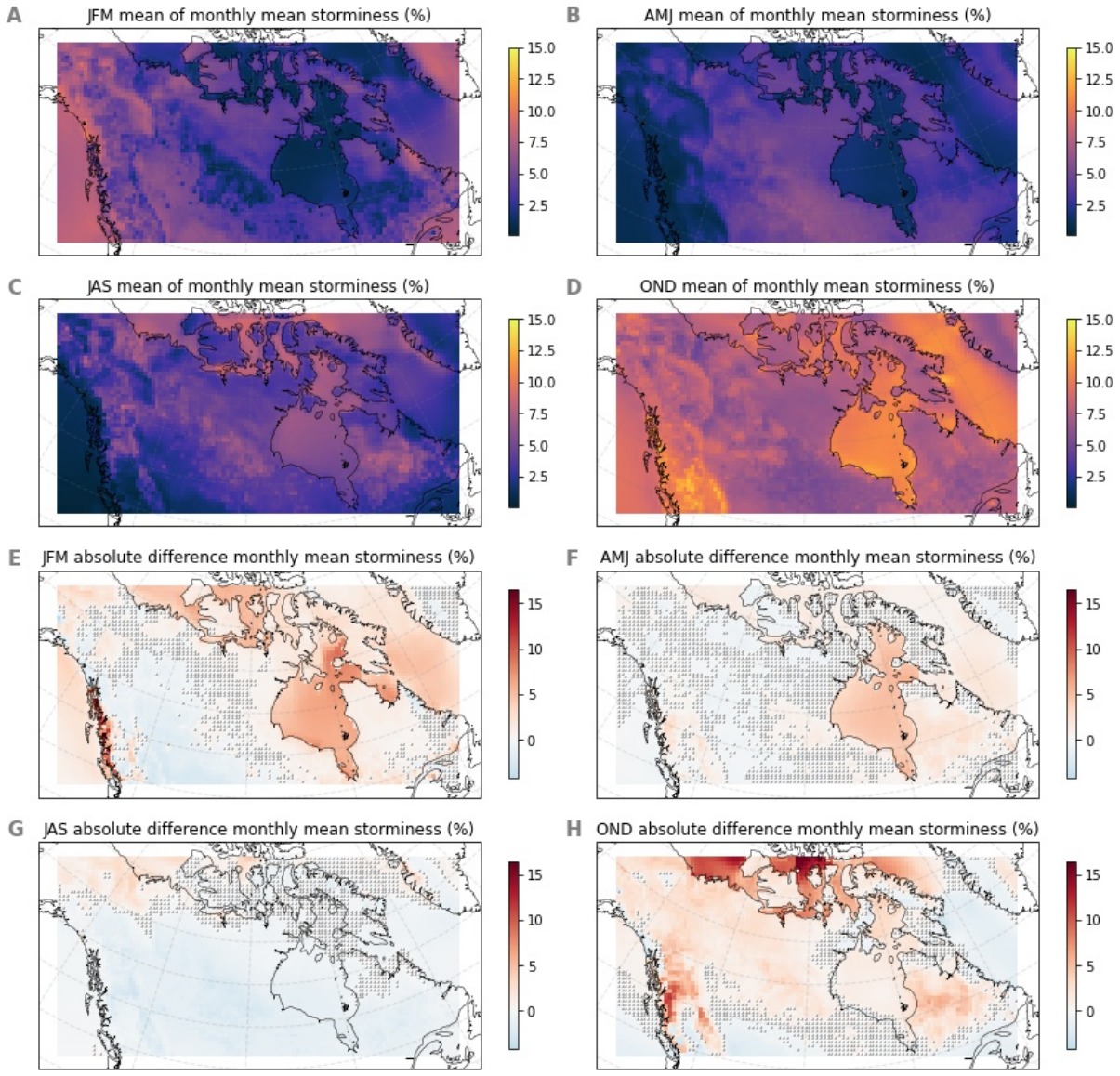

Figure C.5: Mean storminess (percent of time classified as storm activity, A to D) in the reference period (1970-1999) and absolute difference in 2070-2099 from the reference period (E to H). Non-robust changes are masked with stippling.

C.2 Solar power potential: Supplementary material

Table C.2: Inter-annual and inter-daily variability (as measured through coefficient of variation SPP_{day}, see Section 3.8) in the reference period (1970-1999) by the end of the 21st century (2070-2099), showing the ensemble mean with the ensemble minimum and maximum in brackets.

	IAV 1970-1999	IAV 2070-2099	IDV 1970-1999	IDV 2070-2099
	mean (min, max)	mean (min, max)	mean (min, max)	mean (min, max)
Arviat	0.03 (0.02, 0.05)	0.04 (0.03, 0.05)	0.83 (0.82, 0.84)	0.86 (0.85, 0.87)
Baker Lake	0.03 (0.02, 0.05)	0.04 (0.03, 0.05)	0.85 (0.84, 0.86)	0.88 (0.88, 0.89)
Iqaluit	0.04 (0.03, 0.05)	0.05 (0.04, 0.07)	0.86 (0.85, 0.87)	0.90 (0.90, 0.91)
Iqaluit CL	0.04 (0.03, 0.05)	0.05 (0.04, 0.07)	0.85 (0.84, 0.86)	0.88 (0.87, 0.89)
Rankin Inlet	0.03 (0.02, 0.04)	0.04 (0.03, 0.05)	0.78 (0.78, 0.79)	0.80 (0.80, 0.81)
Sachs Harbour	0.05 (0.04, 0.07)	0.07 (0.05, 0.10)	1.06 (1.05, 1.07)	1.13 (1.12, 1.15)
Sanikiluaq	0.04 (0.03, 0.05)	0.04 (0.03, 0.05)	0.75 (0.74, 0.76)	0.82 (0.81, 0.83)
Umiujaq	0.04 (0.03, 0.05)	0.06 (0.04, 0.07)	0.81 (0.80, 0.82)	0.86 (0.84, 0.87)

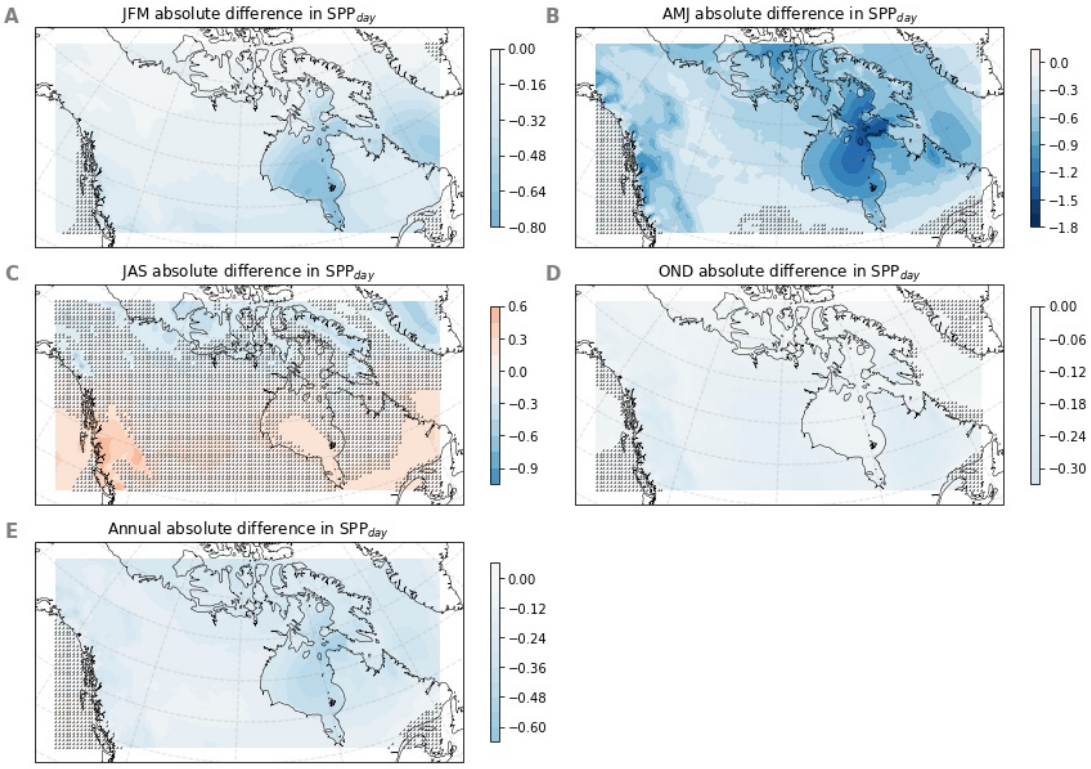

Figure C.6: Ensemble mean change in SPP_{day} (MWh) in 2070-2099 from the reference period (1970-1999), by season. Individual plot colourbars display the range of values for that plot, scaled so that colours are comparable between plots. Non-substantial changes are masked with stippling.

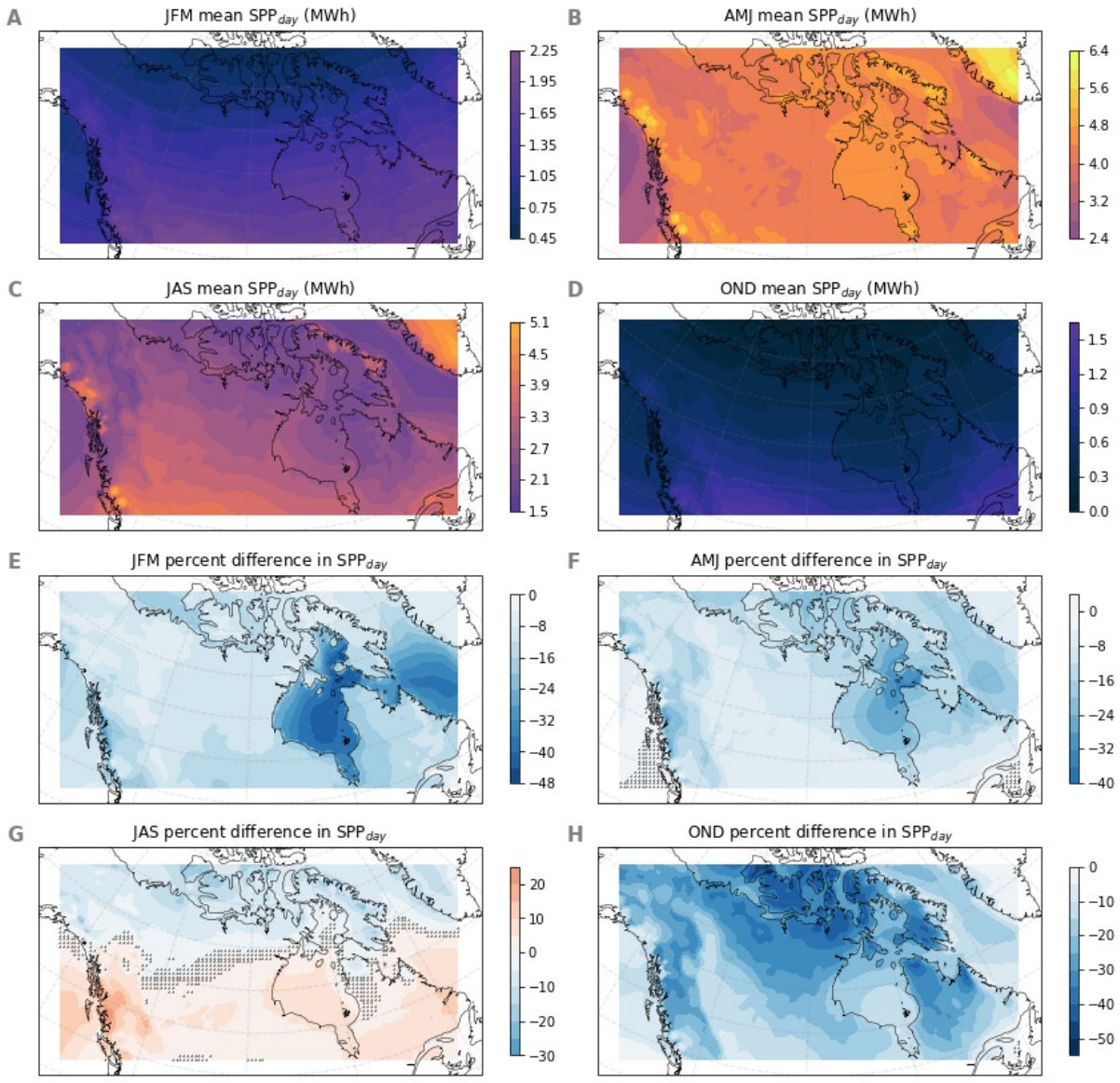

Figure C.7: Mean SPP_{day} in the reference period (1970-1999; MWh, A to D) and ensemble mean percent change (E to H) by 2070-2099, by season. Individual plot colourbars display the range of values for that plot, scaled so that colours are comparable between plots for reference period power production (A to D) and mean change (E to H). Non-robust changes are masked with stippling.

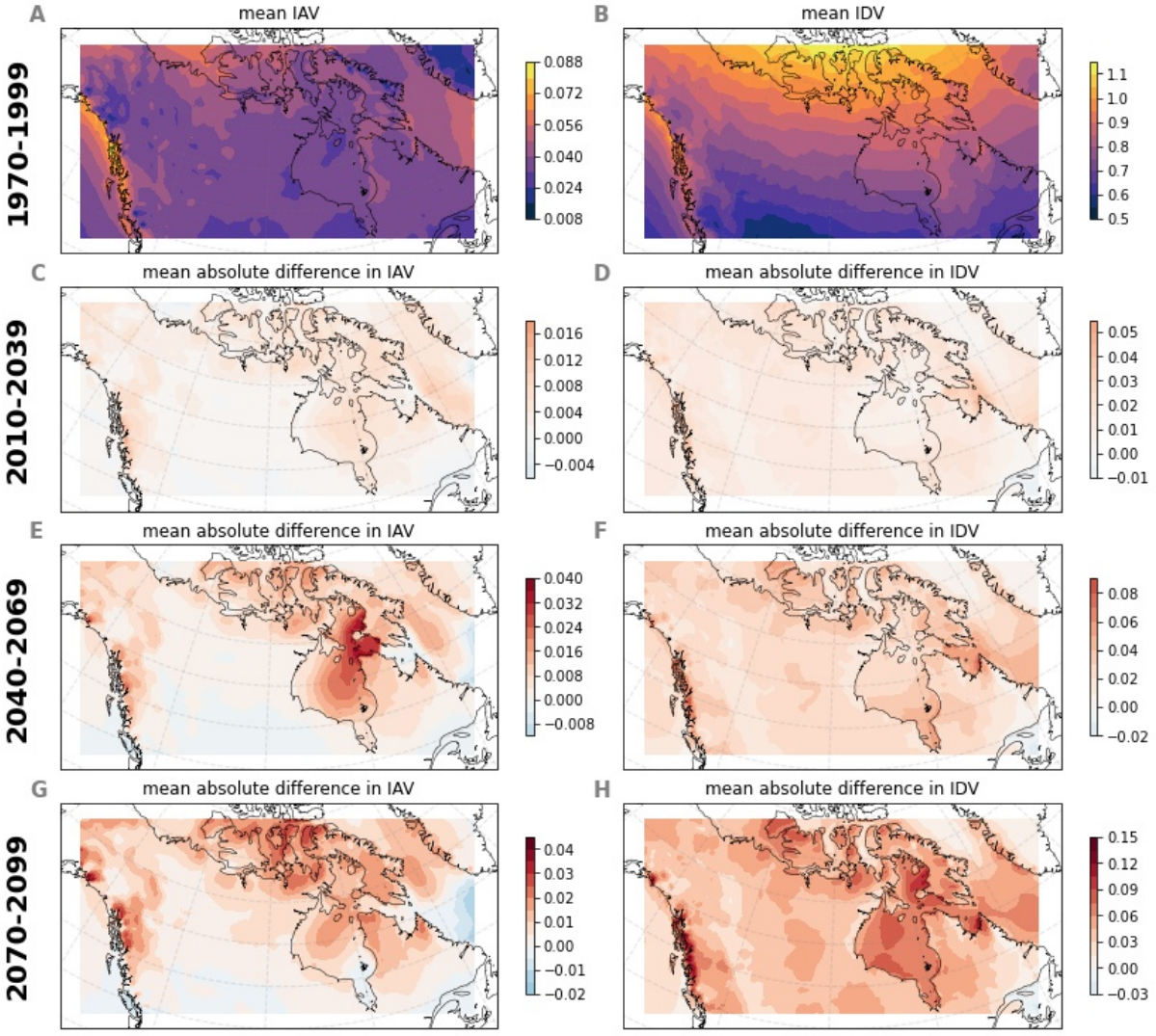

Figure C.8: Daily solar power potential inter-annual variability (column 1) and inter-daily variability (column 2) for the reference period (1970-1999, row 1, dimensionless) and ensemble mean change for the periods 2010-2039, 2040-2069, and 2070-2099 (rows 2 to 4, dimensionless). Individual plot colourbars display the range of values for that plot, scaled so that colours are comparable between plots of IAV change (C, E and G) and IDV change (D, F and H).

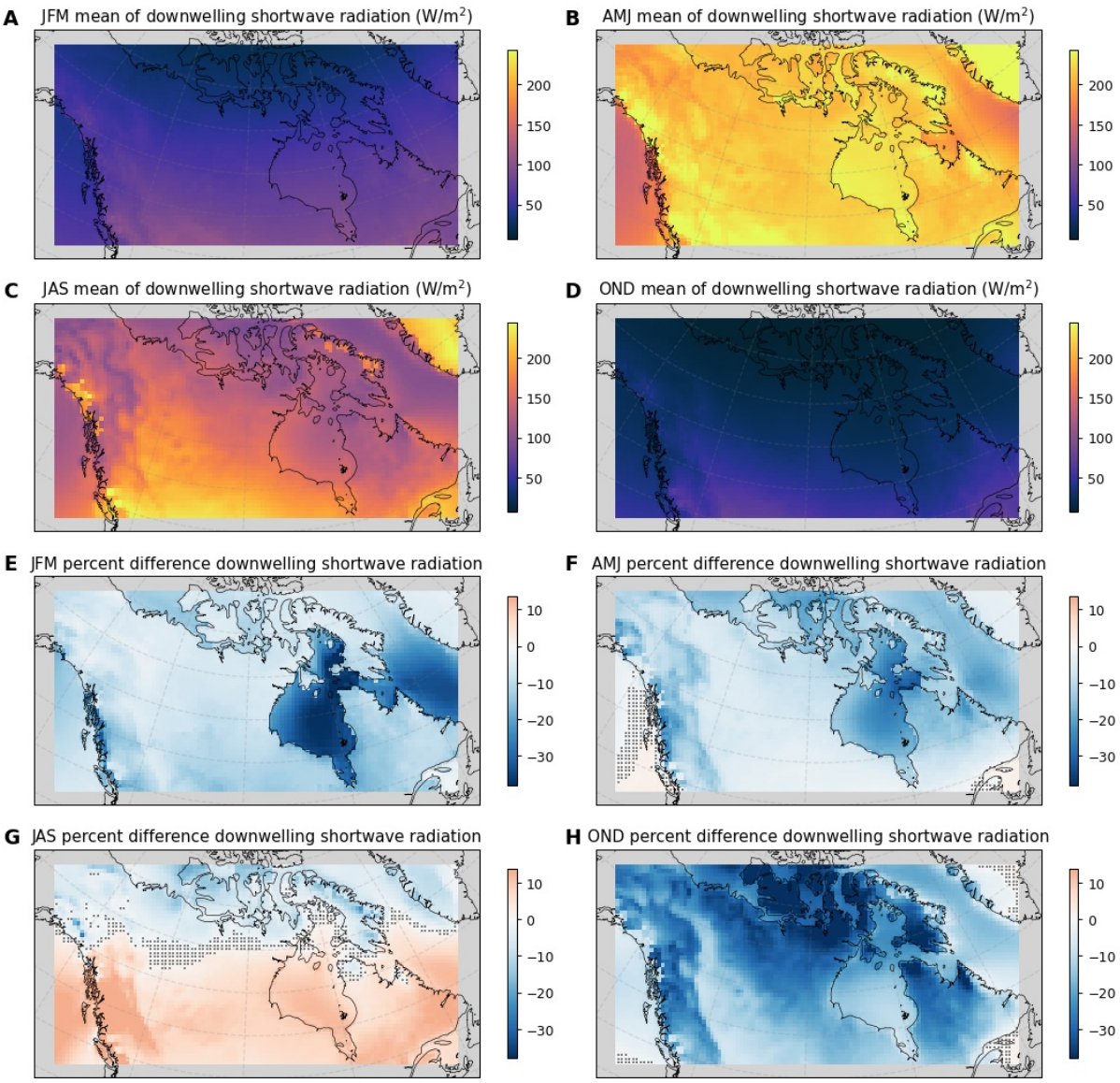

Figure C.9: Ensemble mean DSR by season in the reference period (1970-1999, A-D) and percent difference in 2070-2099 from the reference period (E-H). Non-robust changes are masked with stippling.

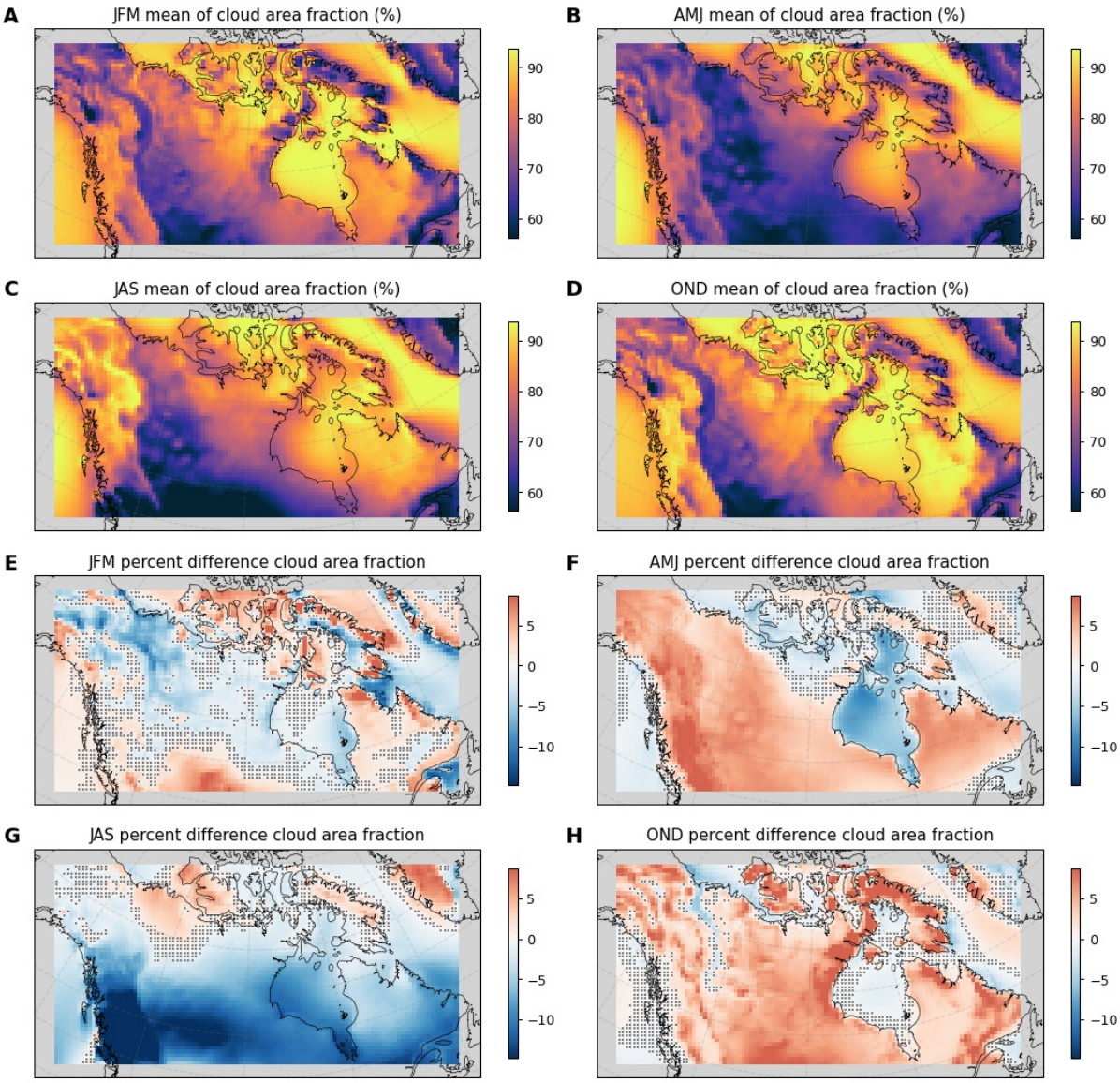

Figure C.10: Ensemble mean cloud area fraction (%, CLT) by season in the reference period (1970-1999, A-D) and percent difference (of % coverage) in 2070-2099 from the reference period (E-H). Non-robust changes are masked with stippling.

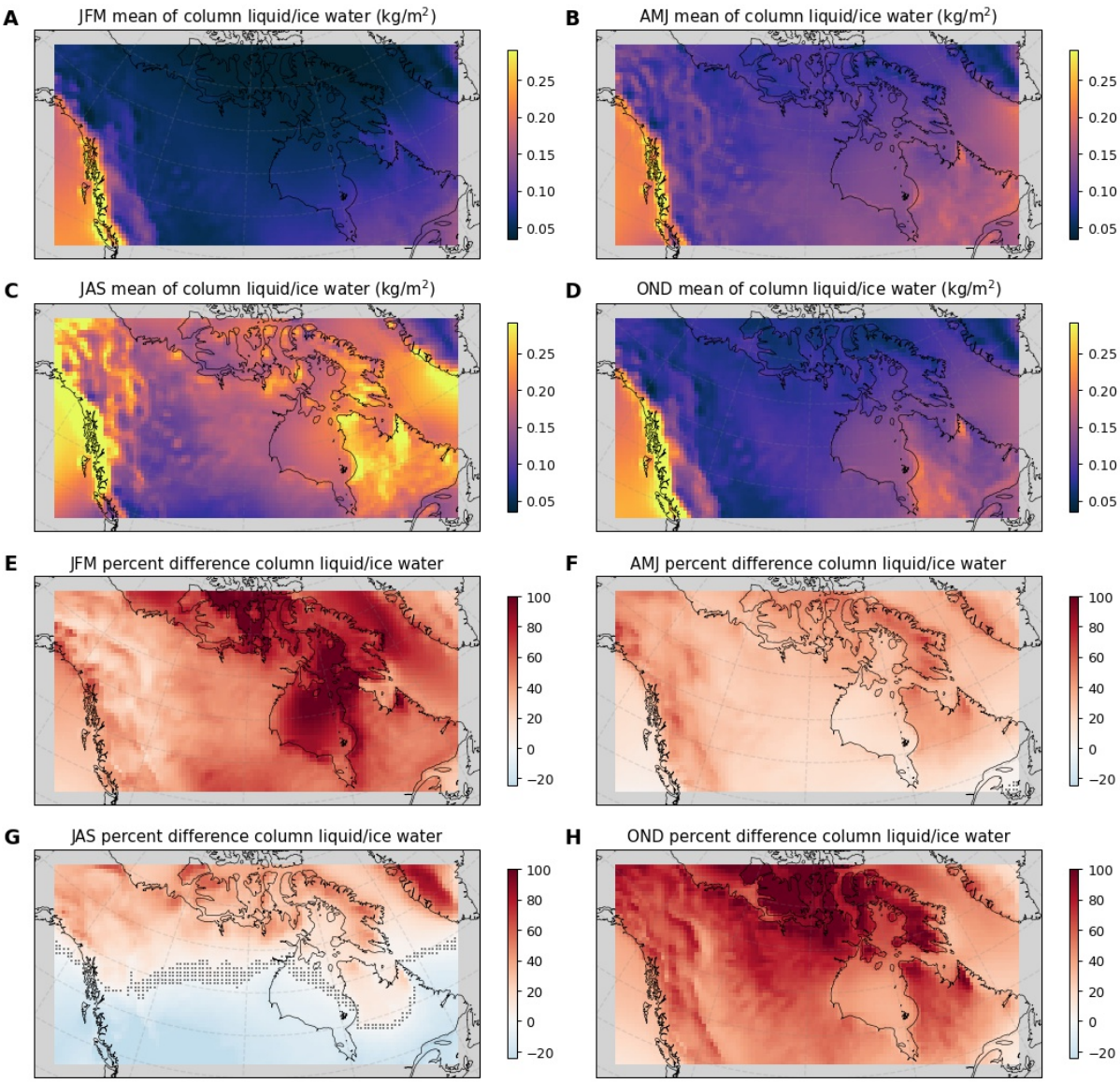

Figure C.11: Ensemble mean column liquid and ice water content (CLW) by season in the reference period (1970-1999, A-D) and percent difference in 2070-2099 from the reference period (E-H). Non-robust changes are masked with stippling.

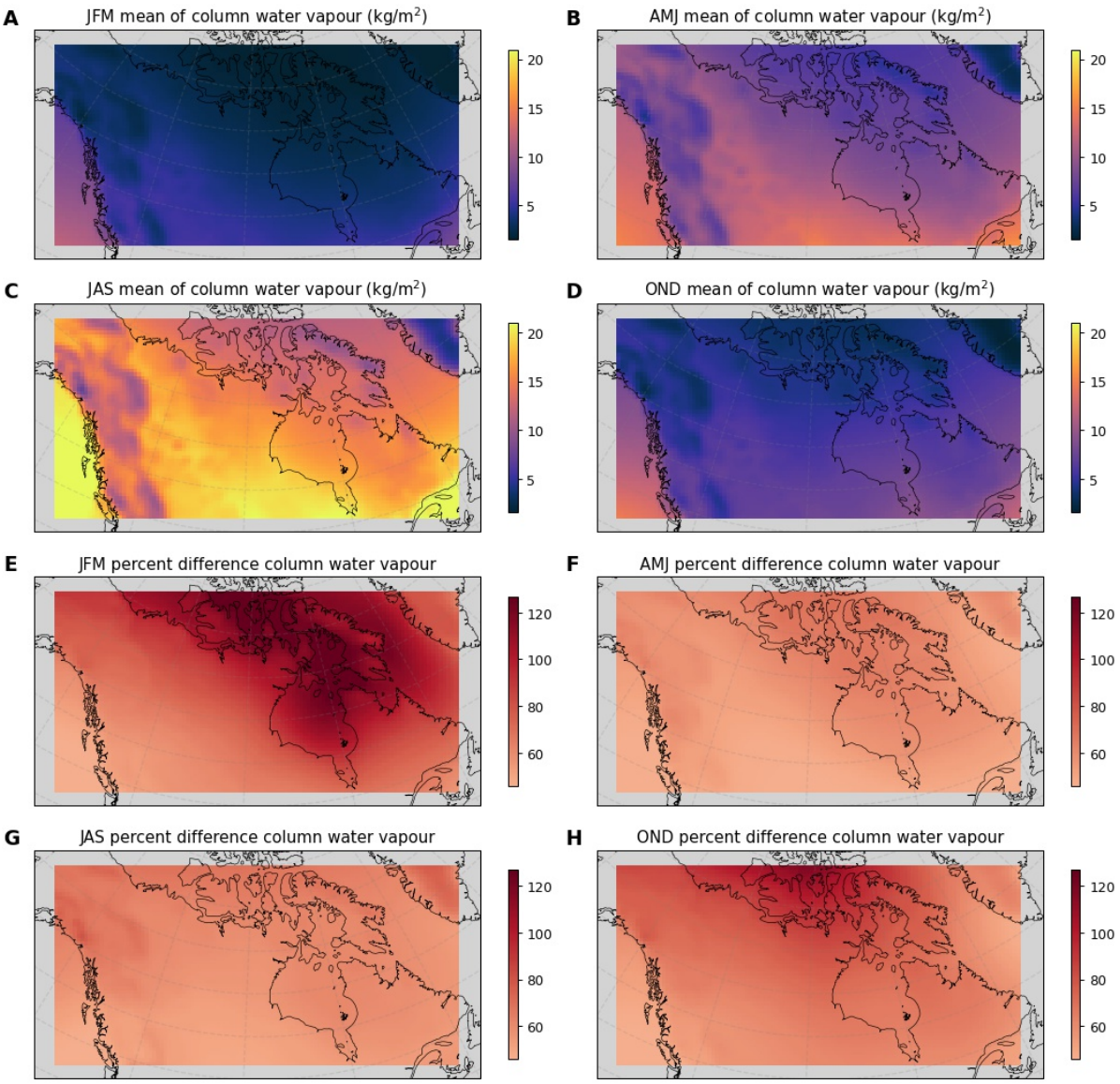

Figure C.12: Ensemble mean column water vapour (CWV) by season in the reference period (1970-1999, A-D) and percent difference in 2070-2099 from the reference period (E-H). Non-robust changes are masked with stippling.

C.3 Covariability: Supplementary material

Table C.3: Correlations between monthly mean WPP_{day} and monthly mean SPP_{day} in the reference period (1970-1999) for detrended values with seasonal cycle removed. 'Annual (seas)' indicates detrended values maintaining seasonal cycle. *Non-significant correlations* (p>0.05) have been italicized.

	AMJ	JAS	JFM	OND	Annual	Annual (seas)
Iqaluit	-0.08	-0.31	-0.33	-0.18	-0.17	-0.10
Sachs Harbour	-0.18	-0.28	-0.22	*-0.01*	-0.16	-0.42
Arviat	-0.10	*-0.00*	-0.15	0.10	-0.05	-0.22
Baker Lake	-0.15	-0.18	-0.18	*0.00*	-0.12	-0.17
Rankin Inlet	-0.11	0.06	-0.05	0.21	*-0.01*	-0.43
Umiujaq	-0.37	-0.38	-0.40	-0.34	-0.32	-0.45
Sanikiluaq	-0.23	-0.09	-0.32	*0.03*	-0.15	-0.51
Iqaluit Coastal Location	-0.09	-0.15	-0.28	-0.11	-0.12	-0.18

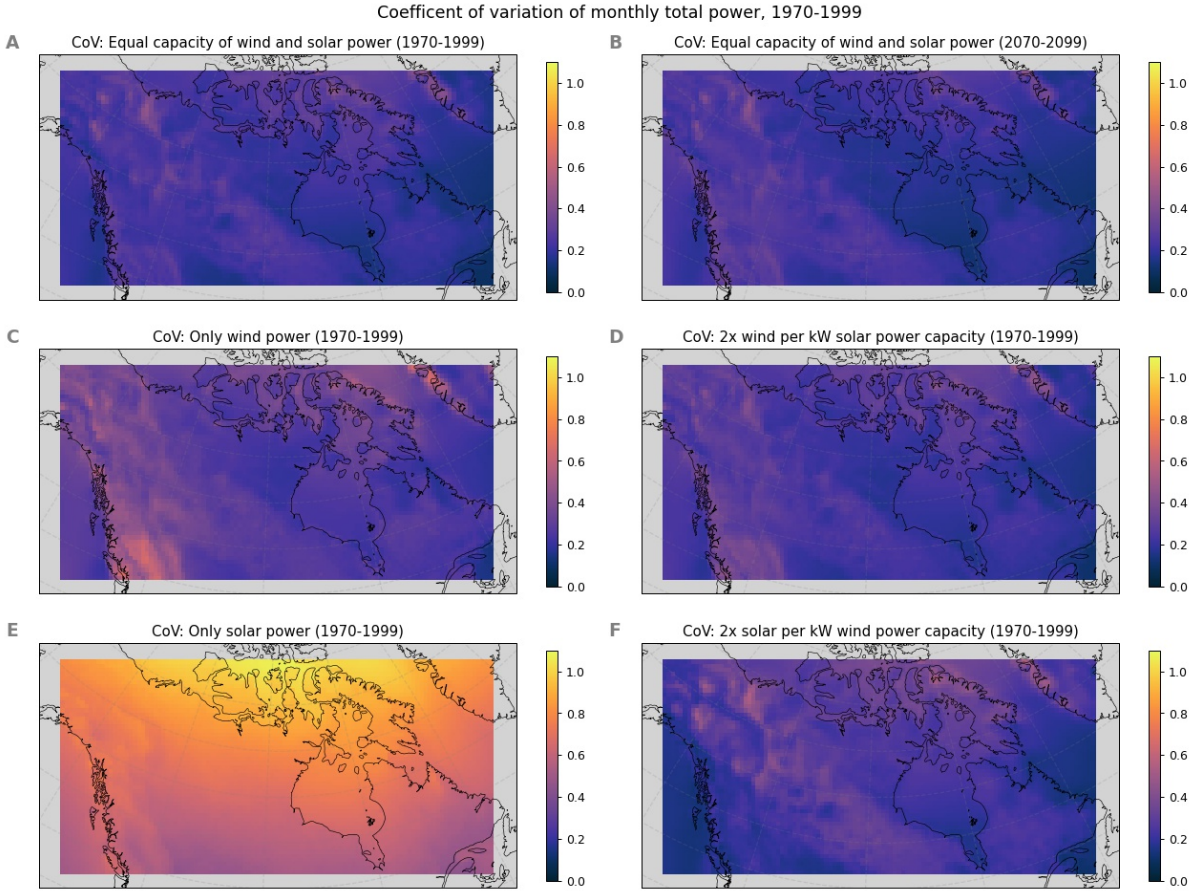

Figure C.13: Coefficient of variation (CoV, dimensionless) of monthly mean $WPP$and monthly mean SPP, for various combinations of wind and solar power capacity: A) equal capacity of wind and solar installed (1970-1999); B) equal capacity of wind and solar installed (2070-2099); C) only wind power installed (1970-1999); D) when wind installed capacity is twice that of solar (1970-1999); E) only solar power installed (1970-1999); F) when solar installed capacity is twice that of wind (1970-1999).

Appendix D: Community-specific results

D.1 Wind power potential

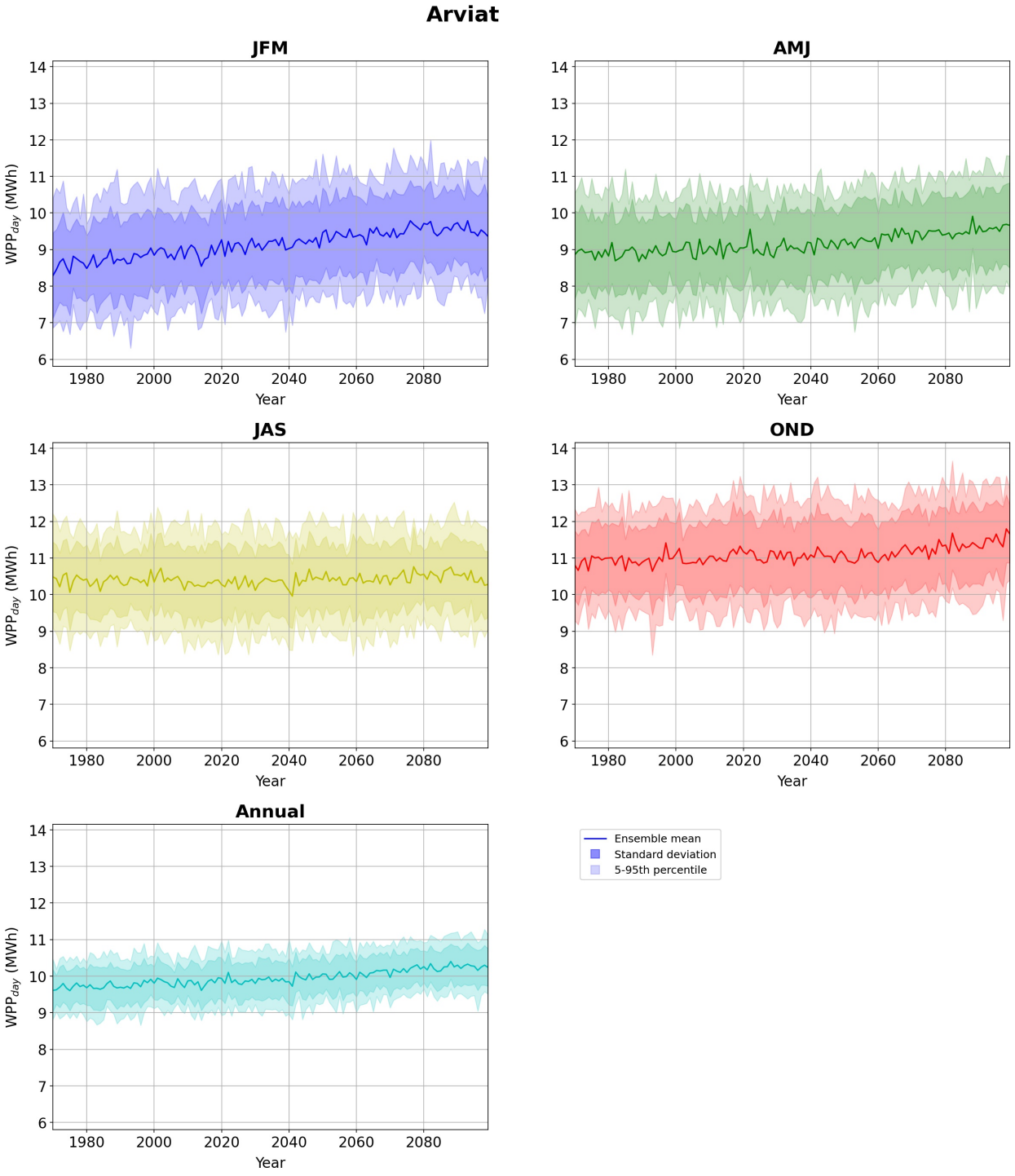

Figure D.1: Mean WPP_{day} projections for Arviat by season and annually from 1970 to 2100, showing the ensemble mean (dark line), standard deviation (dark shading), and 5th to 95th percentiles (light shading).

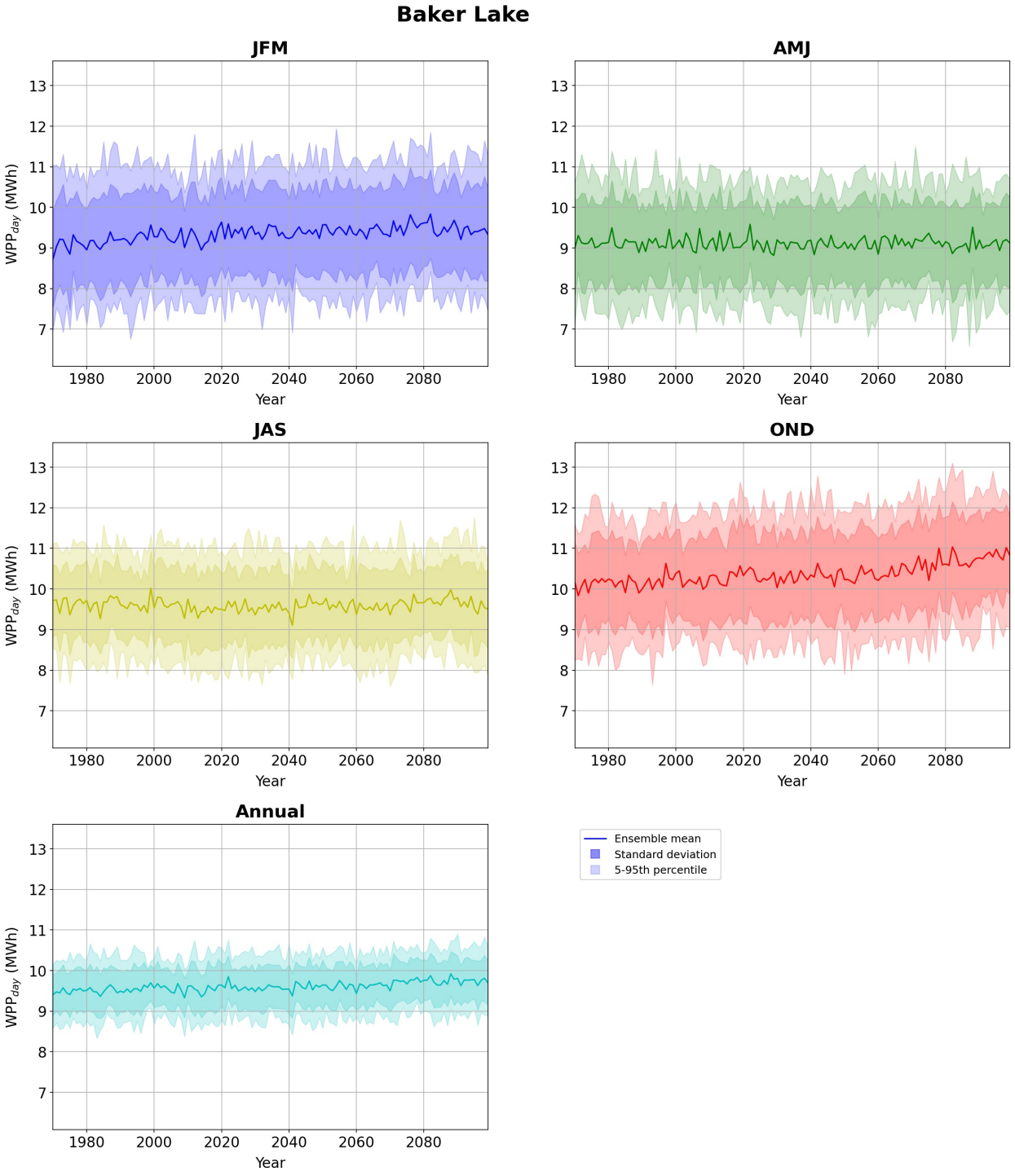

Figure D.2: Mean WPP_{day} projections for Baker Lake by season and annually from 1970 to 2100, showing the ensemble mean (dark line), standard deviation (dark shading), and 5th to 95th percentiles (light shading).

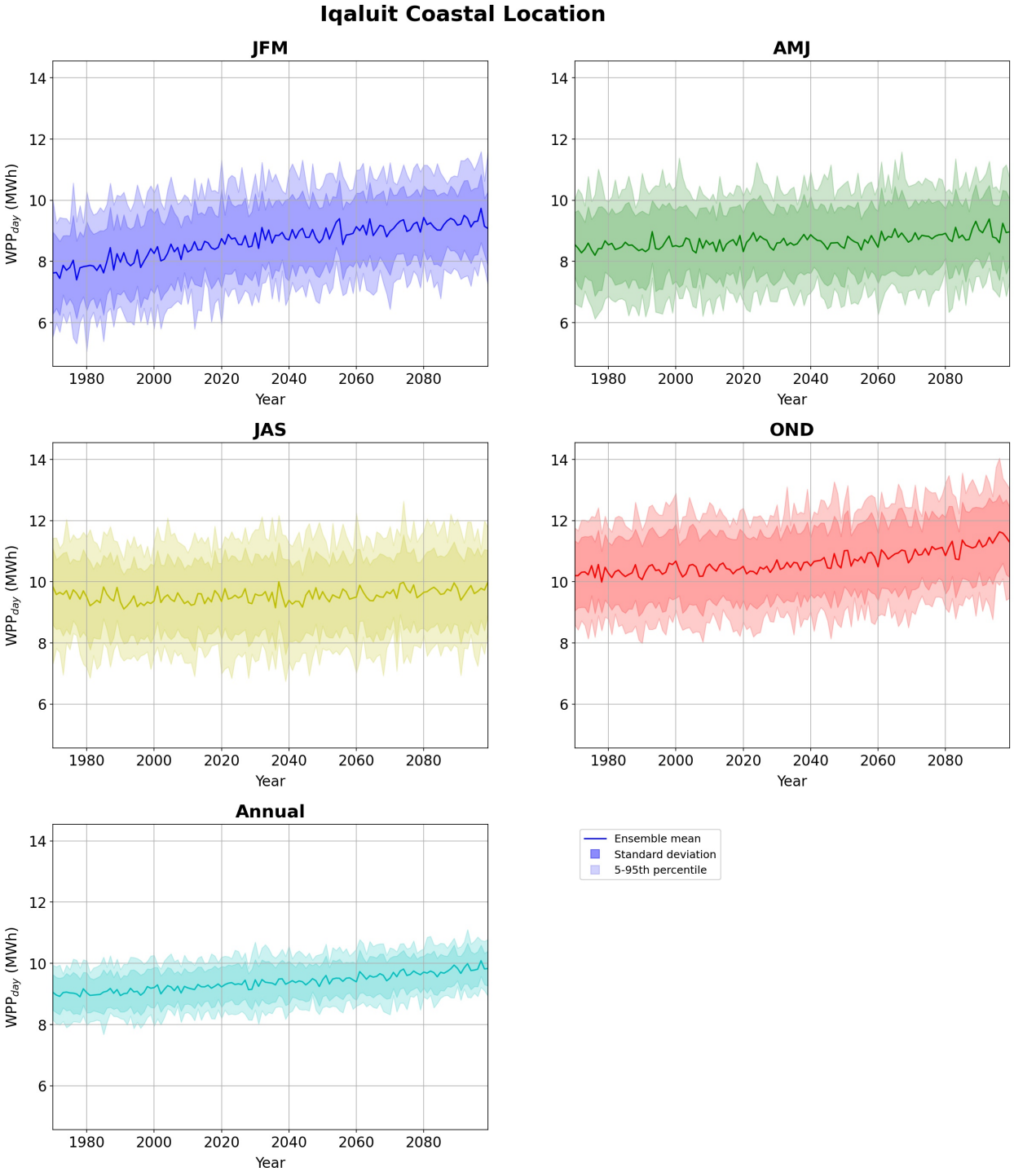

Figure D.3: Mean WPP_{day} projections for Iqaluit (Coastal Location) by season and annually from 1970 to 2100, showing the ensemble mean (dark line), standard deviation (dark shading), and 5th to 95th percentiles (light shading).

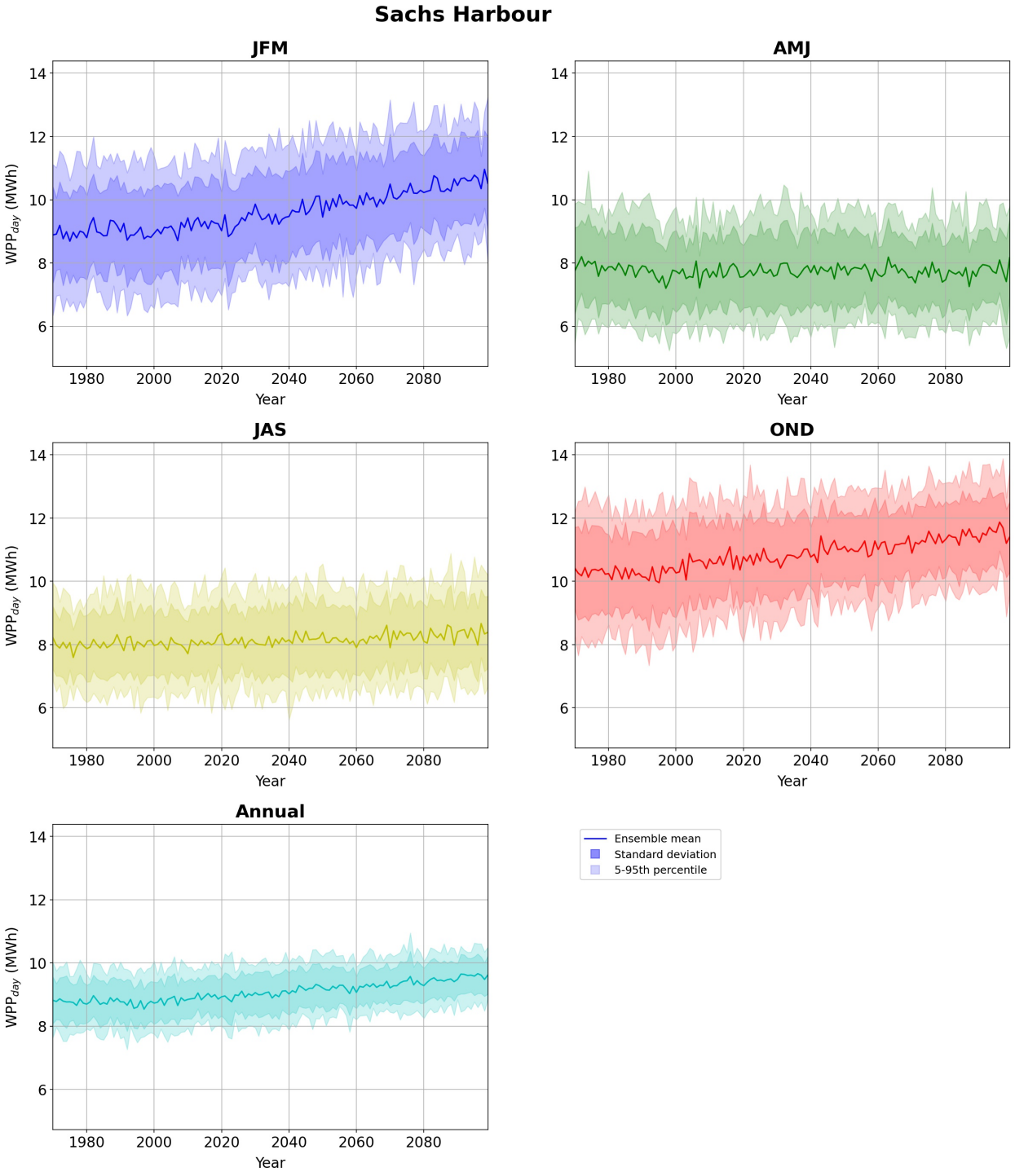

Figure D.4: Mean WPP_{day} projections for Sachs Harbour by season and annually from 1970 to 2100, showing the ensemble mean (dark line), standard deviation (dark shading), and 5th to 95th percentiles (light shading).

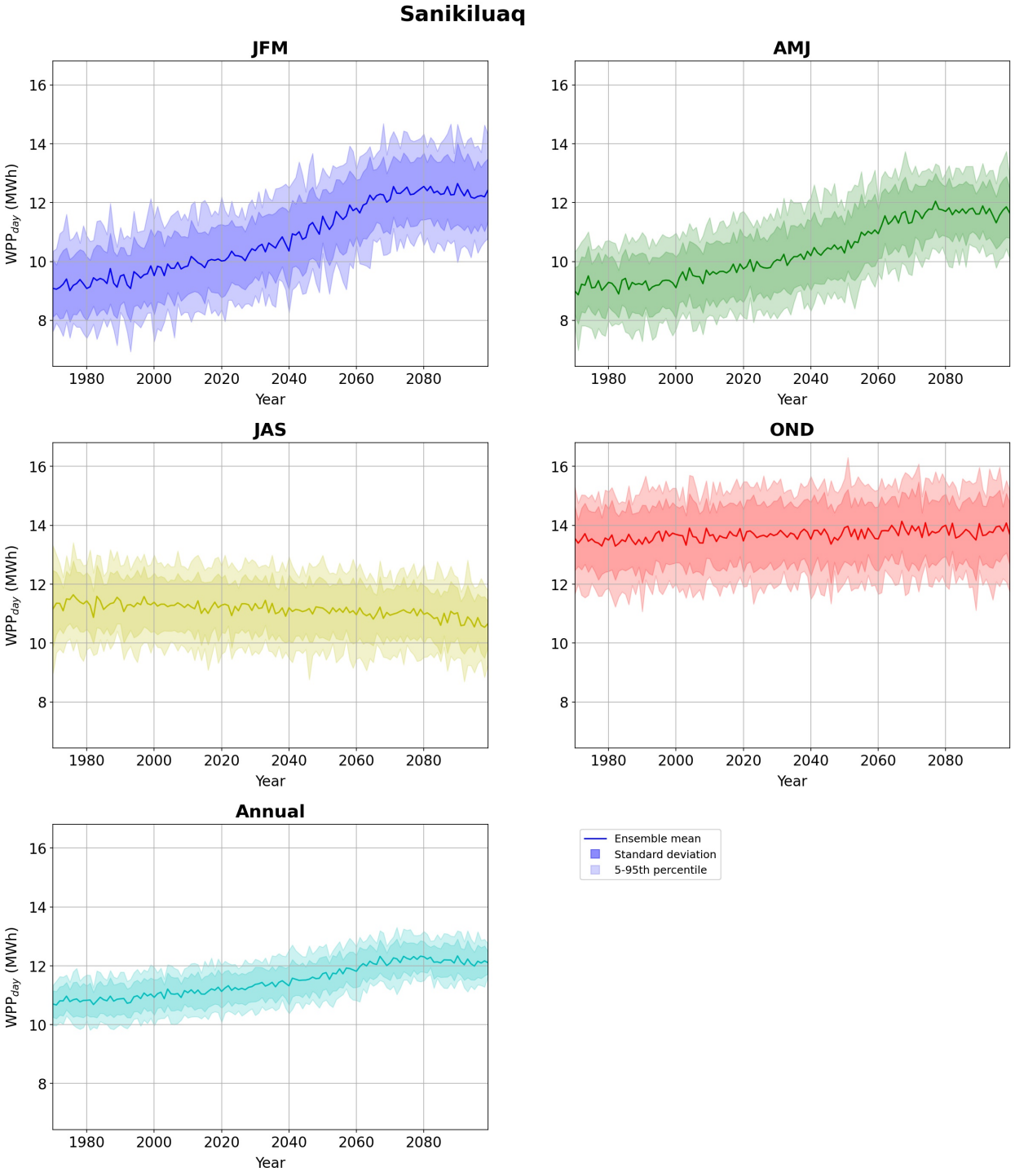

Figure D.5: Mean WPP_{day} projections for Sanikiluaq by season and annually from 1970 to 2100, showing the ensemble mean (dark line), standard deviation (dark shading), and 5th to 95th percentiles (light shading).

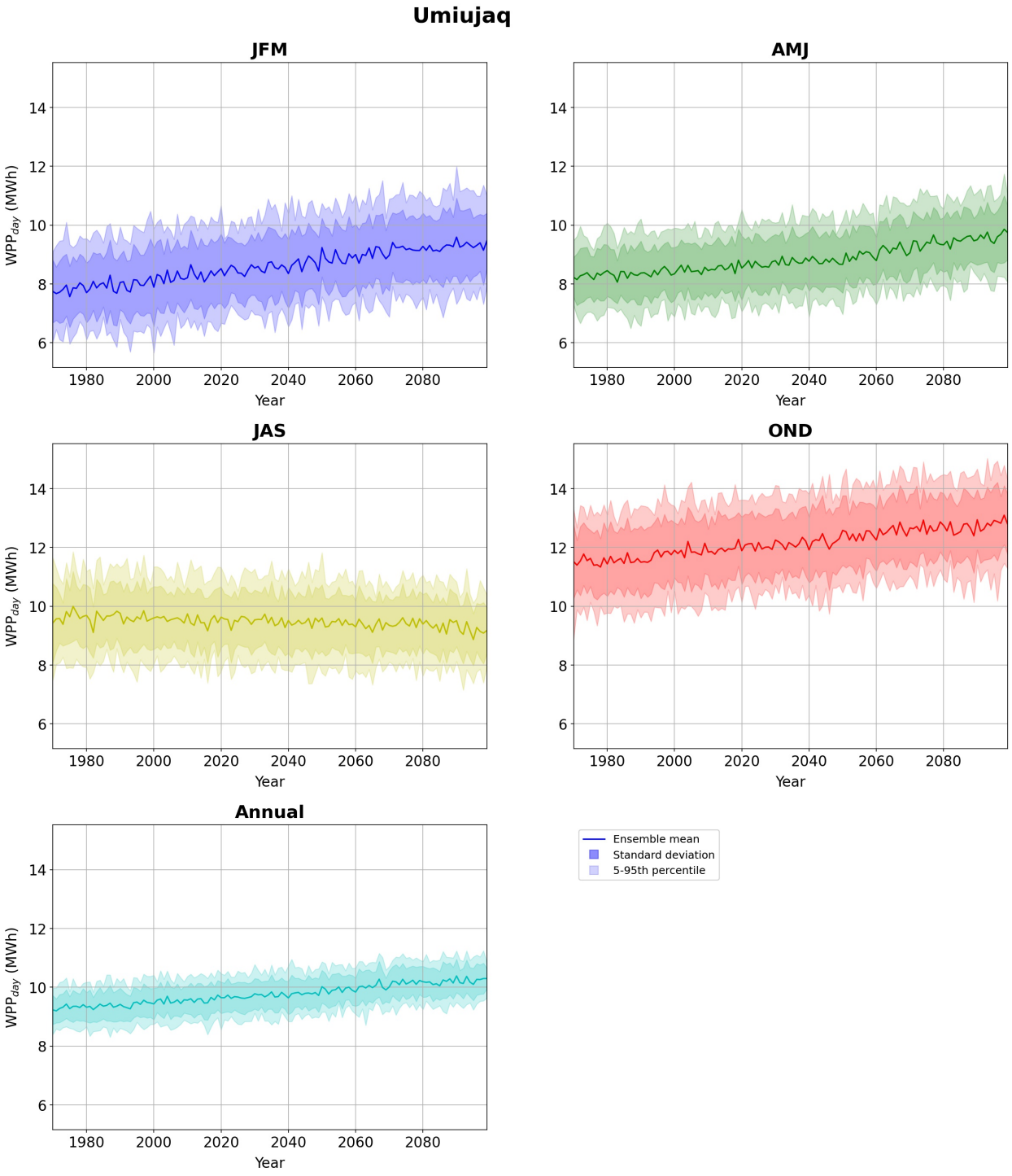

Figure D.6: Mean WPP_{day} projections for Umiujaq by season and annually from 1970 to 2100, showing the ensemble mean (dark line), standard deviation (dark shading), and 5th to 95th percentiles (light shading).

D.2 Solar power potential

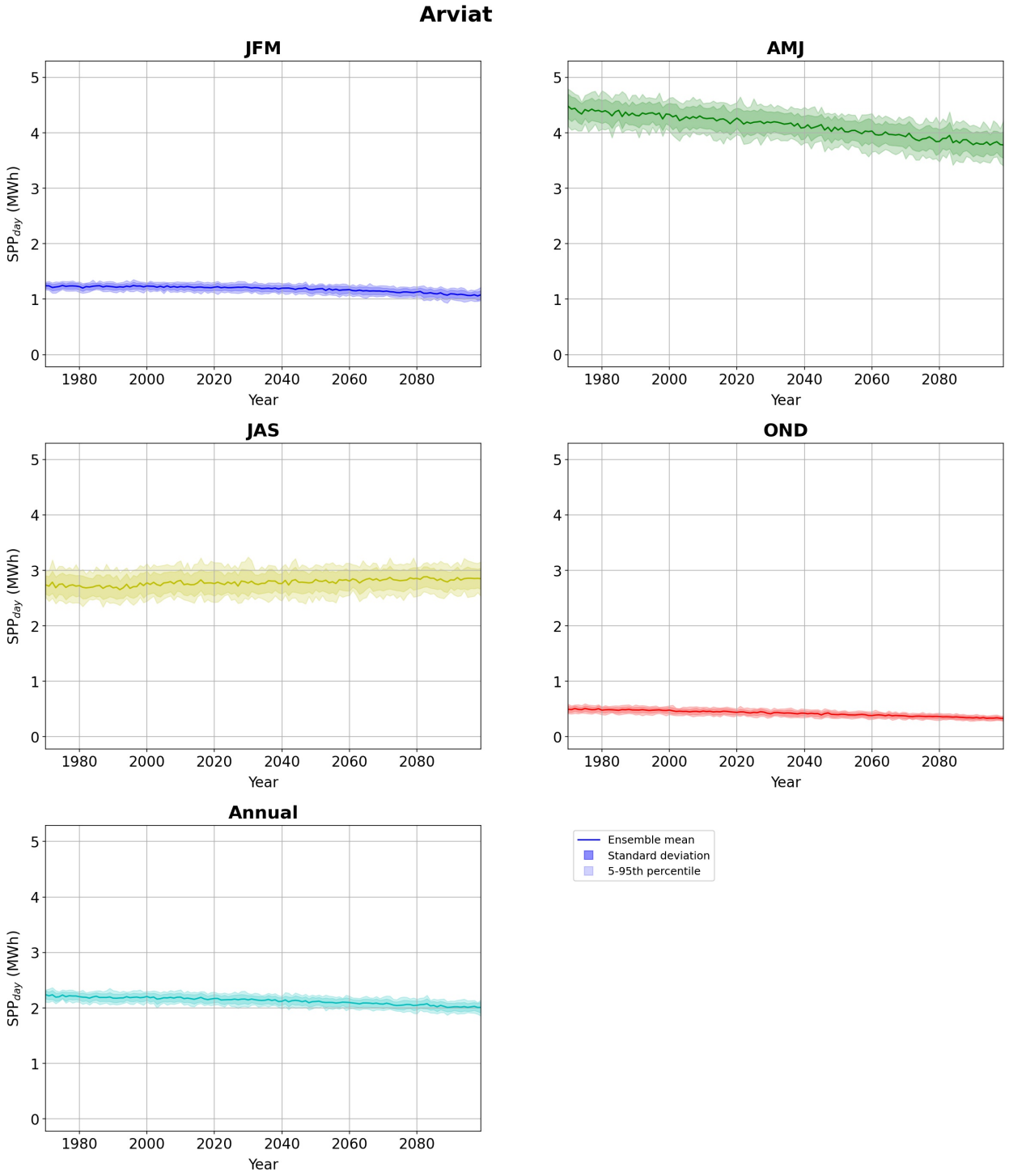

Figure D.7: Mean SPP_{day} projections for Arviat by season and annually from 1970 to 2100, showing the ensemble mean (dark line), standard deviation (dark shading), and 5th to 95th percentiles (light shading).

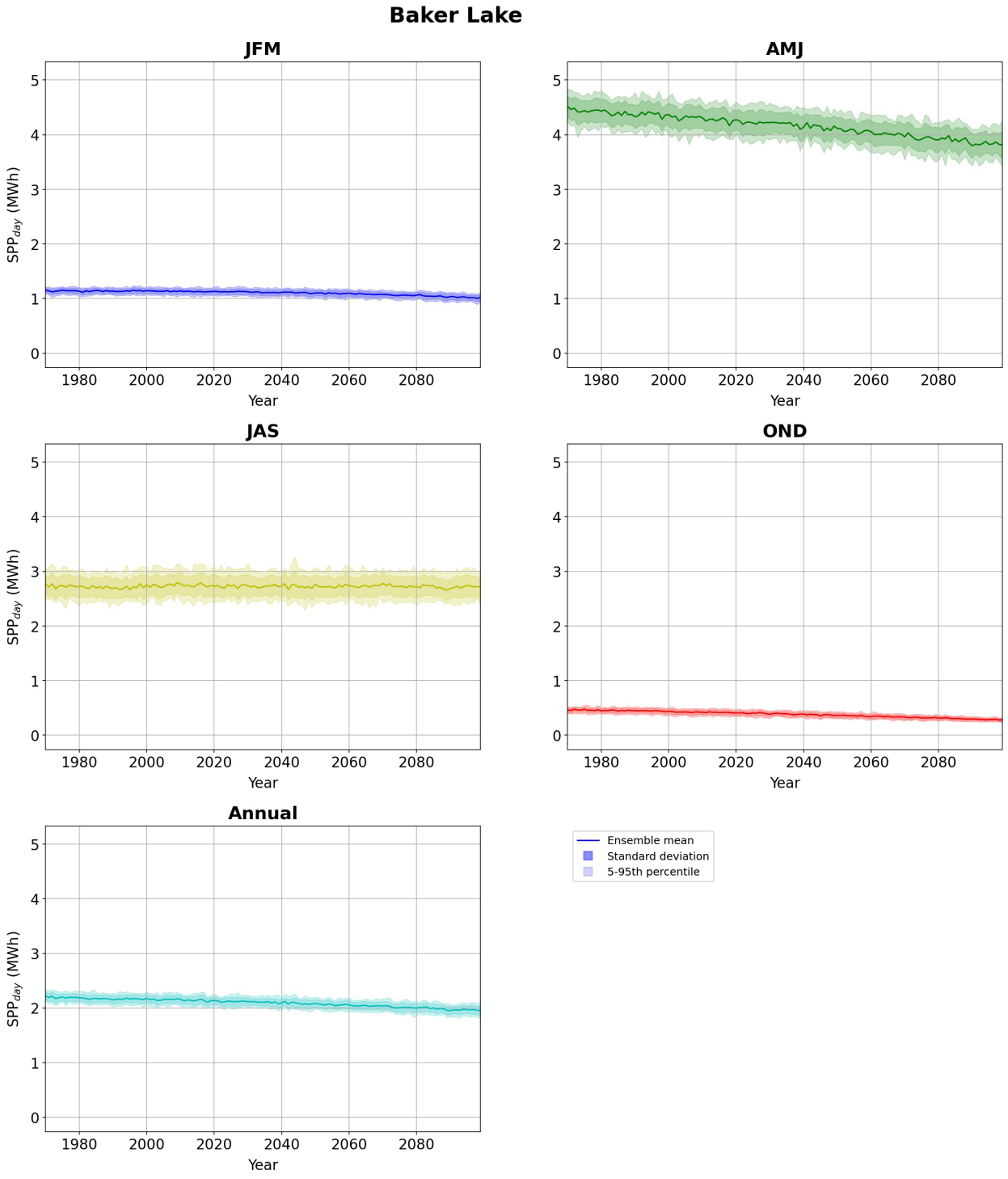

Figure D.8: Mean SPP_{day} projections for Baker Lake by season and annually from 1970 to 2100, showing the ensemble mean (dark line), standard deviation (dark shading), and 5th to 95th percentiles (light shading).

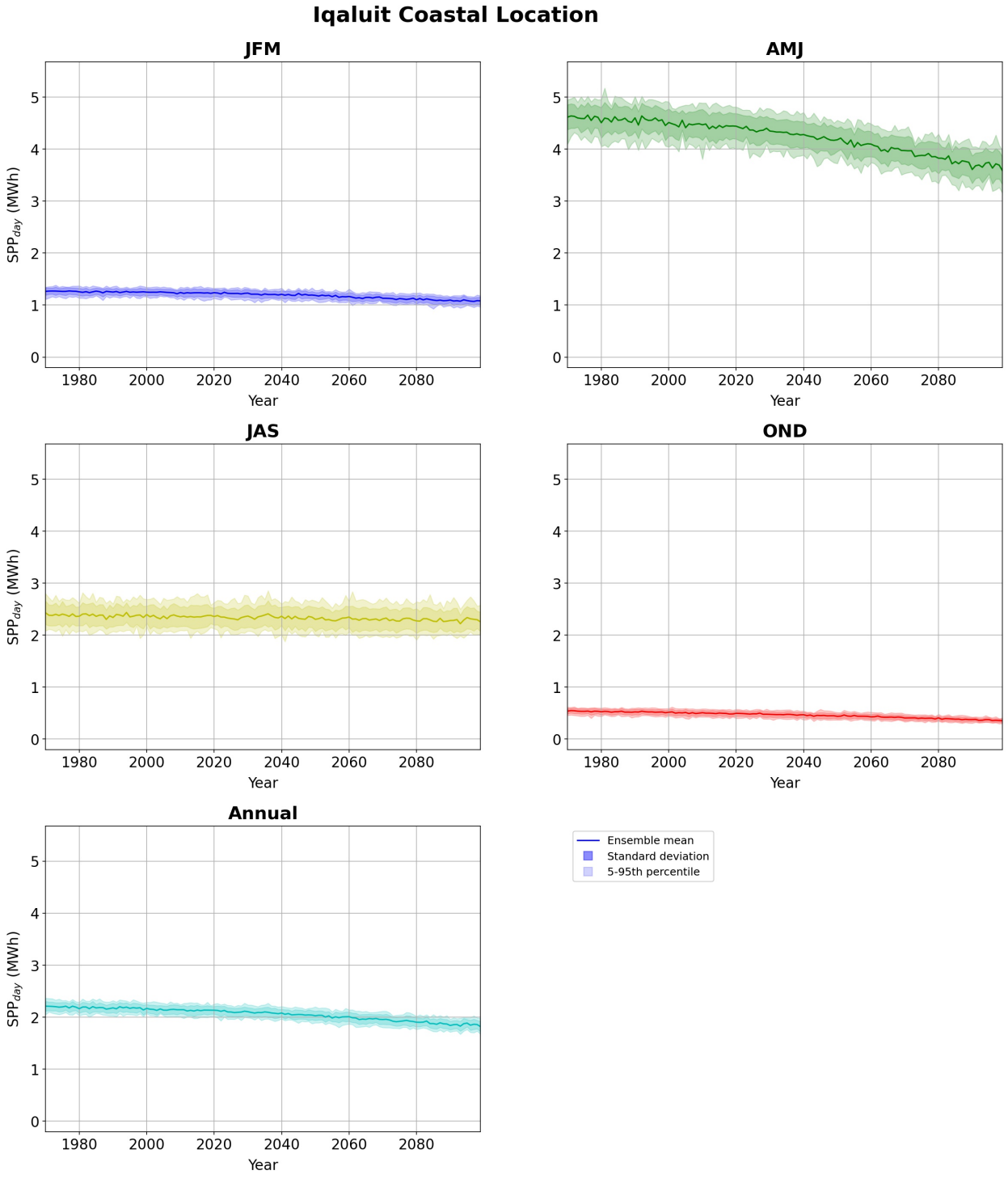

Figure D.9: Mean SPP_{day} projections for Iqaluit (Coastal Location) by season and annually from 1970 to 2100, showing the ensemble mean (dark line), standard deviation (dark shading), and 5th to 95th percentiles (light shading).

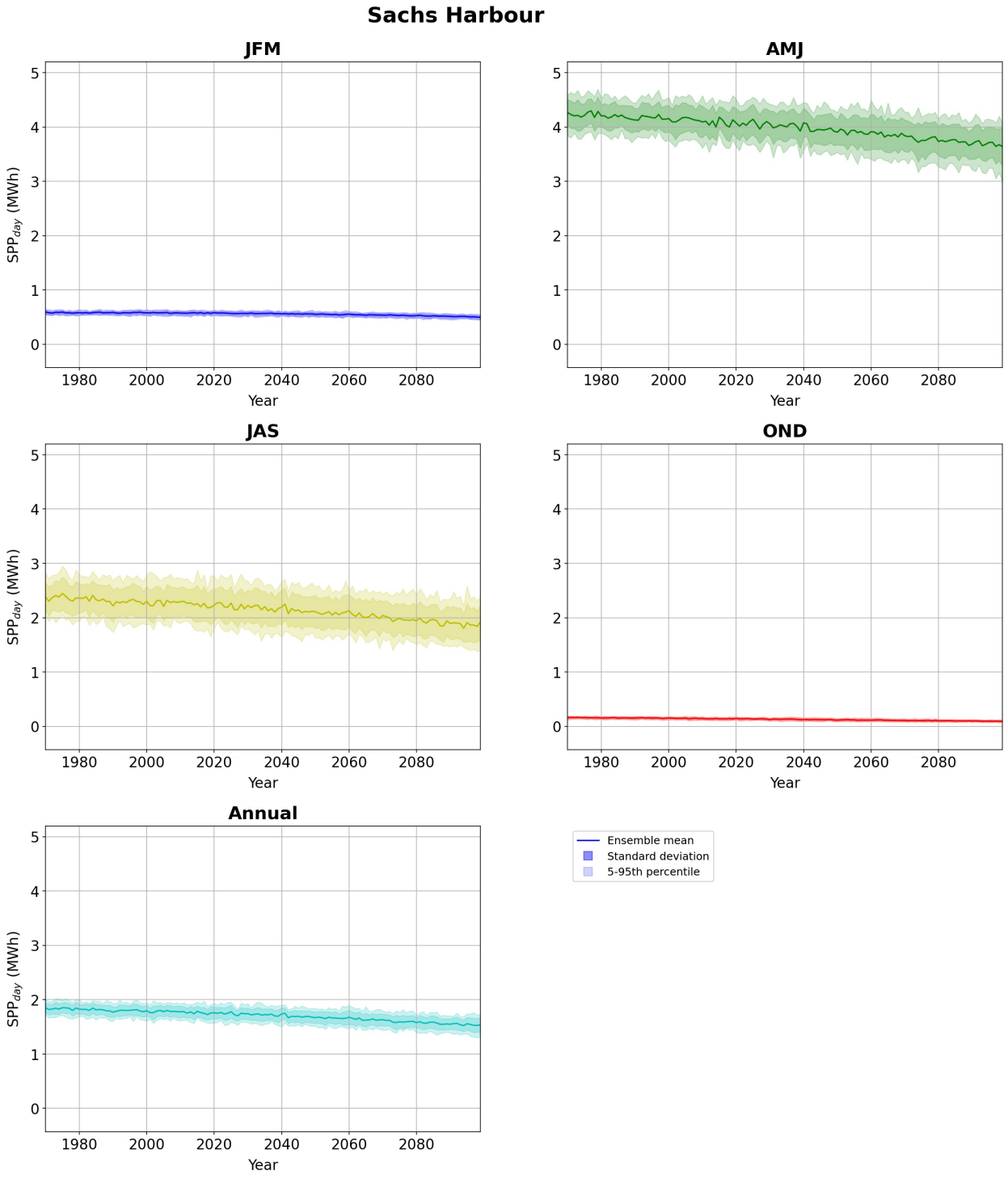

Figure D.10: Mean SPP_{day} projections for Sachs Harbour by season and annually from 1970 to 2100, showing the ensemble mean (dark line), standard deviation (dark shading), and 5th to 95th percentiles (light shading).

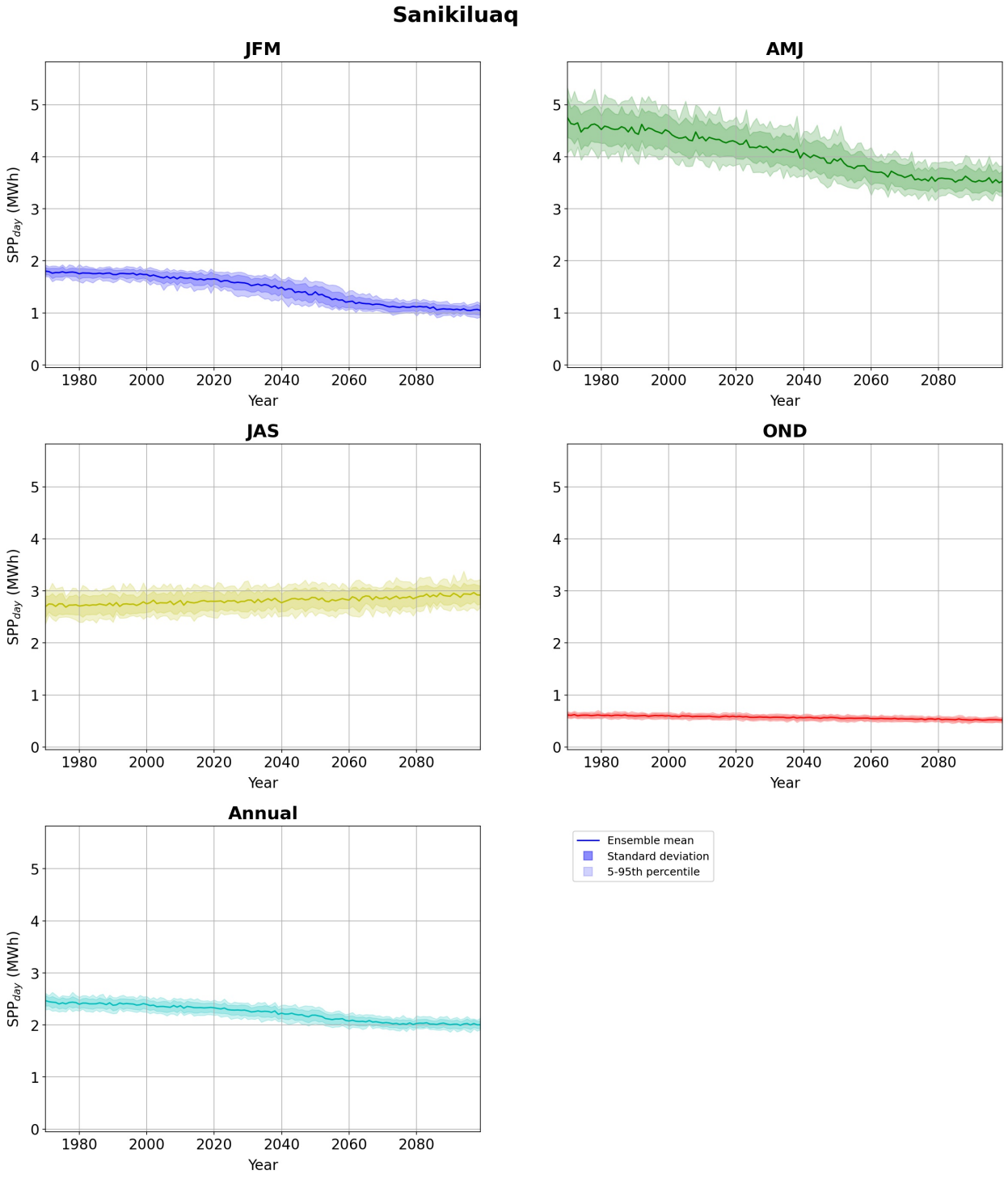

Figure D.11: Mean SPP_{day} projections for Sanikiluaq by season and annually from 1970 to 2100, showing the ensemble mean (dark line), standard deviation (dark shading), and 5th to 95th percentiles (light shading).

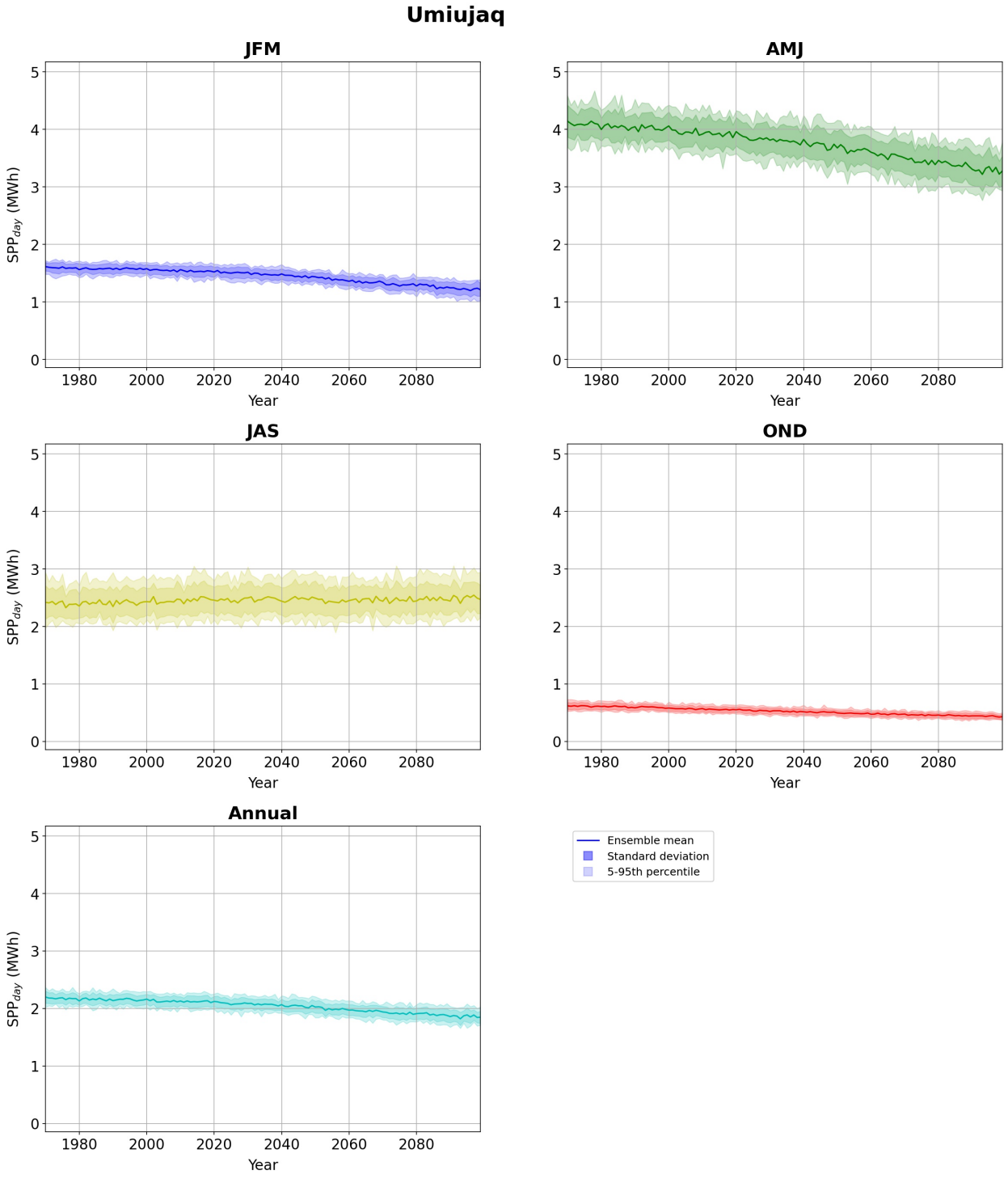

Figure D.12: Mean SPP_{day} projections for Umiujaq by season and annually from 1970 to 2100, showing the ensemble mean (dark line), standard deviation (dark shading), and 5th to 95th percentiles (light shading).